Doctoral Dissertation
博士論文

Research on wavelength-scale metal-clad semiconductor lasers and their waveguide coupling

（波長スケール金属共振器半導体レーザと その導波路結合に関する研究）

Yi Xiao

肖　熠

Under the supervision of Professor Yoshiaki Nakano

（指導教員：中野　義昭）

Department of Electrical Engineering and information Systems,

School of Engineering, The University of Tokyo

Research on wavelength-scale metal-clad semiconductor lasers and their waveguide coupling

（波長スケール金属共振器半導体レーザと
その導波路結合に関する研究）

A dissertation submitted to the Graduated School of Engineering
The University of Tokyo
in partial fulfillment of the requirements for the degree of Doctor of Philosophy

Yi Xiao

肖　熠

Under the supervision of Professor Yoshiaki Nakano

（指導教員：中野　義昭）

Abstract

Large scale integrated electronic circuits have been developed year by year in Moore's Law, and close to fundamental physics limit now. Signals transferred through electrons in wires would get distorted at high communication speed. This is limited by the transmission characteristic of wires. One of the promising solutions is believed to be using light to carry signals instead of electrons. However, conventional photonic devices are three orders larger than electronic devices. This mismatch makes the hybrid integration of photonics and electronics very challenging.

Miniaturization of photonic devices is an important factor for future high speed signal processing. In this thesis, I focused on nano-laser, which is extremely important for optical communication systems. It is a key technology to achieve on-chip optical interconnects. In 2007, first metal-clad laser was demonstrated experimentally. Its size was 260 nm in diameter, on deep sub-wavelength order, considered as high potential candidate in on-chip high-density photonics.

Metal-clad laser has merits of strong light confinement, good thermal dissipation, Purcell effect enhancement and high-speed operation. However, making a metal-clad laser is very challenging because metal is lossy at room temperature, leading to higher threshold than expected. In addition, quality of metal film is poor, further degrading the performance of laser. Since light is easily scattered by rough surface, imperfection of fabrication is a problem to realize such device as well.

Great efforts were made to promote this topic. In our lab, capsule-shaped cavity was discussed numerically so far. By changing the planar mirror of conventional Fabry-Perot cavity into curved mirror, the resonating mode is constricted at center of cavity. As a result, overlap with metal is decreased, metal induced loss is reduced.

I improved the fabrication process, demonstrated capsule-shaped cavity experimentally. In order to confirm the idea of new design, optical pumping was used instead of electrical pumping which may induce heating problem. The cavity has a dimension of 1.6 μm × 1.0 μm. It achieved lasing at room temperature under pulsed optical pumping. Light-in light-out plot shows that capsule-shaped cavity has higher slope

efficiency and higher side mode compression ratio at same pumping power than rectangular cavity.

Basing on this result, I further discussed waveguide-coupled wavelength-scale metal-clad laser. Metal-clad cavity's Q factor is as low as several 100s. Coupling with waveguide will further degrade the Q factor, make it difficult to start lasing. So far waveguide-coupled wavelength-scale LED has been reported but waveguide-coupled wavelength-scale laser is not yet. Capsule-shaped cavity originally has higher Q factor than rectangular cavity, providing advantage in coupling with waveguide. I discussed the design of waveguide-coupled wavelength-scale metal-clad laser using capsule-shaped cavity numerically. By analyzing the power loss in the optical oscillation, it is clear that engineering the width of joint between cavity and waveguide can affect overall Q factor to some extent. This provide a relative easy way to design the device. I tried to fabricate the device with different designs, and spontaneous emission was observed from output waveguide. It is evidence that light is coupled into waveguide successfully.

For future improvement, firstly, better plasmonic material other than silver or gold is required, which has high reflectivity at infrared wavelength and low absorption loss. Secondly, making the device on silicon on insulator (SOI) substrate instead of InP substrate could enhance Q factor of cavity and coupling efficiency with waveguide. Lastly, new active material with higher gain than current semiconductor is preferred in nano-laser to achieve lasing under limited volume.

Contents

Chapter 1   Introduction

1.1   Photonic integrated circuits

Optical communication network has been highly developed since optical fiber was invented in 1960s. Comparing to electrical signals transited by copper wire, optical signals can work in much higher rate with less distortion. Basing on this intrinsic advantage, communication speed goes up to 40 Gbps, which leads to recent information society. Of course, besides low loss long distance transition technology, optical transmitter, optical receiver, optical modulator and optical switch play an important role as well. Most utilized materials in optical field are InP and silicon platform. InP has a direct band gap, which make it fit for light emitter. In addition, its band gap energy is around infrared wavelength, which is low loss wavelength band of silicon fiber. As a result, light source used in optical communication system, LED or laser diode is almost based on InP platform. Silicon is indirect band gap material, has low light emission efficiency. Although latest research shows that silicon can also work as light emitter [1], it is still far from commercial application. However, since CMOS fabrication process has been well developed for large-scale integrated circuit (LSIC), it is easy to make optical devices (except emitters) by silicon.
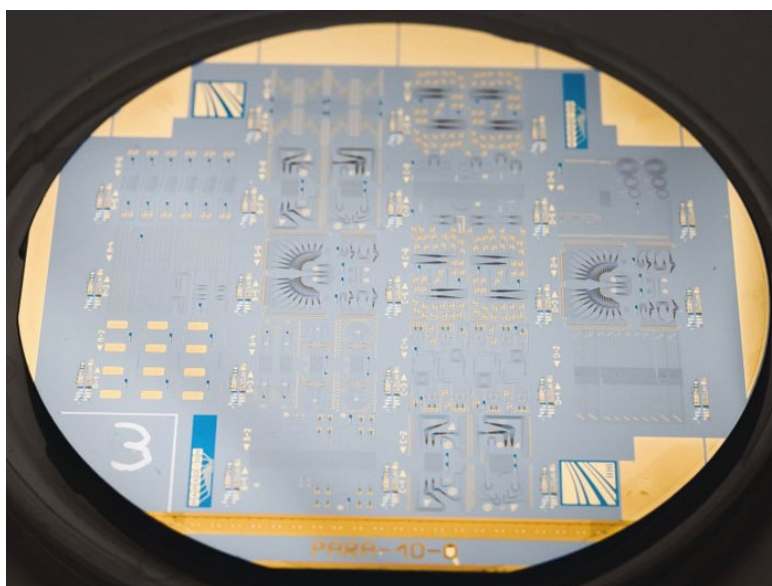

Figure 1.1 photograph of a fabricated multi-project InP wafer [2]. (Fraunhofer Institute for

Telecommunications, Heinrich Hertz Institute, HHI)

The concept of photonic integrated circuit (PIC) was proposed in 1969 [3]. It is an idea that integrates multiple photonic element together to achieve complicated functions mainly used for signal processing. Power consumption in integrated circuit includes dynamic power consumption and capacitive-load power consumption. The capacitance of line in an integrated electronic circuit does not benefit from scaling down of the circuit, and we need to apply a signal voltage to the line in order to transfer information. The power consumption can be approximately written as $E = C_l V^2$, where C_l is capacitance of interconnect line, V is minimum signal voltage. At 130 nm technology node, around 50% of total power is consumed by interconnect lines in a microprocessor [4]. The number is expected to be more than 50% if further scaling down the integrated circuits. New technology is necessary to overcome the energy density problem. The photonics is a promising key point to it for its intrinsic high working speed and low power consumption loss in interconnects. An example of fabricated photonic chips is shown in Figure 1.1.

Introducing photonics into electronics is challenging because fabrication process and basic material are quite different. Currently, integrated circuit with silicon-based photonics is achievable. Figure 1.2 shows an electro-optic system on a chip [5]. Over 70 million transistors and 850 photonic components are integrated. It is a demonstration of the concept and can work well. However, total size of the chip is larger than conventional electronics, because the size of conventional optical devices is typically ~mm order, three orders larger than electronic devices. In order to increase the degree of integration, it is important to solve the mismatch between the electronics and photonics.

A complete optical interconnect includes modulated optical source, passive components to route light, a photodiode for detection, and driving circuits. It is difficult to realize active devices (mainly emitters) by silicon platform now. That is why there is no embedded light source in the example in Figure 1.2. Small light sources used in on-chip optical interconnect with low power consumption of < 10 fJ per bit [6] attracted much attention in recent years. How to integrate III-V material-based active device into silicon platform is another big problem and is out of range of this thesis. I would like to focus on small light source next.
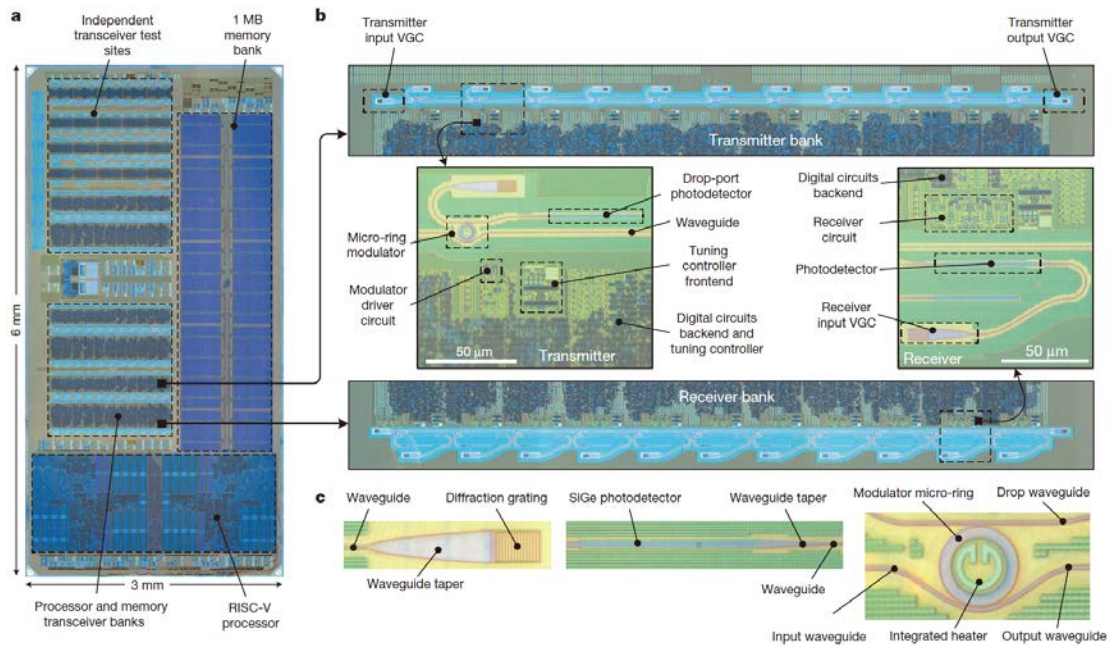
Figure 1.2 The electro-optic system on a chip [5]

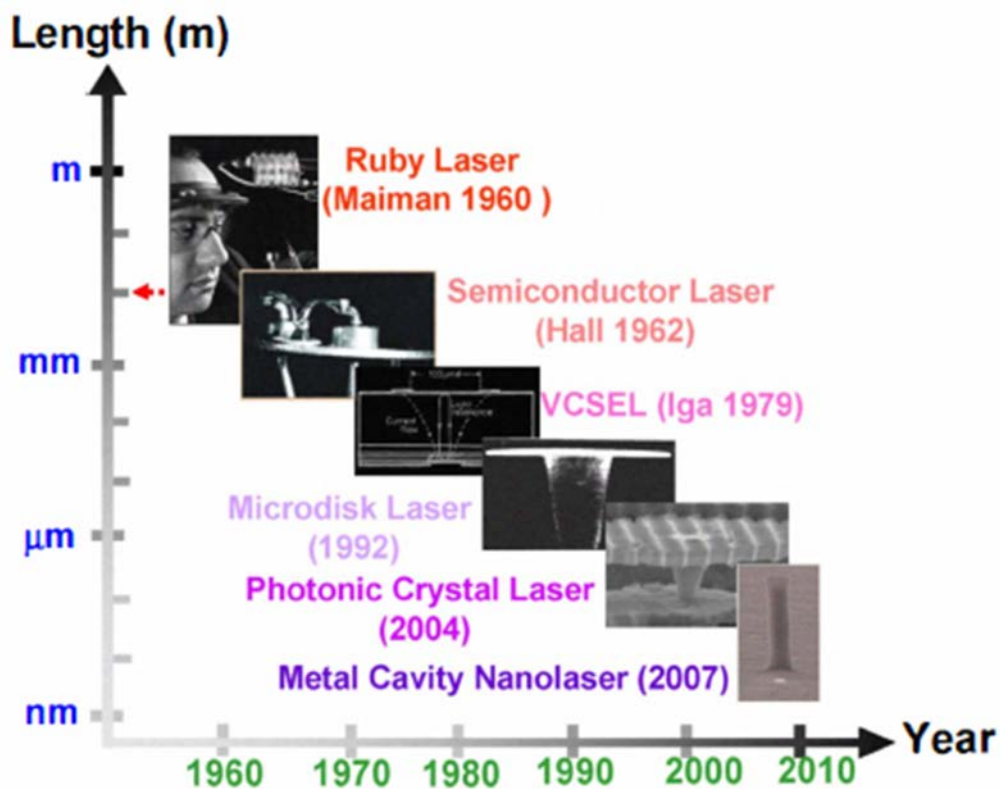## 1.2 A brief history of nano-laser

Figure 1.3 development of laser. [7]

The first solid working laser was a ruby laser made in 1960 [8]. No one could have

imagined how the laser would be used today. They were bulky with complicated structure. Semiconductor laser was born 2 years later [9]. The invention of vertical-cavity surface-emitting laser (VCSEL) in is 1980s [10]. A 1300 nm wavelength GaInAsP/InP material is used for active region. One dimension of laser resonator shrank to several micrometers. This is a big step in miniaturization. From the 1990s, further improvements came out next to next, such as microdisk laser [11] and photonic crystal laser [12].

Microdisk laser can easily reach Q factor at order of ~10^6. However, its so-called whisper-gallery mode travels around the circumference of disk, is difficult to couple with a straight waveguide. In addition, its performance highly depends on surface roughness of disk's sidewall as light energy concentrates along it. Scattering loss could be large if the edge is not smooth. Thirdly, the evanescent field of whisper-gallery mode could cause cross talk with other nearby component, this limits integration density.

Photonic crystal laser is a high Q laser as well. Low threshold current of 4.8 μA and modulating energy of 4.4 fJ/bit are achieved [13]. It needs wide spread periodic structure to acquire high reflectivity, so total footprint is large. Microdisk and photonic crystal laser are excellent but not fitted to high-density on-chip photonic integrated circuits.

Up to this point, dimension of laser dramatically shrank to orders of wavelength. However, further miniaturization is limited by diffraction limit while the devices are consist of dielectric. Light cannot be confined inside a volume which is smaller than its wavelength because intrinsic characteristic of electromagnetic waves.

People have realized surface plasmon-polaritons [14] in early time. It is a phenomenon that electromagnetic oscillation coupled with the oscillation of electrons in metals a phenomenon. From the view of energy, it is energy exchange between electromagnetic field and kinetic energy of electrons. Thus, the electromagnetic field can be localized in a volume smaller than wavelength, but at the cost of high loss. A part of the energy will change to heating because the scattering of electrons. So people did not try to use plasmonics in lasers. Until 2007, by the help of metal, a first sub-wavelength laser was demonstrated [15]. Figure 1.4 shows the structure of the sub-wavelength laser. The material of pillar from bottom to top is p-InP, u-InGaAs, n-InP, n-InGaAs, which

forms a heterojunction. Diameter of pillar is ~260 nm, thickness of active layer is 300 nm. Whole pillar is covered by gold. Light is confined inside the pillar as shown in Figure 1.4(c). The device achieved lasing at 77 K with an injection current of 7 μA. Although the device worked at a cryostat, it opened a new possibility of small lasers.
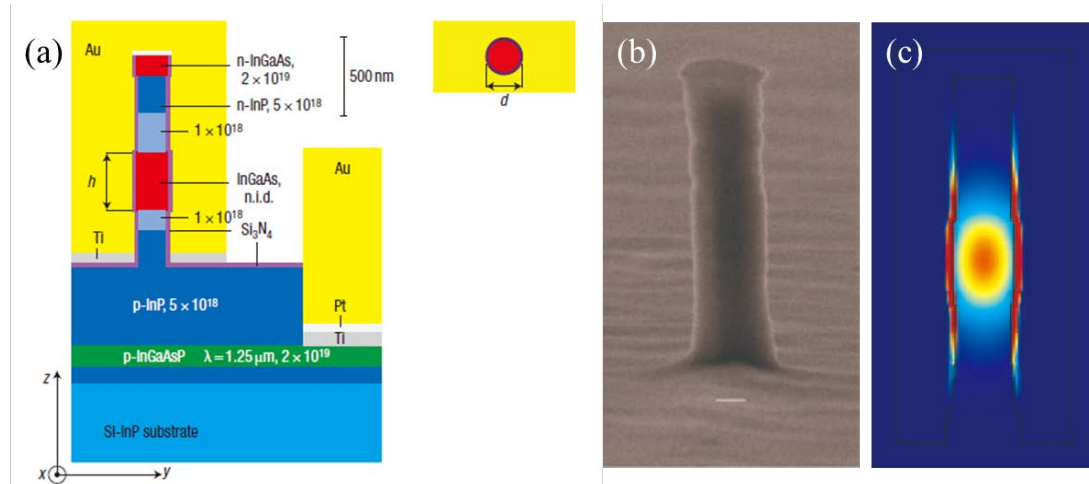

Figure 1.4 (a) Structure of the cavity formed by a semiconductor pillar encapsulated in gold. (b) Scanning electron microscopy (SEM) image of a fabricated pillar. The scale bar represents 103 nm. (c) Simulated electric-field intensity plot of the optical mode in the fabricated pillar.

Another continuous wave sub-wavelength metallic cavity laser with electrical pumping was demonstrated in 2013 at room temperature [16]. The structure of device is shown in Figure 1.5. The size of reported laser is $1.15 \times 1.39 \times 1.7$ μm^3 with a Fabry-Perot like resonating mode in TM polarization. Threshold is 1.2 mA, not at μA because metal is lossy than expected at room temperature. It is an evidence that the material gain could compensate the loss of metal.
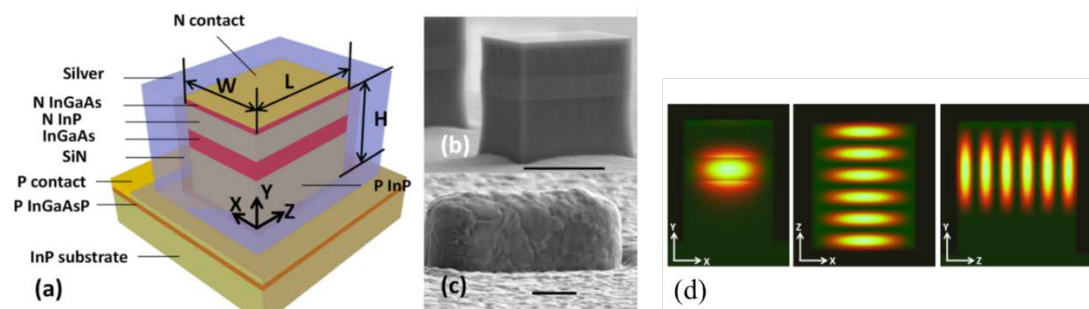

Figure 1.5 Structure of sub-wavelength metallic cavity laser with electrical pumping.

The examples mentioned above both used metal to enhance confinement of light. A laser could even be as small as 100 nm order [17] if using plasmonic mode. As shown in

Figure 1.6, a CdS nanowire is placed on MgF$_2$ coated silver substrate. Inside the gap of CdS and silver, a plasmonic mode is supported and propagates along longitude direction. Cross-section of the plasmonic mode is only 38×5 nm^2. Lasing under optical pumping was demonstrated. Although plasmonic mode is not compatible to dielectric mode widely used in photonics, its' extremely strong mode confinement and high β-factor make it very attractive.
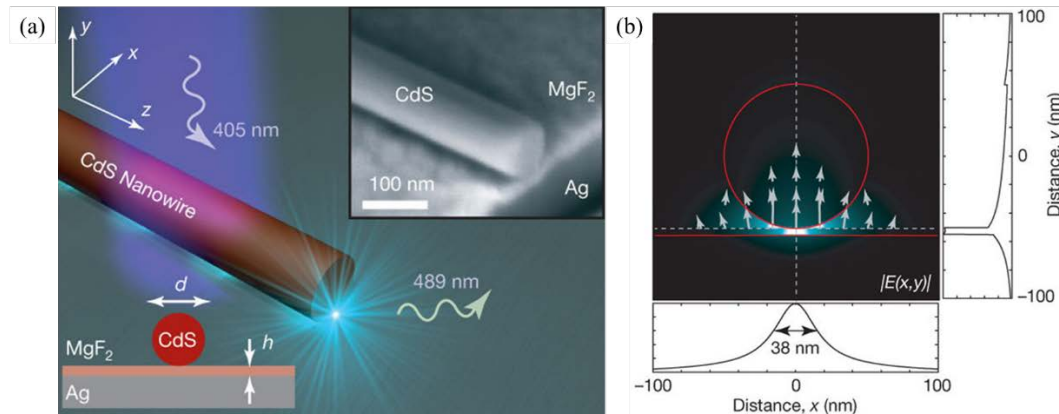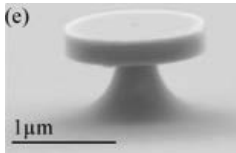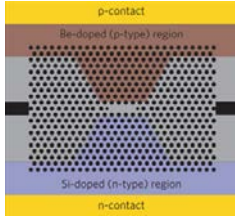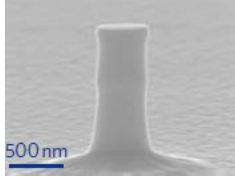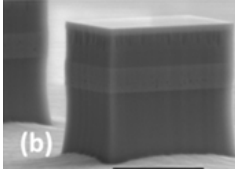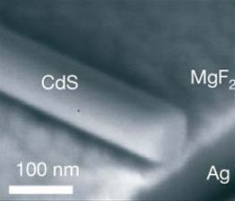

Figure 1.6 (a) The plasmonic laser consists of a CdS semiconductor nanowire on top of a silver substrate, separated by a nanometre-scale MgF2 layer of thickness h. (b) electrical intensity distribution of the plasmonic mode.

Vertical cavity surface emitting Laser (VCSEL) is also a promising technology. Since its' optical oscillation is along vertical direction, it is hard to realize monolithic integration in one chip. Therefore, our discussion will not include VCSEL in this thesis. We summarized several types of small lasers in Table 1-1. It is always trade-off between scaling down and performance.

Table 1-1 Summary of small laser technology so far

Laser type	Image	Q factor	Size	Confinement	Couping with waveguide
Microdisk [18]		~10^6	~10 μm	weak	Difficult

Photonic crystal [19]		~10^6	~10 μm	Strong	Difficult
Metallic Cylinder [15]		10^2	Sub μm	Strong	Difficult
Metallic FP cavity [16]		10^2	~1 μm	Strong	Relatively easy
Plasmonic laser [17]		null	~100 nm	Strong	Extremely difficult

Metal-clad laser and plasmonic laser have low cross talk with nearby components. Among them, metal-clad Fabry-Perot cavity has advantage of moderate coupling efficiency with dielectric waveguide, is a promising light source for on-chip interconnects.

1.3   On-chip light source

As mentioned above, there are significant progress in designing and making wavelength-scale lasers in the past few years. Their small size and low energy consumption are desired in next-generation photonics. However, it is challenging to integrate such small lasers with waveguides. Firstly, radiation pattern of small cavity tends to be divergent, especially for micro-disk and plasmonic lasers. Due to rotation-asymmetry, the whisper-gallery mode irradiates energy to every direction equally. Plasmonic mode has large spatial mode mismatch with dielectric mode. Photonic crystal laser has been studied for quite long time, and latest study achieved low energy consumption as 4.4 fJ per bit [20]. The main problem comes from its' complicated

structure. Although photonic crystal laser could integrate with waveguide by wafer bonding method [21], it is difficult to realize monolithic integration with multiple devices. In the sense of integration, metal-clad FP cavity might be a good candidate because of its' Fabry-Perot like mode, which is easy to couple with waveguide. An adittional advantage is that the whole fabrication could be realized through standard semiconductor fabrication process.
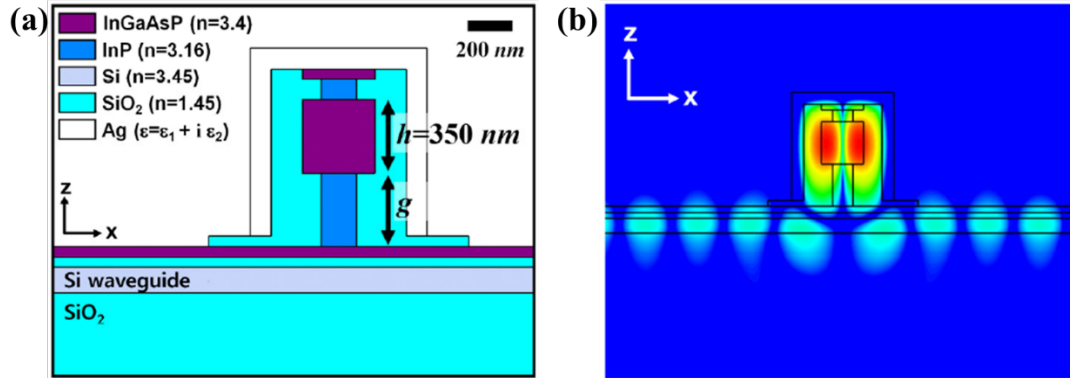

Figure 1.7 Schematic image, (a) device structure and (b) optical field of waveguide coupling of a nano-cavity [22].

There are several numerical studies on waveguide coupling of small lasers [22] [23]. An example of waveguide coupling is shown in Figure 1.7. A nano-cavity is placed on silicon waveguide made on SOI wafer. Light inside cavity transfers to waveguide by mode coupling. The coupling efficiency and total external efficiency is 76% and 4% after optimized in simulation.

Waveguide-coupled nano-LED was reported [24]. There are several issues need to be solved to achieve waveguide-coupled nano-laser. Higher material gain is necessary in nano-cavity comparing to traditional laser because of its' low quality factor. That means the required current density is higher than traditional laser. High current density causes serious self-heating problem, enhanced Auger-recombination and lower emission rate. This is also the reason why threshold of nano-laser is usually higher than calculation. The most critical reason is the metal-induced loss. There is no epitaxial growth method of metal so far. The quality of metal film is not well through sputtering or vacuum evaporation, making fabricated device's performance far below calculation. Non-radiative recombination induced by surface defects is a big problem for small laser cavity because its surface-to-volume ratio is much higher than conventional lasers [25]. Besides these

problems relating to material properties and fabrication technologies, designing of cavity is important as well. Since extracting light from cavity will in turn further reduce cavity's quality factor, engineering the coupling efficiency between laser cavity and waveguide becomes important.
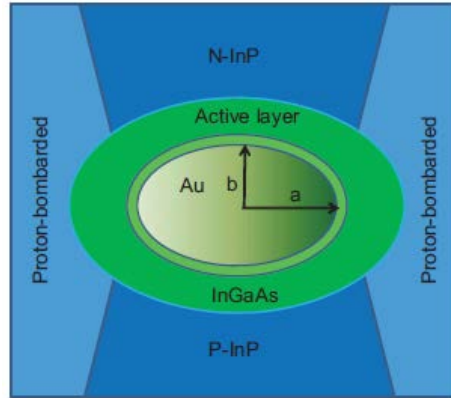

Figure 1.8 Schematic of nano-laser (spaser).

Some researchers pointed out that the threshold current of a spaser (Au spheroid covered by active InGaAs, shown in Figure 1.8) is always on the scale of 10^{-5} A [26]. It is not a good idea to reduce cavity volume too much because the resulting high current density will be a pain. On the other hand, for the application that does not require high degree of coherence, a nano-LED is still attractive. For example, an on-chip system may not need wavelength division multiplexing but cares energy cost most. The main benefits of shrinking the laser are low power consumption and high speed. By rigorous calculation based on rate equations, optical and electronic density-of-states, a subwavelength-scale LED is able to work at a speed as high as a few tens GHz [27] [28], which is better than copper wire interconnect, good enough for most application. According to the calculation, operation speed can be over 100 GHz if cavity is deep subwavelength-scaled. But that is beyond fabrication technology we have today. Jacob B. Khurgin [29] compared a spaser with VCSEL and made a conclusion that threshold current density of a spaser is at least three orders higher than VCSEL due to lossy metal. Gary Shambat [30] demonstrated a directly modulated photonic crystal nano-cavity LED working at 10 GHz with less than 1fJ per bit energy cost. The fabricated device is shown in Figure 1.9. The nano-cavity is intrinsically single-mode featured. Most of spontaneous emissions are emitted into the cavity mode. Thus, coupling efficiency will be much higher than traditional LED when

coupled to a waveguide. The coupling efficiency can reach 60% for a plasmonic-mode cavity bonded to a waveguide [31]. In addition, nano-LED performance is very robust while taking account the uncertainty of fabrication process.
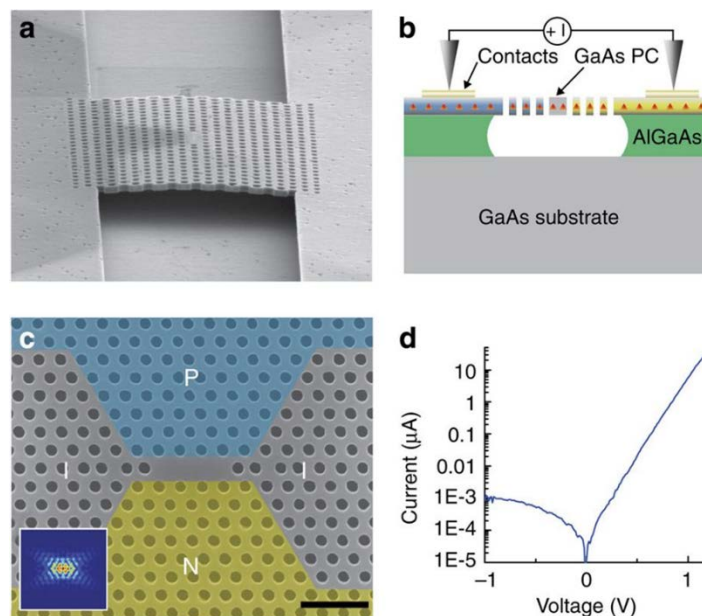

Figure 1.9 Schematic of photonic crystal nano-cavity LED. (a) Scanning electron microscope image of a device. (b) Vertical cross-section layout of device. (c) Top view of device with doping area depicted. (d) Measured I-V curve.

1.4 Objective and structure of this thesis

Much progress has been made in nano-light source field. Many papers discussed integration with waveguide as well. However, it remains a problem. Improvement is needed in designing of (a) emitter cavity and (b) waveguide coupling. In this work, in order to make optimized designing, we did theoretical study of electromagnetic field behavior in nano-cavity, explored difficulties in practical fabrication. There are two main objectives in this thesis:

(1)   Demonstrated a capsule-shaped [32] [33] optical pumping sub-wavelength metal-clad laser, proved its advantage to rectangular one. The details of capsule-shaped cavity will be discussed in Chapter 4 .

(2)   Trial fabrication of waveguide-coupled sub-wavelength metal-clad laser. We tried to make use of successfully demonstrated laser in objective (1) to reach this target.

The dissertation is organized as following:

In Chapter 1 , a brief background of small lasers is introduced.

In Chapter 2 , physics of metal-clad small lasers is illustrated, including the role of metal and difficulties of the device.

In Chapter 3 , I will introduce fabrication process used in this research and discuss important points in device fabrication.

In Chapter 4 , I will show the design and experiment results of capsule-shaped cavities, with comparison to rectangular ones.

In Chapter 5 , design and analysis of waveguide-coupled sub-wavelength laser are discussed, as well as experiment results.

In Chapter 6 , I will summarize all the work, and discuss what should be done in future to improve the performance of device.

Chapter 2   Basic of small lasers

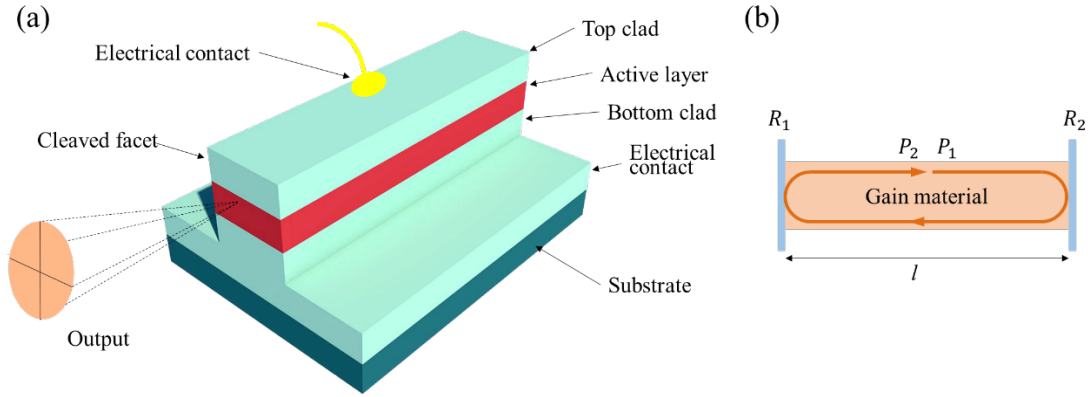## 2.1   Principle of normal semiconductor lasers

Figure 2.1 (a) Structure of a typical commercial semiconductor laser. (b) Schematic diagram of light travelling back and forth inside laser resonator.

● Macro view of lasing mechanism

Figure 2.1(a) is structure of a typical commercial semiconductor laser. Figure 2.1(b) shows the round-trip of light inside laser resonator. Semiconductor forms a strip waveguide, including a n active layer in it. Active layer emits light when current injected. Emitted light travels in the waveguide back and forth, reflecting at cleaved facets. Cleaved facet works as a mirror, whose reflectivity is around 0.3. Assume P_1 is optical power inside resonator, P_2 is optical power after one round-trip.

$$P_2 = P_1 exp(-2\alpha l)R_1 R_2 \tag{2-1}$$

Where α is average distributed loss if $\alpha > 0$, gain if $\alpha < 0$; l is length of resonator; R_1 and R_2 are reflectivity of mirror. We define

$$L \equiv gl + \alpha l - \ln\sqrt{R_1 R_2} \tag{2-2}$$

Where g is the gain. g can be regarded as absorption loss when $g > 0$, which is the usual case. For some special material, g is minus when current injected. Such material can amplify light and used in laser.

The power P_2 can be rewritten as

$$P_2 = P_1 exp(-2L) \tag{2-3}$$

In a working laser, power remains the same, $P_2 = P_1$. This requires $L=0$. Solve the equation we get

$$g = \frac{1}{l}\ln\sqrt{R_1 R_2} - \alpha \equiv g_{th} \qquad (2\text{-}4)$$

g_{th} is threshold gain that compensate all the loss during light oscillation.

Another important definition is Q factor. It is a dimensionless value that describes damping rate of resonator. It is defined as

$$Q = \frac{\omega P}{-dP/dt} \qquad (2\text{-}5)$$

Where ω is angular frequency of light, P is stored energy in optical cavity, $-dP/dt$ is power dissipation rate. Solve the P from equation we have

$$P(t) = P(0)exp\left(-\frac{\omega t}{Q}\right) \qquad (2\text{-}6)$$

In the frequency domain,

$$\Delta f_{\frac{1}{2}} = \frac{f_c}{Q} \qquad (2\text{-}7)$$

Where $\Delta f_{\frac{1}{2}}$ is half width of spectrum of optical resonator, f_c is center wavelength of peak. High Q leads to narrow half width.

Q factor is closely related to propagation loss of the waveguide and reflectivity of mirror, which is determined by physic structure of optical resonator.

● Micro view of laser rate equation

Laser diode is well described in terms of carrier and photon densities by the rate equations.

$$\frac{dN}{dt} = \frac{\eta_i I}{qV_A} - \frac{N}{\tau} - R_{st} \qquad (2\text{-}8)$$

$$\frac{dN_p}{dt} = \Gamma R_{st} + \Gamma\beta_{sp}R_{sp} - \frac{N_p}{\tau_p} \qquad (2\text{-}9)$$

Where N is carrier density; η_i is current injection efficiency; I is injected current; q is charge of one electron, V_A is volume of cavity, N_p is photon density, Γ is confinement factor, R_{sp} is spontaneous emission rate. R_{st} is stimulated emission rate, this is related to the gain factor g mentioned above. β_{sp} is spontaneous emission factor representing the ratio of spontaneous emission that coupled into resonating mode. τ is lifetime of carrier; τ_p is lifetime of photon in bulk. $\frac{N}{\tau}$ is total carrier combination rate, consisting of R_{sp}, R_{st}

and non-radiative combination R_{nr}.

Rate equations is a model that describes relation between carriers and photons in time domain. By setting $dN/dt = 0$ and $dN_p/dt = 0$, we can get steady state of a working laser diode. We can get dynamic response of laser diode by solving the equation numerically.

- Difficulties in reducing size of laser

There are two issues if laser cavity is not big enough.

First is diffraction limit. As shown in Figure 2.1(b), light confined in the resonator reflects many times from the mirrors. The resulted forward wave and backward wave interferes with each other. If their wavelength satisfies equation $2n_{eff}L = m\lambda$, where n_{eff} is effective refractive index, L is length of resonator, λ is wavelength, m is natural number, their nodes and antinodes will be positioned at same place. Their energy will be added together to form a steady oscillation called standing wave. It is also called longitude mode of resonator. The energy of those waves that do not satisfy the phase condition will be cancelled out by each other. Actually, perpendicular to propagating direction, the light should also satisfy this phase condition in lateral direction. This particular light field in lateral plane is called transverse mode. Since the minimum of m is 1, take $n_{eff} = 3$, $\lambda = 1550$ nm for example, any dimension of resonator should be larger than 250 nm.

Second limit comes from material gain. From equation (2-2) and (2-3), when the oscillation inside resonator reach steady state, we have $L = 0$. Suppose average distributed loss is 0, we then have $R_1 R_2 exp(-2g_m L) = 1$, $L = ln\sqrt{R_1 R_2}/g_m$. g_m is property of material and has an objective maximum. R_1 and R_2 are reflectivities of mirrors. Suppose $g_m = 500$ cm^{-1}, $R_1 = R_2 = 0.9$, the length of resonator should be larger than 2 μm.

It is hard to get high reflectivity through dielectric interface. Bragg grating is a good choice, 99% reflectivity is obtainable at a long distance. It is not feasible for a nano-cavity.

In a real dielectric resonator, even though a very high reflectivity is obtained, only a part of backward light reflected at mirror would couple back into resonator according to mode coupling theory. To get a good coupling efficiency the lateral dimension of resonator should be larger than wavelength scale.

Next, I would like to introduce how to overcome this problem by introducing metal.

2.2 Toward nano-scale photonics

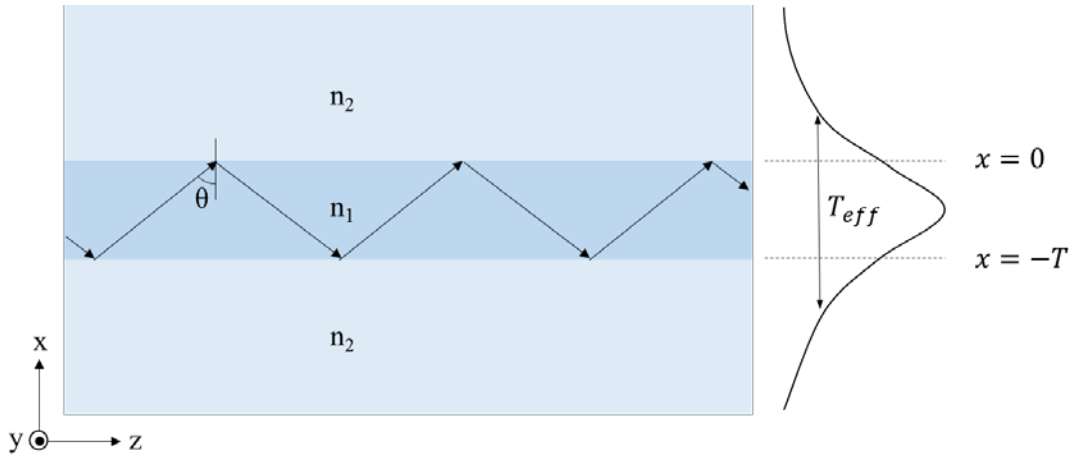### 2.2.1 Step index dielectric waveguide

Figure 2.2 Schematic diagram of a 2-dimension step-index waveguide and electrical field distribution of its fundamental mode.

Normally strip waveguide is used as oscilation cavity in semiconductor laser. For simplicity, I consider a symmetric 2-dimension waveguide. As shown in Figure 2.2, core index is n_1 and clad index is n_2 ($n_1 > n_2$), core width is T. Considering the TE mode only which propagates along z direction, Its Helmholtz equation can be written as

$$\frac{\partial^2 E_y}{\partial x^2} + (k_0^2 n^2 - \beta^2)E_y = 0 \qquad (2\text{-}10)$$

$$H_x = -\frac{\beta}{\omega\mu_0}E_y \qquad (2\text{-}11)$$

$$H_z = -\frac{1}{j\omega\mu_0}\frac{\partial E_y}{\partial x} \qquad (2\text{-}12)$$

Where ω is angular frequency; $k_0 = 2\pi/\lambda$ is called wave-number; n is refractive index and $n = n_1(-T < x < 0)$, $n = n_2(x > 0 \text{ or } x < -T)$; $n = \sqrt{\varepsilon_r}$, ε_r is relative permittivity; $\beta = k_0 n_1 \sin\theta$ is effective propagation constant. We can solve the

equations at each area and have

$$E_y = E_c exp(-\gamma_c x), \qquad x > 0 \qquad (2\text{-}13)$$
$$E_y = E_f \cos(k_x x + \varphi_c), \quad -T < x < 0 \qquad (2\text{-}14)$$
$$E_y = E_s exp[\gamma_s(x + T)], \quad x < -T \qquad (2\text{-}15)$$

Where

$$\gamma_c = \gamma_s = k_0\sqrt{n_1^2 sin^2\theta - n_2^2}, \; k_x = k_0\sqrt{n_1^2 - n_1^2 sin^2\theta} \qquad (2\text{-}16)$$

Because of the symmetric index distribution here, we have $\gamma_c = \gamma_s$. Effective index is defined as $n_{eff} = n_1^2 sin^2\theta$.

Consider continuity condition of E_y and H_z, when $x = 0$,

$$E_c = E_f \cos \varphi_c, \; \tan \varphi_c = \gamma_c/k_x \qquad (2\text{-}17)$$

when $x = -T$,

$$E_s = E_f \cos(k_x T - \varphi_c), \; \tan(k_x T - \varphi_c) = \gamma_s/k_x \qquad (2\text{-}18)$$

Combining the equations above, we get eigen value equation for the TE mode,

$$k_x T = (m + 1)\pi - \tan^{-1}\left(\frac{k_x}{\gamma_s}\right) - \tan^{-1}\left(\frac{k_x}{\gamma_c}\right) \qquad (2\text{-}19)$$

Where m is called mode number, $m = 0, 1, 2$, and so on, all the integer that satisfies $n_2 < n_1 sin\theta < n_1$. For a given waveguide structure, only several specific modes exist. Figure 2.2 shows an electrical field distribution of fundamental mode ($m = 0$). From the equation (2-4) and (2-6), the electrical field does not stop at boundary of waveguide core, but extends into clad layer, decaying exponentially. The effective boundary is usually defined as the position where electrical field decay to 1/e of that at core boundary. Therefore, the effective waveguide width is

$$T_{eff} = T + \frac{1}{\gamma_s} + \frac{1}{\gamma_c} \qquad (2\text{-}20)$$

It is dependent on the index difference between core and clad and the width of core. The larger $n_{diff} = n_1 - n_2$ is, the stronger confinement is. For an example, take $n_1 = 3.4$, $n_2 = 3.17$, T = 2 μm, wavelength λ = 1.55 μm, solve the equation numerically, we get $n_{eff} = n_1^2 sin^2\theta = 3.385$, $\frac{1}{\gamma_s} = 2\pi\lambda/\sqrt{n_1^2 sin^2\theta - n_2^2} = 0.134\lambda = 0.21\mu m$, $T_{eff} = 2.42\mu m$. Effective width gets smaller when width of waveguide decreases. On the other hand, confinement of waveguide becomes weak as well, leading to large field penetration into clad layer. Figure 2.3 is calculation result of effective width of a dielectric waveguide when core width varies. When waveguide width is 1.0 μm or 0.5 μm, the effective mode width is close

to physical width. However, when width comes to 0.1 μm and 0.2 μm, the effective mode width does not decrease but remains over 0.4 μm. It is difficult to make effective mode width to subwavelength order, which is known as diffraction limit.
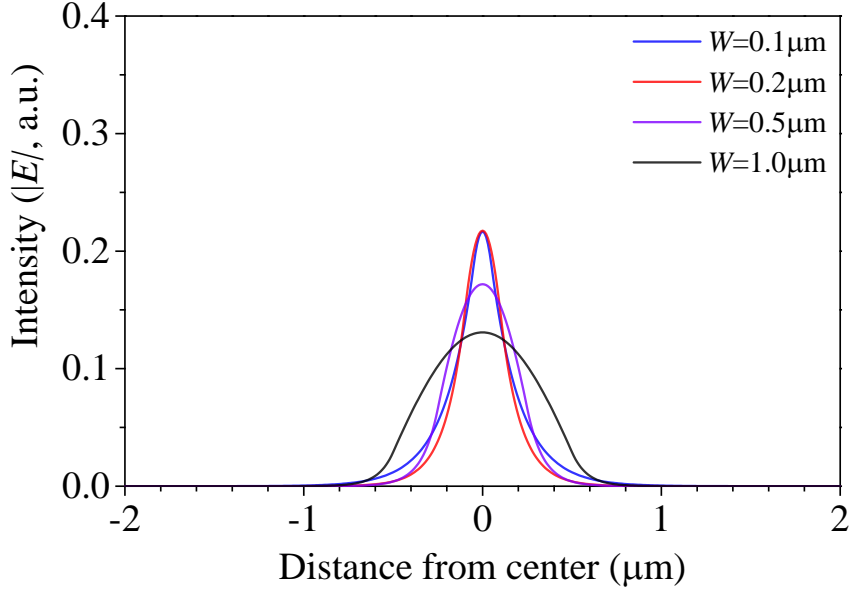

Figure 2.3 Electrical field distribution of fundamental mode of different waveguides. *W* is width of waveguide. $n_1 = 3.17$, $n_2 = 1$, λ=1.55 μm. All the |*E*| are normalized to $\int |E|^2 dx = 1$.

2.2.2 Metal-insulator-metal (MIM) waveguide

The use of material with negative permittivity is a promising way too overcome diffraction limit. Electromagnetic waves couples with the oscillation of electrons at metal surface, energy of electromagnetic field exchanges with electron's kinetic energy. As a result, electromagnetic waves are located in nano-scale spaces. This has been known as surface plasmon polaritons [34].

Let us look at the examples below to grab an intuitive image. Now we set clad layer as metal with permittivity of ε_2, core layer as dielectric with permittivity of ε_1, as shown in Figure 2.4. The difference is that $\varepsilon_2 < 0$ and $\varepsilon_1 > 0$.

● Dielecric mode

Of course, a normal dielectric mode can be supported in such geometry while core layer is sufficient thick. We can find out the optical mode of it, replacing n with ε and using the same analysis as section 2.2.1. We omit the calculation here. We would like to

discuss a component in waveguide effective width, $\frac{1}{\gamma_s} = 2\pi\lambda/\sqrt{\varepsilon_1 sin^2\theta - \varepsilon_2}$. Suppose

the metal is lossless, ε_2 has no imaginary part. Note that for typical metal, absolute value $|\varepsilon_2|$

is usually very large, far bigger than that of dielectric. Thus, field penetration in metals is quite
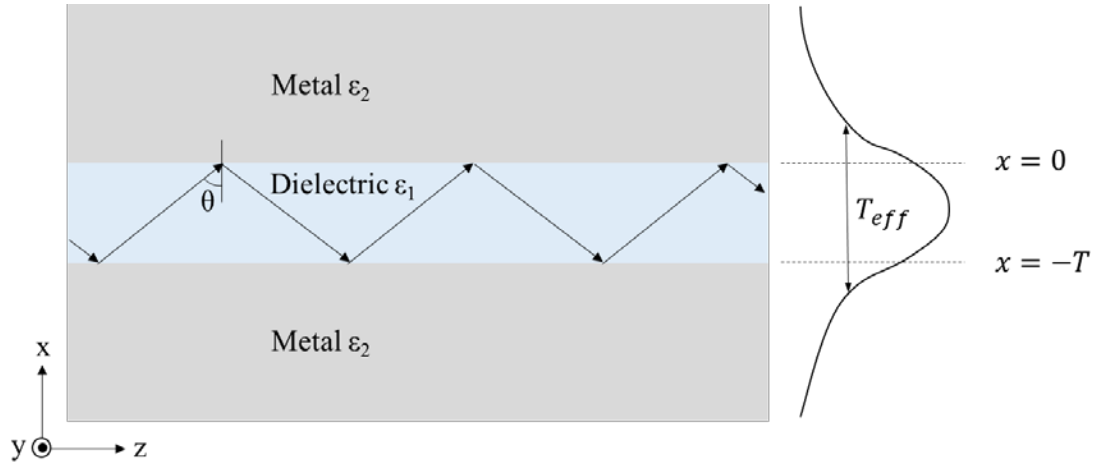
small, typically nanometer scale.

Figure 2.4 Geometry of metal-insulator-metal waveguide, dielectric is sandwiched between two metal layers. Right hand side is a dielectric mode.

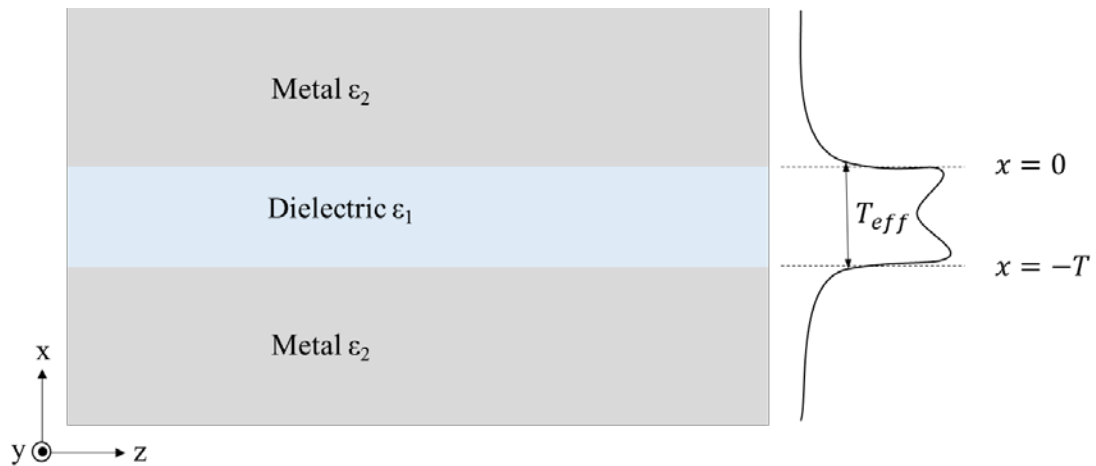● Surface plasmon-polaritons (SPPs)

Figure 2.5 Geometry of metal-insulator-metal waveguide, dielectric is sandwiched between two metal layers. Right hand side is a typical electrical distribution of surface plasmon polaritons.

We consider TM mode in this waveguide. (TE polarized SPPs does not exist because

electrical field tangential to metal surface is zero.) Its Helmholtz equation can be written

as

$$\frac{\partial^2 H_y}{\partial x^2} + (k_0^2\varepsilon - \beta^2)H_y = 0 \qquad\qquad (\text{2-21})$$

$$E_x = \frac{\beta}{\omega \varepsilon \varepsilon_0} H_y \qquad\qquad (\,2\text{-}22\,)$$

$$E_z = \frac{1}{j \omega \varepsilon \varepsilon_0} \frac{\partial H_y}{\partial x} \qquad\qquad (\,2\text{-}23\,)$$

Taking consideration of physics meaning, we can solve these equations for each area. The different point is that electrical field in core layer is located at $x = 0$ and $x = -T$, decaying exponentially. The solution for surface plasmon polaritons should be

$$H_y = H_c exp\big(-\gamma_c x\big), \qquad x > 0 \qquad\qquad (\,2\text{-}24\,)$$
$$H_y = H_{f1} exp(k_x x) + H_{f2} exp([-k_x(x+T)]), \quad -T < x < 0 \qquad (\,2\text{-}25\,)$$
$$H_y = H_s exp\big[\gamma_s(x+T)\big], \quad x < -T \qquad\qquad (\,2\text{-}26\,)$$

Where

$$\gamma_c = \gamma_s = k_0\sqrt{\varepsilon_1 sin^2\theta - \varepsilon_2}, \; k_x = k_0\sqrt{\varepsilon_1 - \varepsilon_1 sin^2\theta} \qquad (\,2\text{-}27\,)$$

Consider the continuity of H_y and E_z, we leave out intermediate expression, dispersion relation can be finally written as

$$\tanh\frac{k_x}{2} = -\frac{\gamma_c \varepsilon_1}{k_x \varepsilon_2} \qquad\qquad (\,2\text{-}28\,)$$

$$\tanh\frac{k_x}{2} = -\frac{k_x \varepsilon_2}{\gamma_c \varepsilon_1} \qquad\qquad (\,2\text{-}29\,)$$

The most interesting point of this mode is that there is no cut-off when core layer thickness decreases to even tens of nanometer [35].
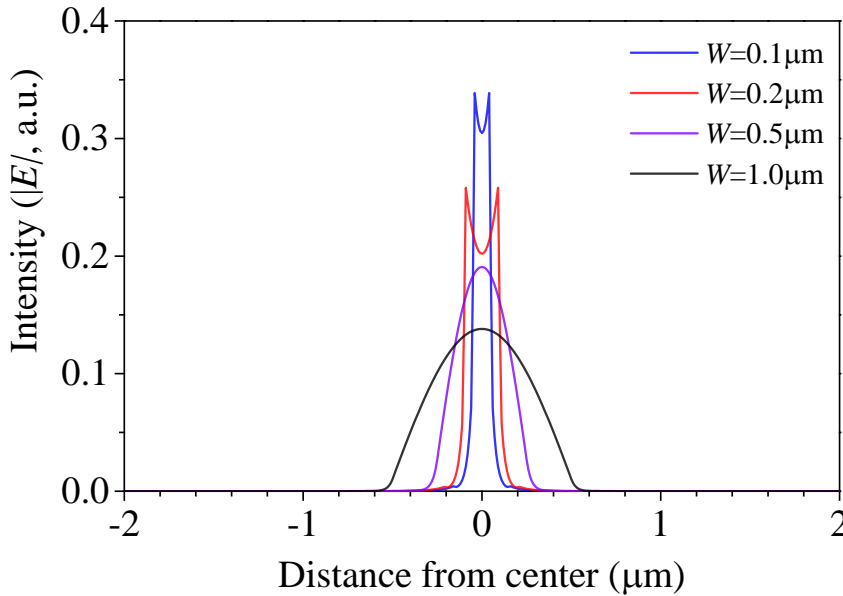

Figure 2.6 Electrical field distribution of fundamental mode in metal-insulator-metal waveguides with different width. W is width of waveguide. $\varepsilon_1 = 12$, $\varepsilon_2 = -86.6\text{-}j8.7$, $\lambda=1.55$ μm. All the $|E|$ are normalized to $\int |E|^2 dx = 1$.

Figure 2.6 shows mode distribution in a metal-insulator-metal waveguide. Unlike

dielectric waveguide, electrical field penetration into metal is only tens of nanometer. Effective mode width decreases as waveguide width decreases, at the cost of huge propagation loss. Electrical field intensity concentrated inside the dielectric slot could be very high. Some reports suggest that average energy propagation slows down near surface plasmon-polariton resonance so net gain per unit time is amplified [36], showing a possibility to compensate metal-induced loss.

2.3 Advantages of nanolaser

2.3.1 Enhanced spontaneous emission factor

Spontaneous emission factor, β_{sp} in equation (2-9), is defined as the ratio of spontaneous emission coupled into specific resonating modes to the total spontaneous emission. A laser with large β_{sp} wastes less input power into useless emission and automatically has lower threshold. Rigorous calculation of β_{sp} is very complicated and relates to quantum photonics [37] [38]. With some assumptions that decay of optical energy inside cavity is far less than the decay of emission dipoles (photons), mode volume is equal to cavity volume, resonating modes frequencies are all included in material emission spectral profile, and photons are equally emitted into each mode, a simple expression of spontaneous emission factor is given as [39]

$$\beta_{sp} = \frac{1}{p} = \frac{1}{4\pi^2} \times \frac{\lambda^3}{V_{cav}} \times \frac{\omega}{\gamma_{atom}} \qquad (\,2\text{-}30\,)$$

where p is the total number of cavity modes, V_{cav} is volume of cavity, λ and ω are wavelength and angular frequency, γ_{atom} is decay of photons, $\gamma_{atom} = \frac{1}{\tau_{atom}}$, τ_{atom} is lifetime of photons in bulk material. We can see that under a certain wavelength, β_{sp} is proportional to inverse of cavity volume (mode volume), typically at order of 10^{-5} for a common laser. For a wavelength-scale cavity with a volume of ~1.0 μm^3, total number of resonating modes are limited to 2 or 3, and the wavelength interval between different modes could be over several tens of nanometers, β_{sp} can go up to 10^{-1} order.

2.3.2 Enhanced working speed due to Purcell effect

The Purcell effect is a phenomena that spontaneous emission rate is enhanced when an atom is in a resonant cavity not in free space. The enhancement is given by [40]

$$F = \frac{3}{4\pi^2}\left(\frac{\lambda}{n}\right)^3\left(\frac{Q}{V}\right) \qquad (\,2\text{-}31\,)$$

Where λ is wavelength in vacuum, n is refractive index of cavity material, Q is quality factor, V is mode volume (cavity volume).

The rate of spontaneous emission relates to states density of electromagnetic modes and local field intensity, and it has been observed at optical frequencies [41]. It can be explained by quantum electrodynamics [42]. In a quantum view, the density of modes determines the emission rate (transition rate). When an atom is in free space, there are infinite electromagnetic modes surrounding it. If we move the atom to a resonant cavity, the local modes are changed into finite, discrete modes. The spontaneous emission rate is then enhanced by a factor, as well as spontaneous lifetime [43].

This is very useful because a dielectric one-dimension photonic crystal structure can have high β_{sp} but cannot modify spontaneous lifetime [44]. A metal-clad micro cavity is able to shorten spontaneous lifetime to below that in bulk material theoretically [43] and experimentally [24]. In principle, a laser/LED with metal-clad nano-cavity having large Purcell factor can achieve modulation speed over 10 GHz [28] [27].

Chapter 3   Device fabrication

3.1   Introduction, challenging of fabrication

Semiconductor device manufacturing has developed for decades since 1960s.The industry preferred silicon to Germanium because (1) silicon is abundant element in nature in the form of sand, making it very low cost; (2) Silicon has larger bandgap (0.7 eV) than Ge (0.2 eV), making its' thermal noise is smaller than Ge at high temperature. Thanks to the mass manufacturing of silicon, the fabrication technology of silicon developed quickly. The process nodes is 10 μm in 1971, 1.0 μm in 1985, 90 nm in 2004, and 7 nm in 2018. It is expected to be 5 nm in 2020. On the other hand, people did not pay much attention to III-V (InP, GaAs, etc.) in the past. Later, people realized that III-V has intrinsic advantages in fabricating optical active device for its' direct band, the III-V comes into researchers' sight. However, due to industrial problem, the fabrication technology is not optimized for III-V. The process nodes for III-V photonic devices is not as small as silicon. In addition, light is sensitive to the error and edge roughness induced by fabrication. Lastly, some photonic devices have unique structures differing from electronics, need non-standard process steps to realize. These factors make fabrication of optical devices harder than electronic devices.

The difficulties in this work mainly lie in two aspects. First is the cylindrical mirror of the cavity whose radius is only 1 ~ 2 μm. We need to fabricate such structure with high precision. Otherwise, the performance of real device would be far from simulation. Second problem is metal coating of the cavity. We deposit metal film to cavity sidewalls by vacuum evaporation. During the deposition device is tilted by 60 degree and rotated 90 degree or 180 degree to another side after one side is done. The optical property of metal film is dependent on the quality of evaporation [45]. The above problems are key factor to device performance. The repeatability of devices are not good if we cannot deal with these issues, and any discussion or comparison of results from different experiments would be nonsense.

In this chapter, I would like to talk about what I have done to improve the fabrication process. It is the prerequisite of this research.

3.1.1 Process for light injection cavity

Table 3-1 Layer structure of wafer for optical pumping laser

Layer	Material	Thickness (nm)	Doping (cm^{-3})
1. P-contact	P-InGaAs	100	$> 1 \times 10^{19}$
2. Upper clad	P-InP	600	5×10^{17}
3. Etch stop	U-InGaAsP	8	
4. Buffer	U-InP	50	
5. Active core	U-InGaAs	350	
6. Buffer	U-InP	50	
7. Bottom clad	N-InP	700	5×10^{17}
8. Etch stop	N-InGaAsP	8	5×10^{17}
9. Bottom clad	N-InP	250	1×10^{18}
10. N-contact	N-InGaAsP	100	$> 5 \times 10^{18}$
11. Buffer	N-InP	300	$> 5 \times 10^{18}$
12. Substrate	InP		

The fabrication process is shown in Figure 3.5. This is to confirm the idea that capsule-shaped cavity has better Q-factor than rectangular one. We use optical pumping instead of current injection to avoid heating problem, which could make experiment more complicated. Photon luminescence is checked before fabrication. The measured data is plotted in Figure 3.1. Measurement is done at room temperature, using continuous wave 1030 nm pumping laser. Emission center is around 1575 nm. As stated in later chapter, target resonating wavelength is 1550 nm in our design.
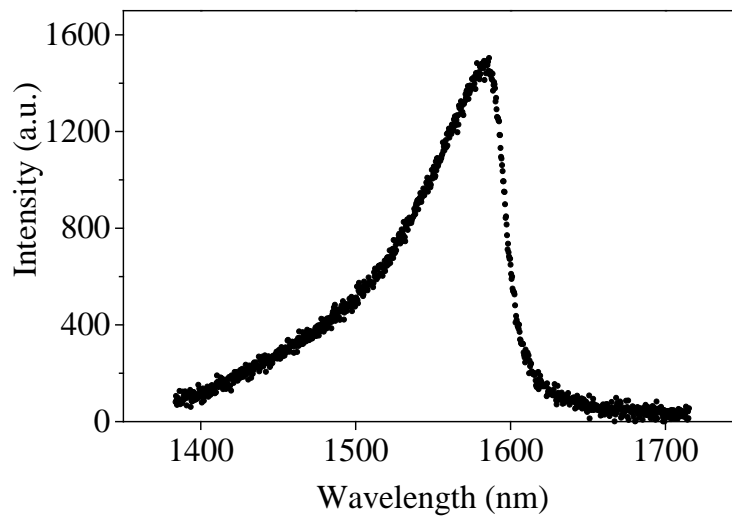
Figure 3.1 Photon luminescence of active layer U-InGaAs

(a) Clean wafer. Wafer is dipped into acetone for 1 minute, then rinsed by isopropyl alcohol (IPA) and ethanol for 1 minute, respectively. After that, put wafer on 200℃ hotplate for 10 minutes to dissipate any liquid molecule remains on wafer surface.

(b) Deposit SiO_2 and Cr as hard mask during dry etching. 400 nm thick SiO_2 is deposited by plasma enhanced chemical vapor deposition (PECVD) during 350℃. SiO2 formed by PECVD is more robust than that formed by sputtering or vacuum evaporation, so that pattern degrades less during dry etching process. Even so the single SiO_2 layer does not meet our needs since we have to etch the InP more than 1.5 μm. Thus, we introduce bi-layer mask to increase dry etching selectivity ratio. 30 nm thick Cr is deposited on SiO_2. In our comparison experiment, the Cr layer either deposited by sputtering or vacuum evaporation shows similar robustness.

(c) Spin coat resist. HSQ is a good choice for state-of-the-art fabrication. Sub 10 nm nano-wire patterning by HSQ with good edge roughness has been reported [46] [47]. Wafer is cut into 1 cm × 1 cm pieces. Rotation speed is set as Table 3-2. 3 drops of HSQ resist are dripped onto center of sample immediately after rotation rate reach 500 rpm, using a pipet 3 cm over sample surface. It worth noting that HSQ is very sensitive to operation condition. Any changes in the underlined parameter and Table 3-2 would cause unexpected affect in resist thickness and uniformity, which result in negative consequence during lithography. After spin coating, HSQ is prebaked under

150°C for 2 minutes.

Table 3-2 Spin coating condition for HSQ

	Rotation per minute (rpm)		Ramp-up time (second)	holding time (second)
Step 1	500		5	5
Step 2	3000		5	60

(d) The EBL is done by F7000S model from Advantest company. Electron acceleration voltage is fixed to 50 kV. Dosage for 1 μm × 2 μm pattern is around 2000 μC/cm^2. Proximity effect correction (PEC) is introduced to improve patterning accuracy. The details will be illustrated in later section. After exposure, sample is dipped into NaOH/NaCl/H$_2$O solution with weight ratio of (1%:4%:95%) under room temperature for 23 seconds. Check the pattern by microscope carefully. Completion degree of develop may be different from area to area. Develop sample for 3 seconds more if develop is not completely done. Then 2 seconds O$_2$ plasma descum is necessary to remove remains of resist. Finally, check the pattern by scanning electron microscope. Make sure no residues remains, especially at edge of patterns. Measure the patterns by step meter after develop. Thickness of HSQ should be 120 ~200 nm under spin coating condition given in step (c).
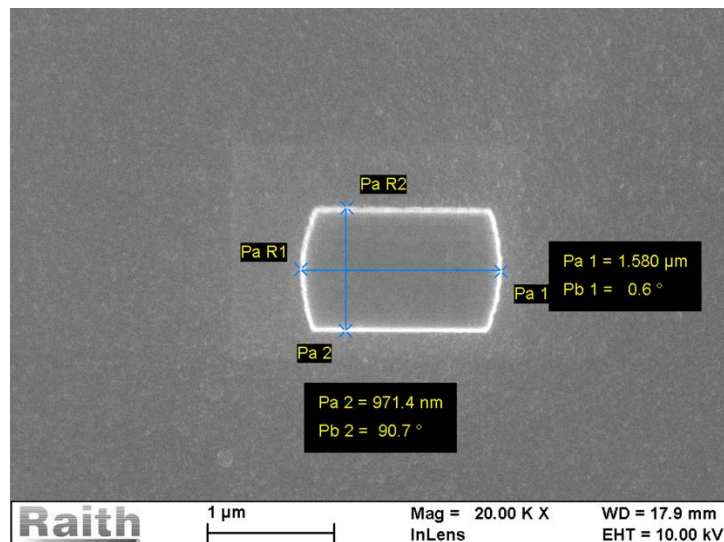
Figure 3.2 Scanning electron microscope image after develop

(e) Pattern is transferred to Cr, then to SiO$_2$, both done through dry etching. The condition of the dry etching is summarized in Table 3-3.

Table 3-3 Condition for Cr and SiO$_2$ dry etching

Etching material	Cr	SiO$_2$
Pressure (Pa)	5.0	2
Gas (sccm)	Ar/O$_2$/Cl (10/25/40)	CHF$_3$/Ar (20/10)
RF power (W)	400	80
Time	60 seconds	19 minutes
Equipment model	ICP-RIE Ulvac CE-S	Samco RIE-10NR
Etching rate	> 60 nm/min	22 nm/min

(f) Dry etch InP/InGaAs to form mesa. Since the mesa is as high as 1.5 μm, one should be very careful of etching condition. Even 2 degree side wall tilting can degrade Q factor of cavity fatally [48]. We use H$_2$/CH$_4$ to dry etch InP, which result in better surface roughness than Cl$_2$ [49]. The condition is summarized in Table 3-4. Please notice that sample surface might be dirty after step (e) with undesired residues or particles on it. It is necessary to clean it before InP dry etching. We firstly dip sample into H$_2$SO$_4$/H$_2$O$_2$/H$_2$O (1:1:50) solution for 20 seconds at room temperature to slightly remove 20 nm thick InGaAs at surface, then rinse sample twice by DI water.

Table 3-4 Condition for InP dry etching.

Etching material	InP	Cleaning
Pressure (mTorr)	15.0	75.0
Gas (sccm)	H$_2$/CH$_4$ (45/15)	O$_2$ (50)
RF power (W)	120	40
ICP power (W)	100	0
Temperature (°C)	60	60
Time	60 seconds	22 seconds
Equipment model	Oxford PlasmaPro100	
Etching rate	~80 nm for InP per cycle (60s H$_2$/CH$_4$+ 22s O$_2$) ~50 nm for InGaAs per cycle (60s H$_2$/CH$_4$+ 22s O$_2$)	

(g) Surface treatment. Cavity surface is damaged by high energy ions bombard during dry etching. The defects at surface will act as impurity recombination center, reducing radiation recombination efficiency. There are 5 steps in surface treatment.

Step 1 is O_2 plasma oxidization , with gas pressure 75 mTorr, gas flow rate 50 sccm, RF power 80 W, temperature 60°C and lasting time of 60 seconds. Step 2 is oxide removal by diluted phosphoric acid (H_3PO_4:H_2O = 1:10) for 1minute. Use HCl:H_2O (1:20) to rinse for about 10 seconds because InP will get oxidized even in DI water. This step should be done in dark, because any electrons in conductive band generated by light will cause undesired chemical reaction, making cavity surface rough. Step 1 and step 2 are repeated for 3 times. Step 3 is removing SiO_2 hard mask by buffered HF (BHF) solution. 3 minutes are enough to remove 400 nm thick SiO_2. Step 4 is slight InGaAs etching by a H_2SO_4:H_2O_2:H_2O (1:8:5000) lasts only 5 seconds. After that ultrasonic cleaning in Acetone is done to remove remaining Cr, which is not dissoluble in BHF and sticky to sample surface. HF is also good at removing oxides of InP compounds [50]. Step 5 is dipping sample into 20% $(NH_4)_2S$ solution [51] for 30 minutes. This treatment fills dangling bond with S to prevent further oxidization by O_2. Step 2, step 3 and step 4 are all done at room temperature.
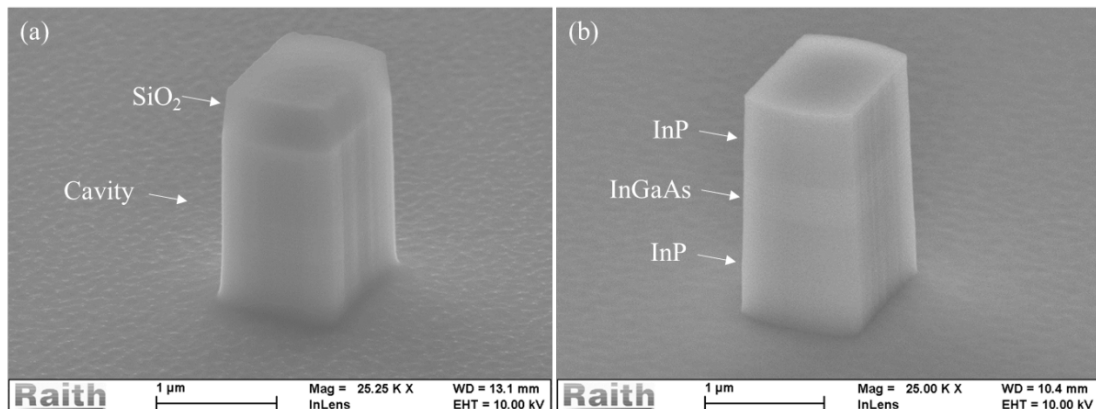
Figure 3.3 (a) cavity before surface treatment, (b) cavity after treatment. It is easily to distinguish InGaAs layer from InP by image brightness, because oxides induced during dry etching are removed. We can also see that floor in (b) is more smooth than that in (a), which suggests that surface treatment is effective.

(h) Passivation with SiO_2. Firstly, clean sample by acetone with ultrasonic wave applied. This is to make sure no particles and organic contamination on the surface. Then rinse sample with IPA and ethanol. After that, 40 nm thick SiO_2 is deposited by PECVD.

(i) Metal coating. It is better to start this step immediately after (h). Silver is deposited by vacuum evaporation. In order to cover sidewalls as well, sample is fixed to a 45 ~ 60 degree tilted holder. Since adhesion between silver and SiO_2 is weak, 2 nm of Ge

wet layer is deposited before silver. The quality of silver film is related to optical loss in cavity. High vacuum and high deposition rate are helpful to get good silver film [45]. During our experiment, silver deposition start while pressure is less than 3×10^{-5} Pa, deposition rate is 15 nm/s.
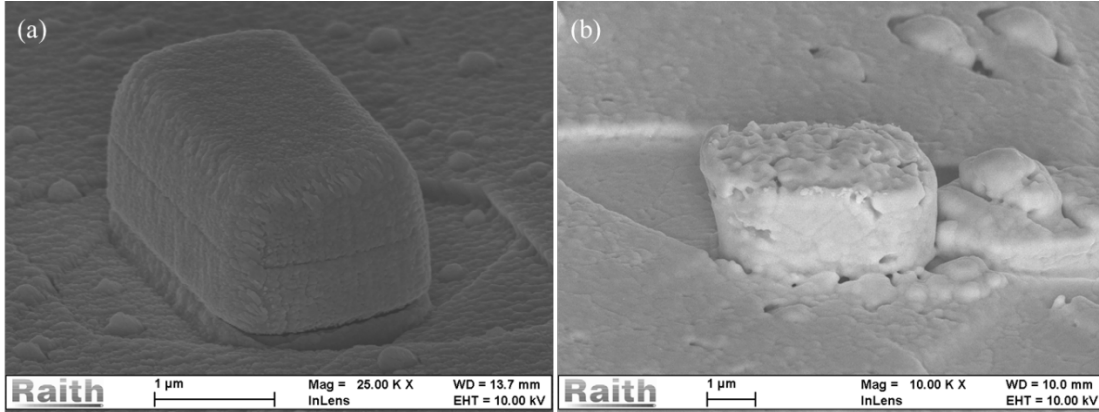

Figure 3.4 silver coating at deposition rate of (a) 0.3 nm/s and (b) 15 nm/s. The silver in (a) is formed by lots of small grains with size of several 10s nm. The grain size is several 100s nm in (b). We expect less scattering loss at SiO_2/Ag interface inside despite of worse surface roughness outside.

(j) Up to this point, device is almost finished. Because cavity is covered by metal, no light can get out from it. We need to inject and collect light from bottom. In order to protect device on surface, we spin coat polyimide PW-1230 onto sample with parameter written in Table 3-5. Prebake it at 120°C for 3 minutes. Then harden it through rapid thermal annealing. The parameter is written in Table 3-6.

Table 3-5 Spin coating condition for PW-1230 polyimide

	Rotation per minute (rpm)	Ramp-up time (second)	holding time (second)
Step 1	600	5	5
Step 2	2500	5	30

Table 3-6 Rapid thermal annealing for PW-1230 polyimide

	Start temperature (°C)	End temperature (°C)	Time (hour)
Step 1	0	120	0.5
Step 2	120	120	0.5
Step 3	120	300	1

| Step 4 | 300 | 300 | 1 |

(k) Flip over sample, stick it to silicon carrier by black wax. 1st, put silicon carrier and black wax on hotplate, heat them to 180°C. 2nd, paint black wax on carrier by cotton swab. 3rd, flip over sample, place it on melted black wax. Paint black wax to sidewall of sample carefully, make sure sidewalls are covered completely. 4th, lift carrier away from hotplate, wait for black wax getting hard again. Then sample sticks to carrier firmly.

(l) Remove substrate. The thickness of wafer we used is 325 μm. 1st, polish substrate for about 250 μm. 2nd, use HCl to etch InP, H_2SO_4/H_2O_2 to etch InGaAsP until device layer.

(m) Ready for measurement.

InGaAs	SiO2	HSQ	Polymer
InP	Cr	ZEP520A	Black wax
InGaAsP	LOR7B	Ag	Silicon

(a) Clean wafer
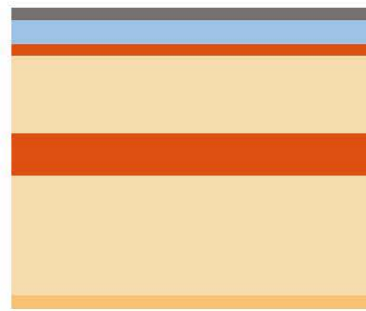
(b) Deposit SiO$_2$ and Cr
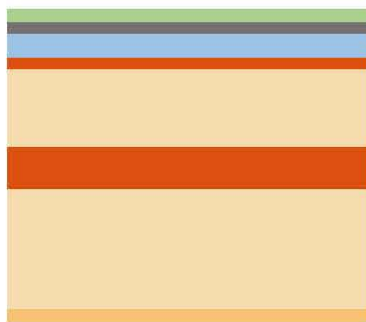
(c) Spin coat HSQ resist
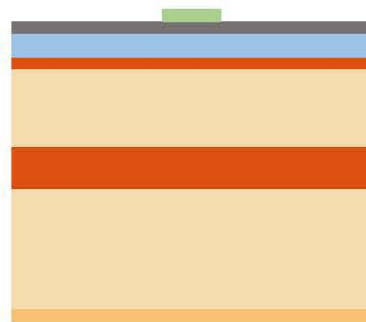
(d) EBL expose
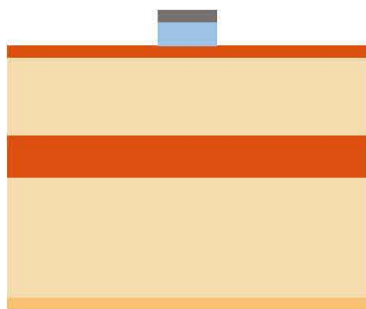
(e) Dry etch Cr and SiO$_2$
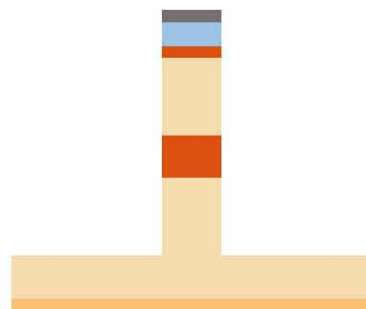
(f) Dry etch InP, InGaAs
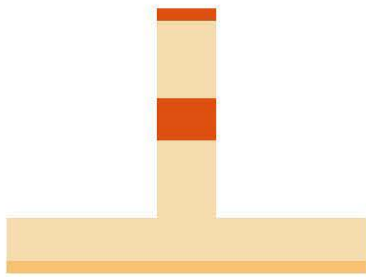
(g) Remove hard mask, clean surface
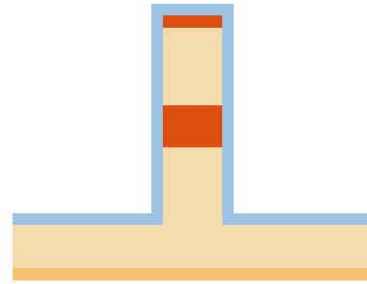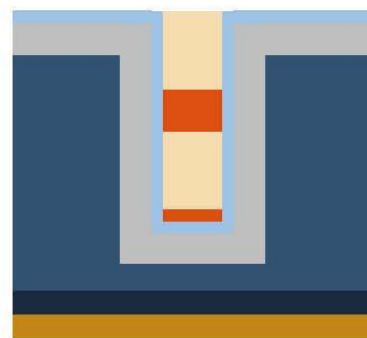

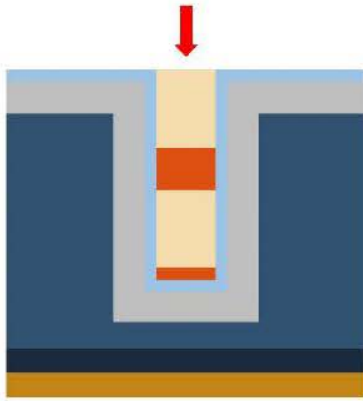**(h)** Passivation with SiO$_2$
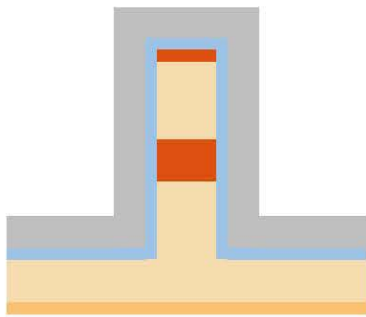
(i) Deposit Ge and Ag
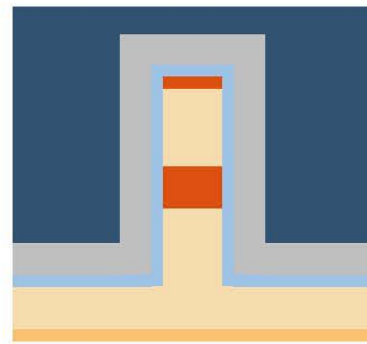
(j) Cover cavity by polymer
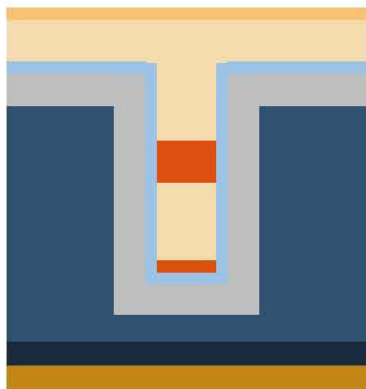
(k) Flip the sample, over, stick it to silicon carrier by black wax

(l) It etch substrate InP

(m) Inject light and test

Figure 3.5 Fabrication process of light-injection cavity

3.1.2 Process for waveguide-coupled device

Table 3-7 Layer structure of wafer for waveguide-coupled device

Layer	Material	Thickness (nm)	Doping (cm^{-3})
1. P-contact	P-InGaAs	100	$> 1 \times 10^{19}$
2. Upper clad	P-InP	480	5×10^{17}
3. Etch stop	U-InGaAsP	8	
4. Buffer	U-InP	20	
5. Active core	U-InGaAs	450	
6. Bottom clad	N-InP	400	5×10^{17}
7. Waveguide core	N-InGaAsP	350	5×10^{17}
8. Bottom clad	N-InP	200	5×10^{17}
9. Bottom clad	N-InP	250	5×10^{18}
10. Etch stop	N-InGaAsP	100	$> 5 \times 10^{18}$
11. Buffer	N-InP	50	$> 5 \times 10^{18}$
12. Substrate	InP		

The fabrication process flow of waveguide-coupled device is shown in Figure 3.11. Layer structure of used wafer is shown in Table 3-7. Comparing to Table 3-1, active core thickness is 100 nm larger. We expect thicker InGaAs layer provide larger optical gain to compensate extra loss induced by waveguide. Index of InGaAsP at 1550 nm is around 3.4,

a bit larger than 3.17 of InP. Thus, 350 nm thick InGaAsP layer is used as waveguide core, expected to offer good confinement of light.

The steps (a)~(e) are the same as that illustrated in section 3.1.1, aiming at making optical resonator. It is worth mentioning that in step (d) here, do not forget adding alignment markers for lithography of waveguide later.

(f) Spin coat HSQ resist again. The operation here is the same as step (c) in section 3.1.1. Note that after several steps of process, surface of sample is not clean as at beginning. Spin coating of resist may not good. But it is not recommended to remove resist by TMAH (2.38%) and spin coat again even if part of sample is not coated with resist well. Empirically, redoing makes things worse.

(g) Lithography with mask alignment. Since we use electron beam direct write lithography, the alignment is done through operation of controlling software. By recognizing markers on sample and setting coordination manually, we draw waveguide next to cavity. The result after this step is shown in Figure 3.6.
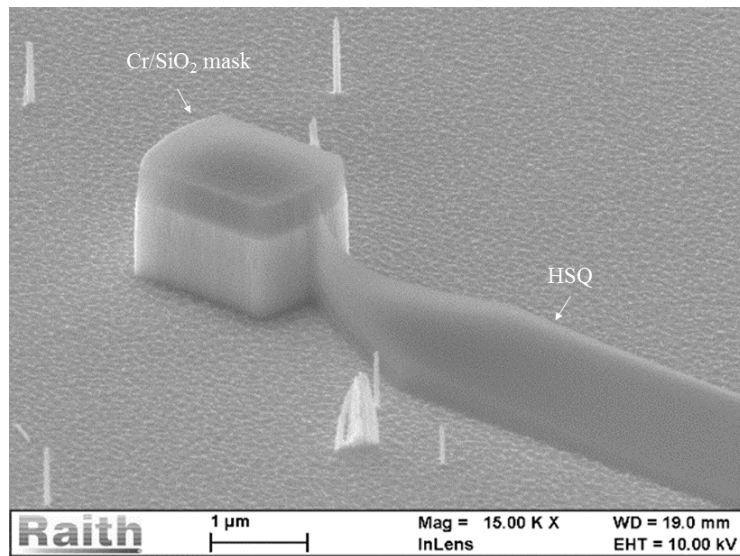
Figure 3.6 Waveguide mask formed after electron beam lithography.

(h) Dry etch waveguide. We need to etch down about 700 nm , from top of layer 7 to reach layer 9 in Table 3-7. HSQ can be regarded as quasi-SiO_2 after expose, its selectivity to InP during H_2/CH_4 dry etching is around 1:10 from experiment data. 120nm thick HSQ is capable to work as hard mask in this step. The image after this step is shown in Figure 3.7.
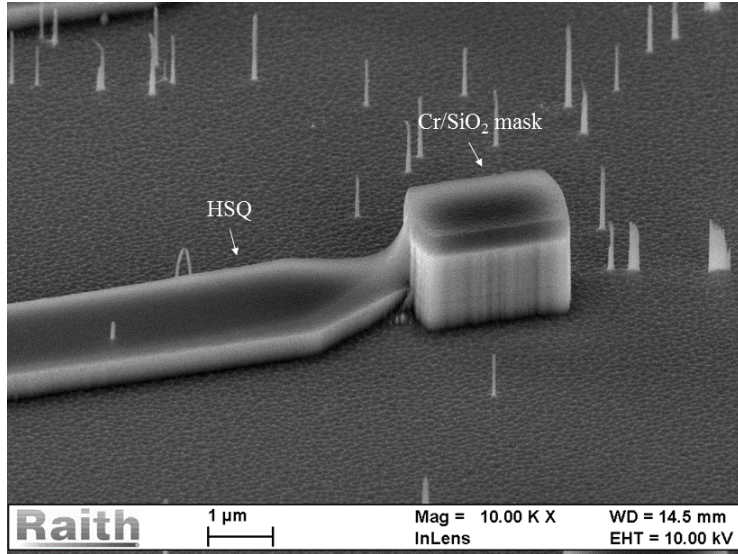
Figure 3.7 Waveguide coupled structure after dry etching.

Steps (i), (j) are the same as (g), (h) in section 3.1.1, respectively.
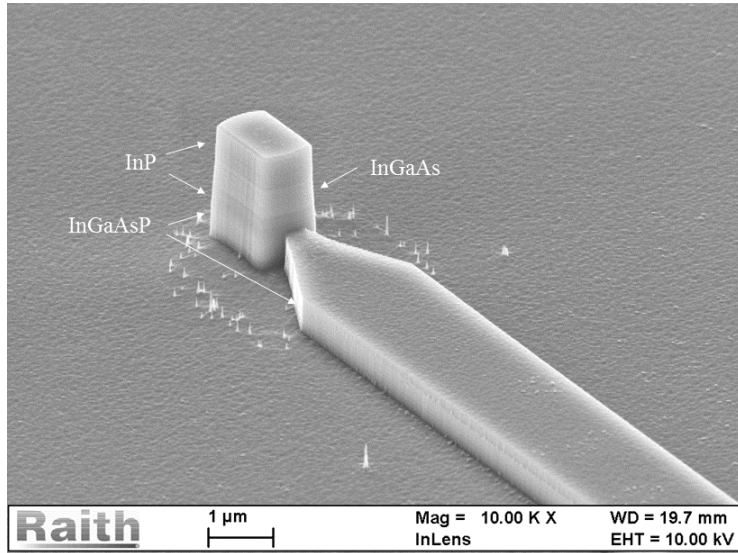

Figure 3.8 Waveguide coupled device after surface treatment. Layer structure can be seen clearly.

(k) Spin coat LOR7B resist for planarization. Up to this point, total height of mesa is around 2200 nm. LOR7B is a type of thick resist. Its thickness is 1200 nm if spin coated under condition of Table 3-8. Bake it at 180°C for 3 minutes. Then do the spin coating again with same condition. The total thickness of LOR7B is around 2400 nm after twice spin coating. It is a bit thicker at area of mesa, so that mesa is covered completely.

Table 3-8 Spin coating condition for LOR7B

	Rotation per minute (rpm)	Ramp-up time (second)	holding time (second)

Step 1	500	5	5
Step 2	3000	5	60

(l) Dry etch back the resist to expose only top of mesa. Etching rate of resist is quite high, one should be careful about the etching time. A conservative way to do it is that etch only 30 seconds or even less each time, and check it by optical microscope. We etch back until the top is opened to air, Judging from the interference of light at mesa's top and contrast of mesa's outline. Figure 3.9 shows top of a mesa after contact open.

Table 3-9 Condition for etching back LOR7B resist

Etching material	LOR7B
Pressure (Pa)	30.0
Gas (sccm)	O_2/CHF3 (20/2)
RF power (W)	100
Time	30 seconds $\times$ 2
Equipment model	Samco RIE-10NR
Etching rate	~ 500 nm per 30 seconds
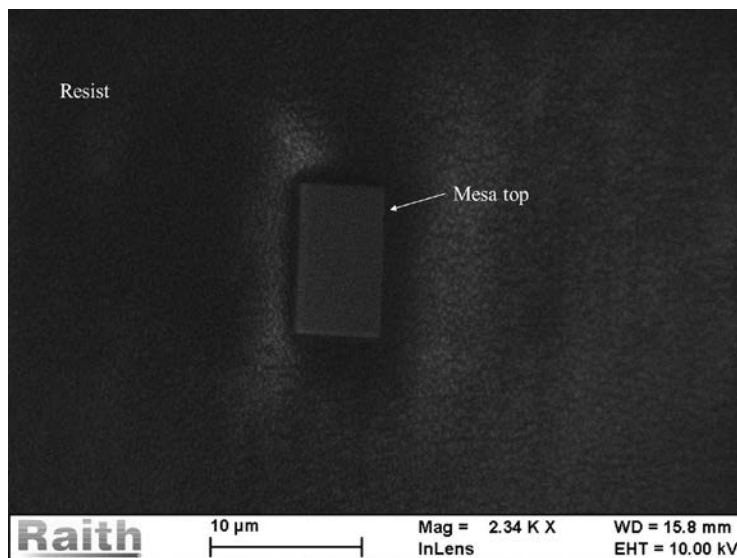
Figure 3.9 Scanning electron microscope image after contact open. Only top is exposed

(m) Dry etch SiO_2 at top of mesa to expose p-contact layer to air. Condition for etching SiO_2 here is the same as that in Table 3-3. But note that necessary time here is only 2.5 minutes.

(n) Remove all resist remains on surface by TMAH (2.38%). After that, check sample

surface by scanning electron microscope. Sometimes, unknown residues. Sometimes some residues remains (Figure 3.10a), which cannot be dissolved by TMAH (2.38%). In that case, one can try O_2 plasma cleaning in Table 3-10. Do not forget to treat sample with $H_2SO_4:H_2O_2:H_2O$ (1:8:5000) solution for 5 seconds again to reduce contact resistance after oxidization. A sample image after this step is shown in Figure 3.10b.

Table 3-10 Condition for cleaning resist residue

Etching material	LOR7B residue
Pressure (Pa)	50.0
Gas (sccm)	O_2 (50)
RF power (W)	300
Time	2 minutes
Equipment model	Samco RIE-10NR
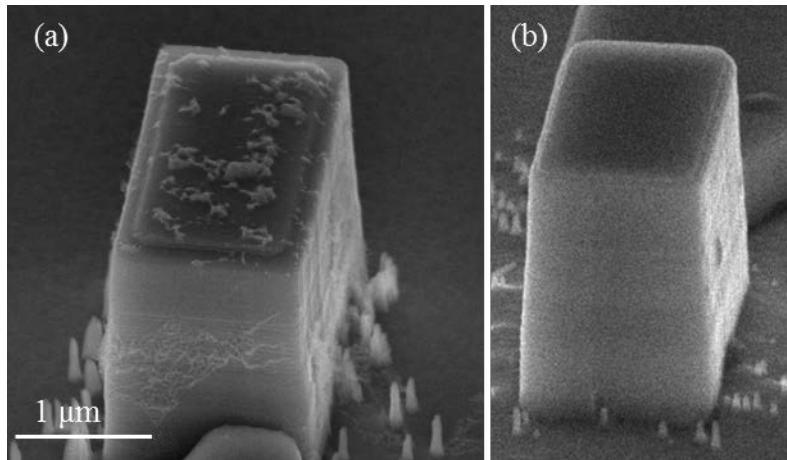
Figure 3.10 (a) residues after resist removal, (b) after O_2 plasma cleaning

(o) Spin coat bi-layer resist for lift-off of electrode. Firstly 2400 nm thick LOR7B is coated as the same as step (k). Next, spin coat ZEP520A on LOR7B with the condition stated in Table 3-11. Thickness will be around 500 nm.

Table 3-11 Spin coating condition for ZEP520A

	Rotation per minute (rpm)	Ramp-up time (second)	holding time (second)
Step 1	500	5	5
Step 2	4000	5	60

(p) Do lithography again for p-contact electrode. Since highly accurate patterning is not required, equipment model Raith eLINE Plus is used. In order to reduce lithography time, following settings are preferred: dosage 30 $\mu C/cm^2$; aperture size 60 μm; accelerate voltage 10 kV; step size 0.2 μm. Make sure return settings to default after patterning. Develop sample following steps in Table 3-12. The important point is step 4. The undercut is near 9 μm when develop time is 25 seconds. Larger undercut may cause distortion of ZEP520A patterns.

Table 3-12 Condition for develop of LOR7B/ZEP520A bi-layer resist

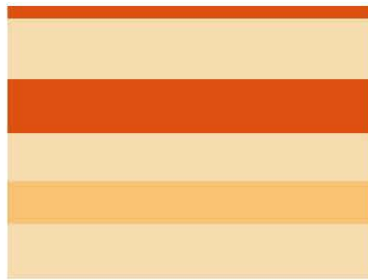| Target resist	Step	Solution	Time (second)
ZEP520A	1. Develop	ZEDN50	60
	2. Rinse	IPA	30
	3. Rinse	IPA	30
LOR7B	4. Develop	TMAH (2.38%)	25
	5. Rinse	DI water	30
	6. Rinse	DI water	30

(q) Deposit Ge/Ag as the same as step (i) in section 3.1.1. Since very thick silver film is deposited onto tilted sample, sides of sample are coated with silver as well, which will make lift-off more difficult. Thus, we use Kapton tape to cover edges of sample, preventing them from deposition.

(r) Lift off silver. Dipping sample into ZEDMAC for 24 hours at room temperature.

(s) Spin coat LOR7B for only one time, then ZEP520A, using the same condition as that in Table 3-8 and Table 3-11, respectively.

(t) Do lithography for n-contact electrode. All condition and operation are the same as in step (p), except GDS file.

(u) Dry etch insulator SiO_2 as the same as step (m).

(v) Deposit n-contact electrode. Ti/Au (20 nm / 400 nm) are deposited through vacuum evaporation. Recommended vacuum degree is 3×10^{-5} Pa, deposition rate is 0.3 nm/s for Ti and 0.3 nm/s for Au. It is better to cover edges of sample by Kapton tape, which makes later lift-off easy. A quick annealing is recommended after lift-off. To reduce contacting resistance.
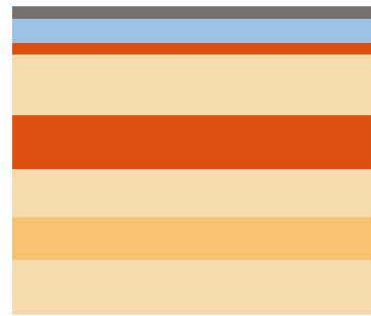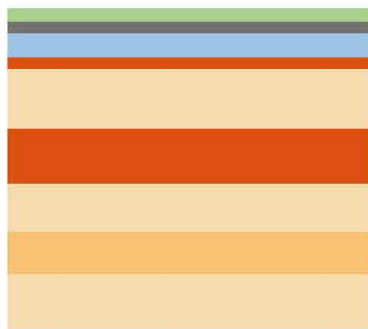
(w) Lift-off, the same as step (r).

(x) Ready for test.

(a) Clean wafer

(b) Deposit SiO₂ and Cr

(c) Spin coat HSQ resist

(d) EBL expose and develop
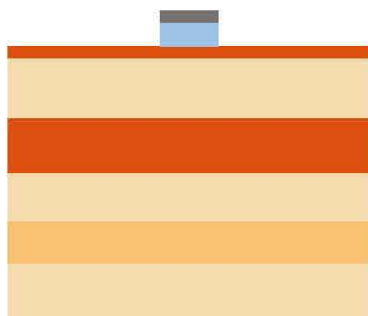
(e) Dry etch Cr and SiO₂
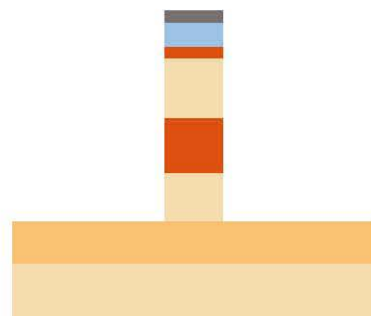
(e) Dry etch InP and InGaAs to form cavity
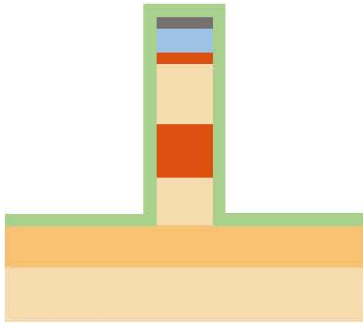
(f) Spin coat HSQ resist
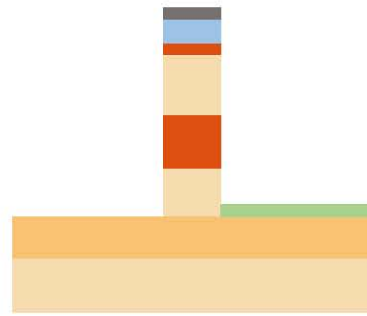
(g) EBL expose and develop
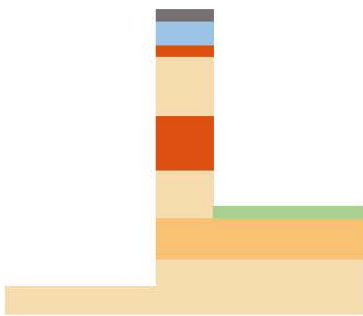
(h) Dry etch InGaAsP to form waveguide
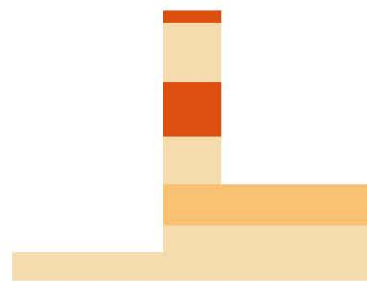
(i) Remove hard mask and clean surface
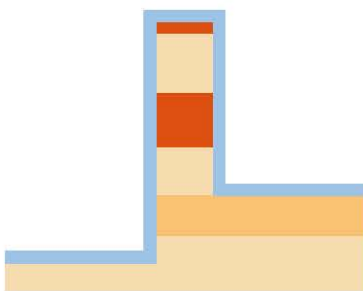
(j) Passivation with SiO$_2$ by PECVD
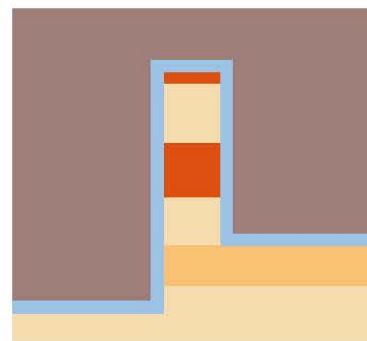
(k) Spin coat LOR7B resist
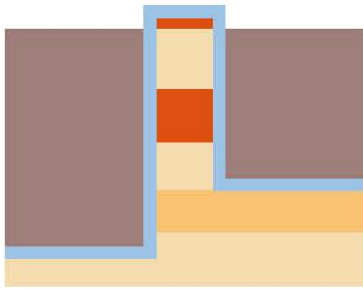
(l) Etch back resist
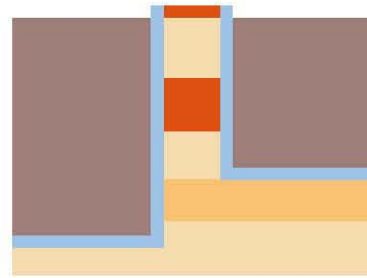
(m) Dry etch top SiO$_2$
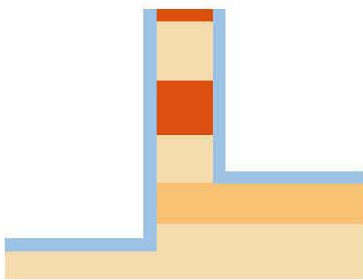
(n) Remove resist
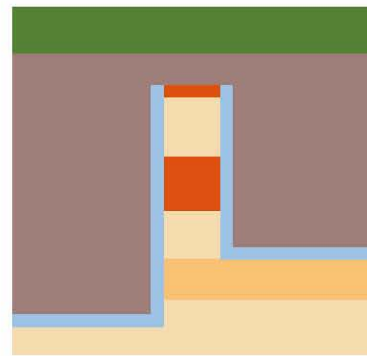
(o) Spin coat bi-layer resist LOR7B and ZEP520A
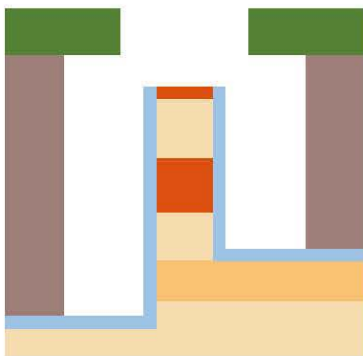
(p) EBL alignment expose for p-contact
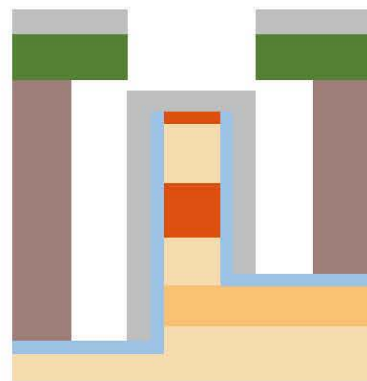
(q) Deposit 2 nm Ge and 1000 nm Ag by evaporation
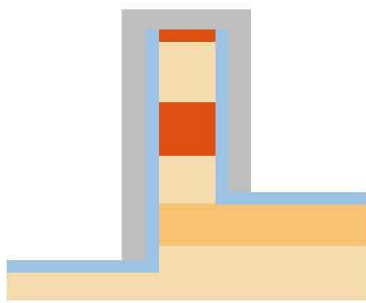
(r) Lift off
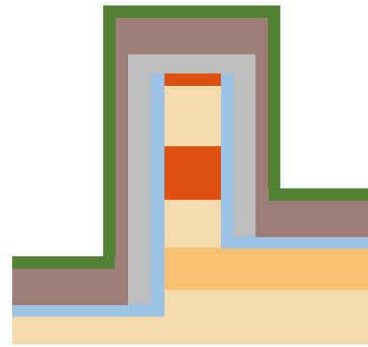
(s) Spin coat LOR7B and ZEP520A resist
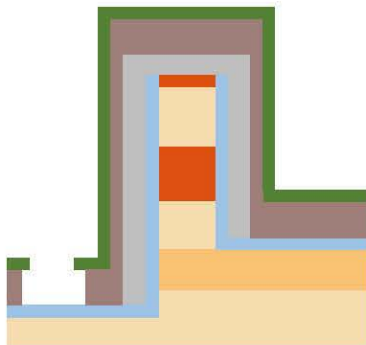
(t) EBL alignment expose for n-contact
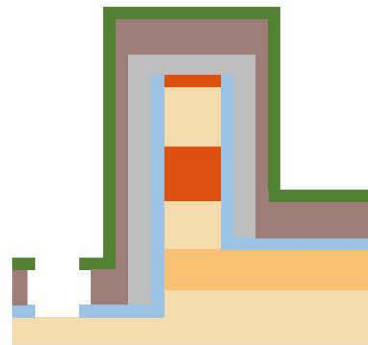
(u) Dry etch insulator SiO$_2$
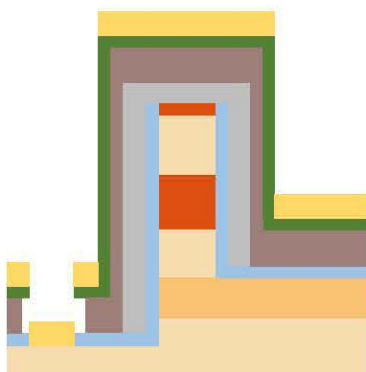
(v) Deposit 20 nm Ti and 400 nm Au
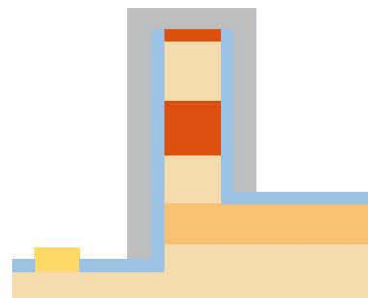
(w) Lift off
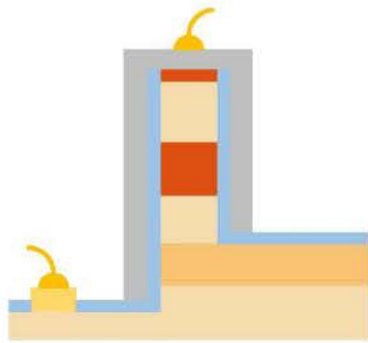
(x) Inject current and test

Figure 3.11 Fabrication process of waveguide-coupled device

3.2 Important points during fabrication process

3.2.1 Improved edge roughness with HSQ
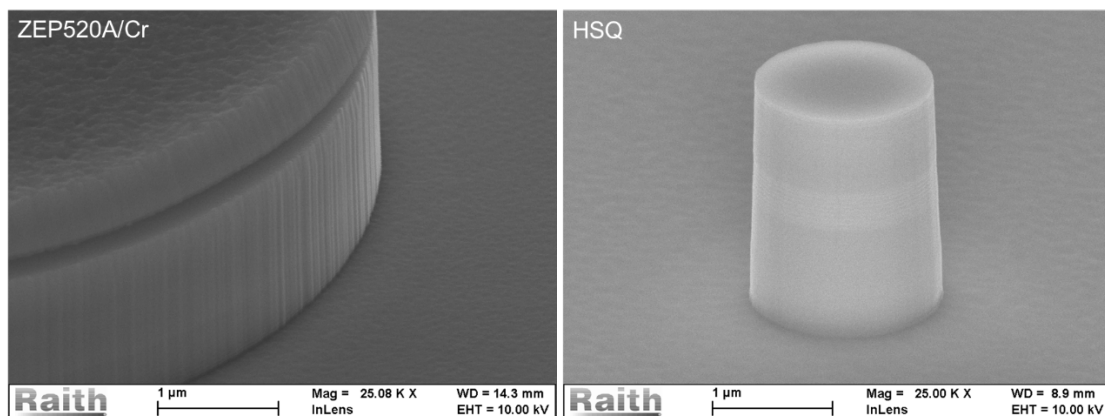
Figure 3.12 Sidewall roughness of mesa processed by using ZEP520A and HSQ.

In previous work, we used ZEP520A, a positive resist, in our electron beam lithography. Exposed part is washed away, and then a 20 nm thick chromium (Cr) layer is deposited by electron beam heated vacuum evaporation. Cr is used as hard mask during later dry etching after lift-off. Due to the nucleation mechanism during deposition [52], the metal atoms get together to form cluster first, then small island. The islands get bigger and bigger and finally form continuous film. Usually the minimum thickness for Cr to form continuous film is 20 nm. The edge roughness of Cr mask is inevitably over 20 nm, leading to a corrugated sidewall of mesa shown in Figure 3.12. Since our device is very

small, the scattering caused by corrugated sidewall will be a big problem.

In our research, we used negative resist HSQ during electron beam lithography. The exposed part is washed away, therefore the edge roughness is basically the resolution of electron beam, could be less than 10 nm. In addition, the HSQ exposed by electrons turns to quasi-SiO_2, which can be used as hard mask during dry etching. This offers an advantage in fabricating device with high accuracy, although its selectivity is less than real SiO_2. In Figure 3.12, we can see that sidewall of a mesa fabricated by using HSQ is much more smooth.
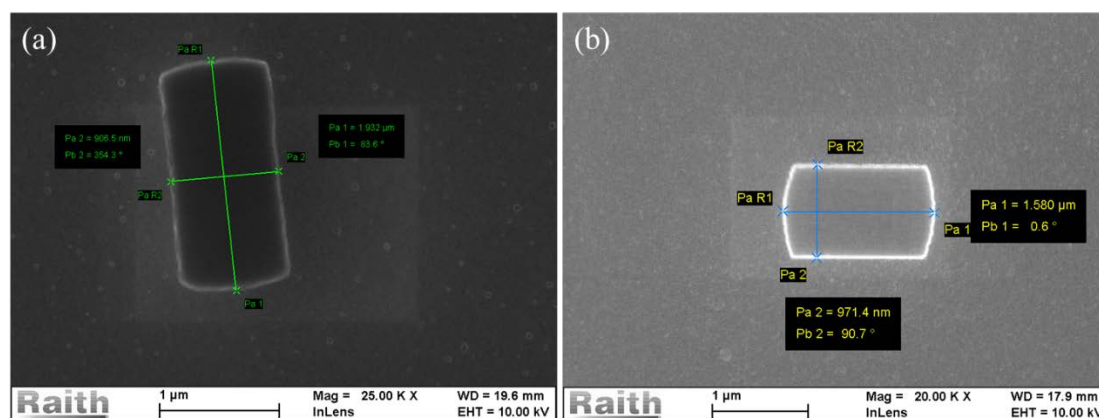
Figure 3.13 (a) HSQ developed by 2.38% TMAH with dose of 270 μC/cm^2, (b) HSQ developed by NaOH(1%wt):NaCl(4%wt):H_2O(95%wt) solution with dose of around 2400 μC/cm^2.

It is worth noting that 2.38% TMAH developer does not work very well with HSQ [53]. The sidewalls of resist are irregular and highly rough. It also occurs in our experiment, as shown in Figure 3.13(a). We tried adjusting dose from 180 to 400 μC/cm^2, but there is no improvement in edge roughness. The unexposed or slightly exposed area of HSQ resist are easily dissolved when using low dose because of the instability of dangling Si bonds [47]. High exposure dose can make Si bonds more stable, increase the contrast between exposed and unexposed areas. In this case, stronger developer is necessary. High contrast pattern with dose as high as several thousand was obtained by using KOH and NaOH solution [53] [54]. We get good developed pattern by using NaOH solution experimentally (Figure 3.13(b)).

3.2.2 Proximity effect correction in HSQ patterning

During electron beam lithography, the scattering of electrons due to interaction with resist (forward scattering) and substrate (backward scattering) leads undesired broadening of designed pattern. This is called proximity effect. The energy density profile in resist due to one point exposure is called point spread function (PSF). Usually the profile is approximated by summing two Gaussian distribution [55] (forward scattering and backward scattering, respectively)

$$f(r) = C_1 exp(-(r/B_1)^2) + C_2 exp(-(r/B_2)^2) \qquad (3\text{-}1)$$

Where C1, C2, B1, B2 are constants, r is distance from center point. This equation can be rewritten as [56]

$$f(r) = \frac{1}{1+\eta}\left(\frac{1}{\pi\alpha^2}exp(-(r/\alpha)^2) + \frac{\eta}{\pi\beta^2}exp(-(r/\beta)^2)\right) \qquad (3\text{-}2)$$

Where r is distance from center point, η is ratio of back scattering energy to forward scattering energy, α is the forward scattering range parameter, β is the backward scattering range parameter.
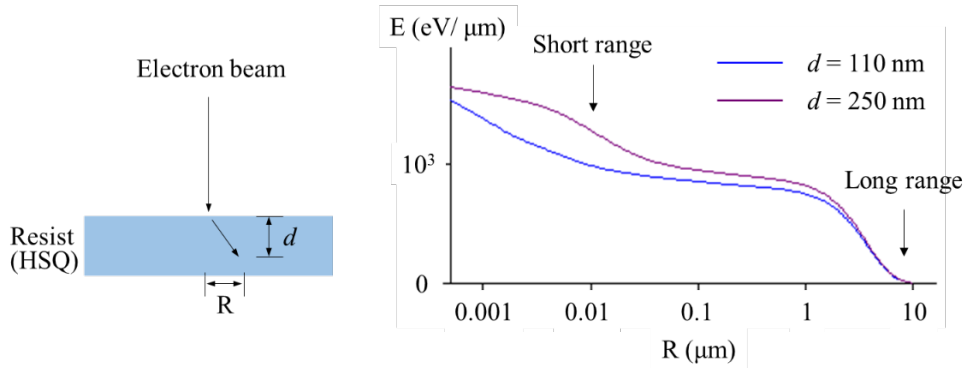
Figure 3.14 Typical point spread function of HSQ resist.

Figure 3.14 is an example of electron energy distribution. R represents the distance from beam spot, d is depth from resist surface. Blue curve and purple curve show the energy distribution at depth of 110 nm and 250 nm, respectively. The short range is around 0.01 μm, corresponding to effects of forward scattering. Long range is around 10 μm, which is caused by backward scattering of substrate. Comparing the two curves, we can see that forward scattering effect is more significant at deeper position. This is why thin resist often has higher resolution than thicker one. The thickness of HSQ in our

experiment is around 150 nm (detected by Dektak).

In a two-dimension plane, deposited energy after exposed by a given pattern is written as a sum of the PSF function of each pixel.

$$E(r) = \sum_{r_0} f(|r - r_0|)D(r_0) \qquad (3\text{-}3)$$

Where $D(r_0)$ is input dose as a function of position, f is point spread function, $E(r)$ is deposited energy as a function of position, r represents the position of point (x,y). As long as we know f and desired deposited distribution E(r), we can inversely optimize the design of $D(r_0)$. This is called proximity effect correction.

There are three methods to do it: (1) Dose modification [57] [58] [59]. To determine dose for each pixel instead of using uniform dose for whole pattern. (2) Shape modification [57] [60]. In this method, a single dose is used for entire pattern, but the pattern is modified in such a way that the developed pattern will be as close to designed pattern as possible. (3) Background exposure correction [61]. By writing an inverse of the designed pattern again to bring background dose to a uniform level. In this research, We used dose modification method. We firstly calculate the point spread function by commercial soft TRACER [62], and then do the correction of designs by BEAMER [62].
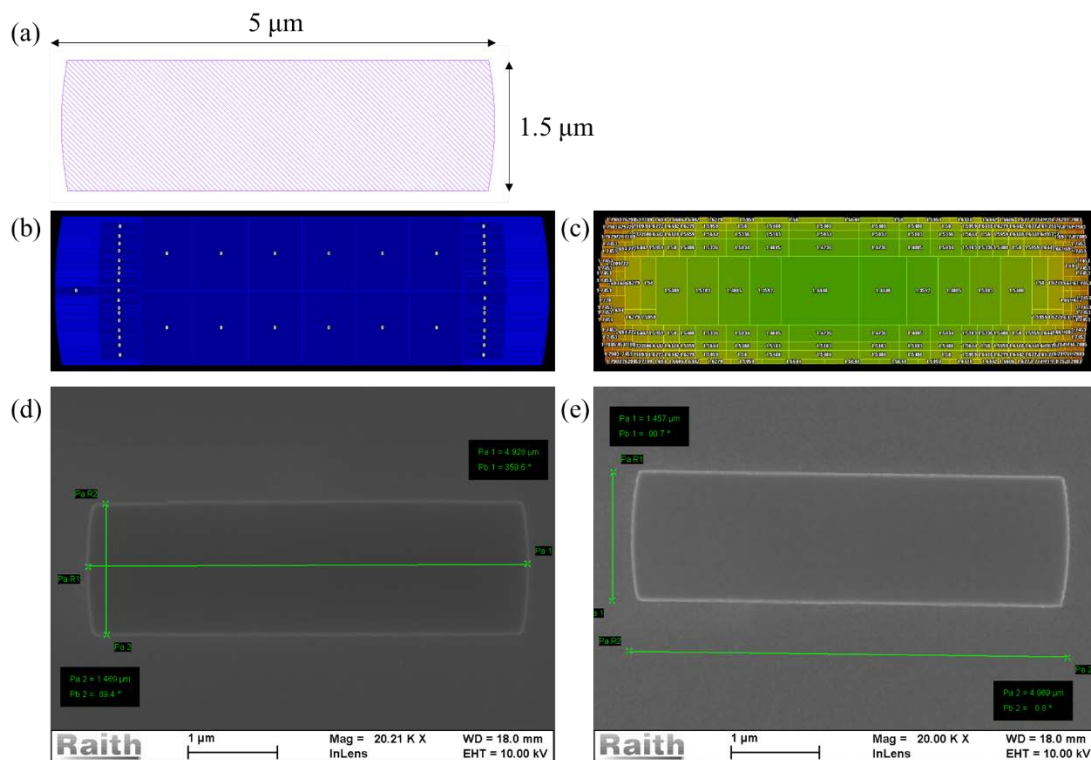
Figure 3.15 (a) A designed pattern with 5 μm in length and 1.5 μm in width. (b) Uniform input of dose without correction. (c) Input of dose after proximity effect correction. Green area represents

higher dose and orange area represents lower dose. (d) Developed pattern without correction. (e) Developed pattern with proximity effect correction.

Figure 3.15 is a comparison with and without dose modification. Figure 3.15(a) is a designed pattern with 5 μm in length and 1.5 μm in width. Figure 3.15(b) shows uniform input of dose without correction. Each area will be exposed by same energy. (c) Input of dose after proximity effect correction. Each area will be exposed by $a \times 1800\ \mu C/cm^2$, the factor a varies from 1.4448 in center green area to 1.7983 at orange edge. The value of 1800 is determined by experiment. Figure 3.15(d) is developed pattern without correction and Figure 3.15(e) with proximity effect correction. No matter what value of dose we choose, the developed pattern is always distorted. The long side is not straight because of over expose due to long-range backward scattering effect. After dose modification, the developed pattern is almost the same as designed image.

● **Uniformity of HSQ EBL**
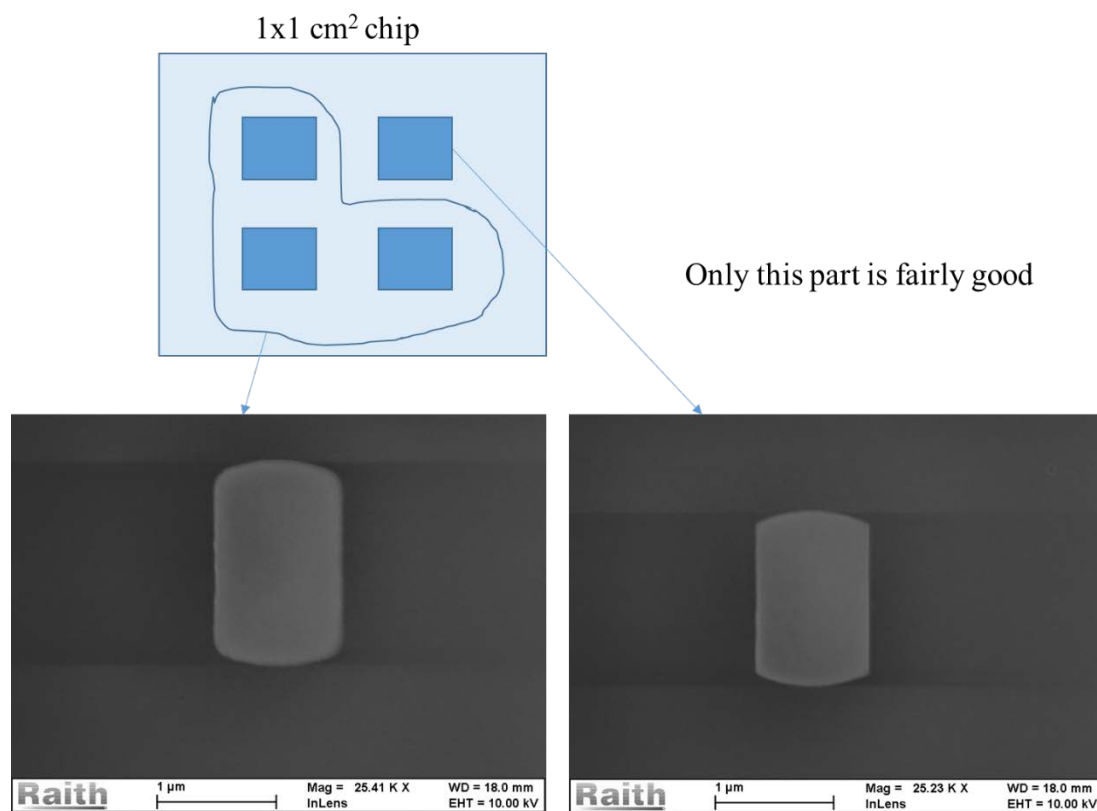
Figure 3.16 Uniformity of HSQ performance on the chip.

A problem is that HSQ is quite sensitive to process condition. An example during

condition developing is shown in Figure 3.16. On the 1×1 cm^2 chip, after lithography, develop results differed from area to area. We see correctly patterned resist and round-cornered resist on chip simultaneously. We checked the resist thickness by Dektak, found that the thickness varied from 150 nm to 250 nm at different positions. Further comparison experiment showed that how many drips used in spin coating is very important. Too much resist dripped onto the chip may cause difficulties in resist spreading. One should always confirm process condition before using real samples.

3.2.3 Dry etching

Dry etching of InP is a key processing in fabricating photonic devices. Unlike electronics, light is sensitive to geometry imperfects during fabrication. For example, extra scattering will occur if there is a particle near waveguide. We mentioned how to obtain smooth hard mask in previous section. This section is about another important step to obtain smooth sidewall of mesa.

Dry etching of InP is basically classified into Cl$_2$-based and CH$_4$ based [63]. We used CH$_4$ based gas during this work because it results in better sidewall roughness [64]. During the dry etching, only part of radicals from CH$_4$/H$_2$ react with InP, redundant gas will react with each other and form polymers [65]. The polymers stick to sidewalls and protect them from bombard of ions. However, extra polymers will result in sloped sidewalls after dry etching, which is not good for laser cavity. O$_2$ plasma ashing can wash undesired polymers away. A practical recipe to etch InP is cycles of CH$_4$/H$_2$ etching and O$_2$ ashing to get good verticality [49].

Anisotropy of the etching is mainly due to ion bombardment effects. In addition to period ratio of CH$_4$/H$_2$ etching to O$_2$ ashing, pressure, power (accelerate voltage for ions), and fraction of gases. Radicals hit InP along vertical direction, react with surface materials. Sidewalls are only exposed to the scattered ions in gas phase or reflected ions from nearby surfaces. Thus, decreasing pressure can reduce scattering in gas phase, decrease the lateral etch rate. However, ion concentration is low at low pressure, leading to low etch rate in vertical direction. We used inductively coupled plasma (ICP) etching to

improve aspect ratio of dry etching. It is a widely used technology. By applying strong time-varying (radio frequency) magnetic field to the gas exposed in electrical field, molecules are ionized much more efficiently than conventional way of which only electrical is used. Therefore, ICP technology can generate high-density ions at low pressure, offering improved profile control of sidewall. Secondly, average dynamic energy of ions depends on accelerate voltage. The higher it is, the higher vertical etch rate is. At the same time, mask degrades faster, and substrate will be left with more damaged surface. It is a trade-off between several factors, and should be determined by experiment. Lastly, decreasing fraction of CH4 generally enhance sidewall verticality, but lower etch rate. It is complicated since they are not linearly related [65].

Simple summary here. One should change the established InP etching recipe following priorities below: (1) Power. (2) Period ratio of CH_4/H_2 etching to O_2 ashing. (3) Pressure. (4) Gas fraction. Noting that gas fraction is last parameter to change because unexpected second-order effects may come out.

3.2.4   Metal deposition

We chose silver as metal coating material because it shows best performance among common metals (see details in 4.2.2). Silver is active metal, highly reactive with oxygen or H_2O. During vacuum evaporation, residue gas in the chamber is mainly H_2O [66] and oxygen. They will contaminate the surface of deposited silver, causing boundary inside silver film. Such boundary is reason of scattering, which is not good for optical device. We have several guidelines to deposit silver film.

Firstly, one should make the vacuum as high as possible to avoid contamination to the silver film [45]. It is good to bake chamber for long time (over 12 hours) to improve vacuum. Make sure cool down the chamber and sample to room temperature before deposition. Since sample is fixed inside chamber, it may take several hours to cool down. Silver film will be porous and rough if temperature is near 100 centigrade [67].

Secondly, make deposition rate fast [45] So that the silver atom will be covered by other silver atoms before attacked by residue gas atom.

Thirdly, rapid time annealing help increase grain size of silver film in my comparison experiment (Figure 3.17). We can see grain size of silver became larger after annealing. Note that this is only test during process developing. My final device is coated by vacuum evaporation. Thickness of film is important as well. Holes may form in thin film with long time annealing (Figure 3.18). We deposited 1.0 μm thick silver in final device.
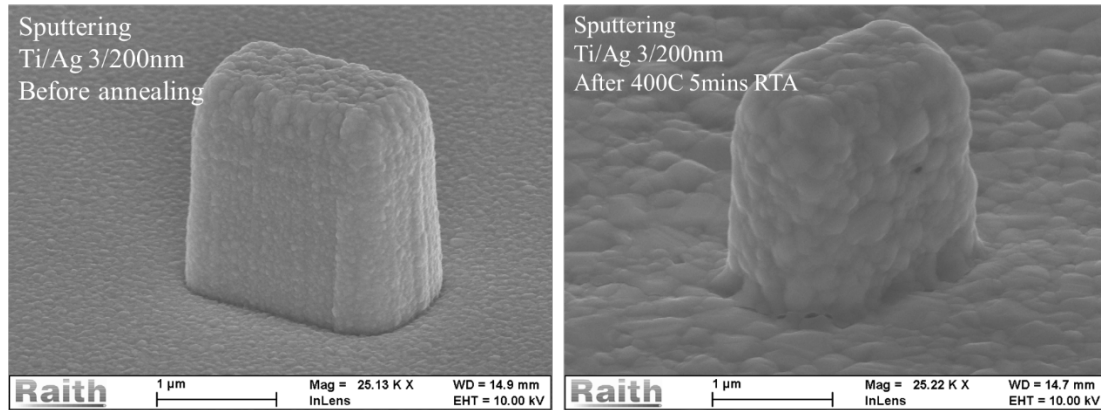
Figure 3.17 Scanning electron microscope images of silver films deposited by sputtering before and after annealing.
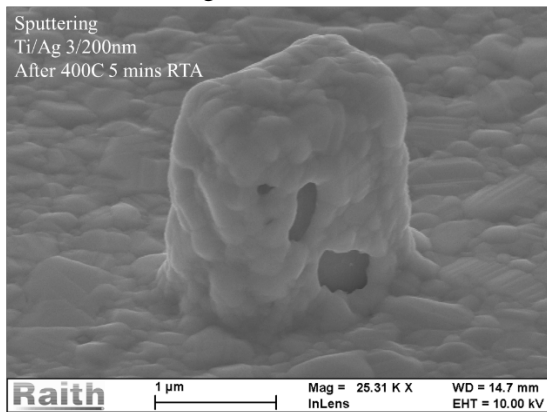
Figure 3.18 Holes formed after annealing.

3.2.5 Surface treatment

Plasma dry etching can result in damage and contamination in devices [68] [69]. Residues remain on the surface of devices may cause oxidization or unexpected resistance. Ion bombardment can result in bonding changes and impurities implantation. The effects can go as deep as several hundred nanometers in depth direction, creating trap states in the materials and modifying carrier lifetime. The sidewall of mesa will be damaged by scattered ions although it is not exposed to vertically accelerated ions. For diode emitters,

non-radiation recombination efficiency will increase as a result. In this research, the surface-to-volume ratio of wavelength-scale cavity is large so such effects are fatal to its operation. It is necessary to remove damaged surface after dry etching.

We use O_2 plasma to oxidize InP surface at vertical walls of mesa, $H_3PO_4:H_2O$ (1:10) to remove InP and its oxides, $H_2SO_4:H_2O_2:H_2O$ (1:8:5000) to slightly remove InGaAs. Latest report suggests that SiO_2 passivation also help improve the emission efficiency after wet chemical treatment [25].

Chapter 4 Light-injection wavelength-scale metal-coating laser

4.1 Introduction

In this chapter, we will firstly introduce the design of capsule-shaped cavity. Then, comparison of simulation result of capsule-shaped cavity and rectangular cavity shows that Q factor of TE mode is enhanced by this design. A previous work in our group is also presented. Clear improvement was confirmed [33]. Basing on that work, I reviewed other factors in cavity design, such as effect of metal and insulator to device's performance as well. Improvement of fabrication process is detailed in Chapter 3 . After that, I fabricated several cavities with different dimensions and tested them at room temperature by optical pumping. Lastly, measured data of fabricated devices shows that slope efficiency of capsule-shaped cavity is higher than that of rectangular one, which is in good agreement with simulation result.

4.2 Device design
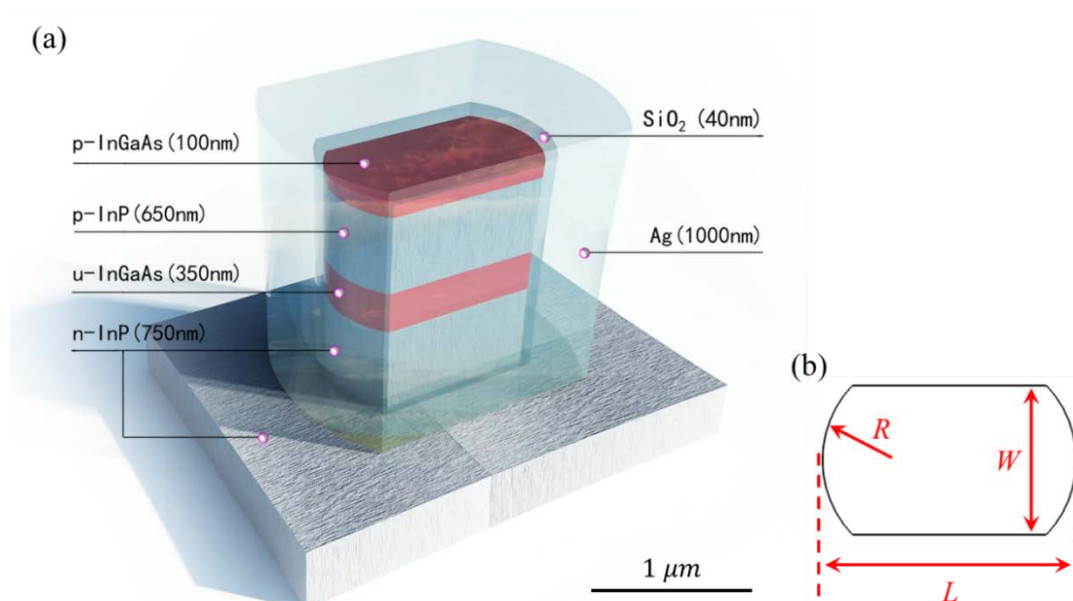
Figure 4.1 Design of capsule-shaped cavity. (a) Perspective view of cavity. (b) Schematic diagram of top view. Black outline represent InP semiconductor, not including insulator and silver.

Figure 4.1 shows the structure of the fabricated device. The epitaxial layer consists of, from bottom to top, 750 nm n-InP lower cladding layer, 350 nm un-doped InGaAs active layer, 650 nm p-InP upper cladding layer, and 100 nm p-InGaAs contact layer, which is included for future development towards electrical pumping. The mesa is capped with a thin (40 nm) SiO2 insulating layer, followed by a thick (1000 nm) silver layer. As shown in Figure 4.1(b), cylindrical facets with a radius of curvature R are introduced at both ends of the mesa to constrict the mode inside the center of the mesa [32] [33].

4.2.1 Advantage of capsule-shaped cavity and previous work in our group
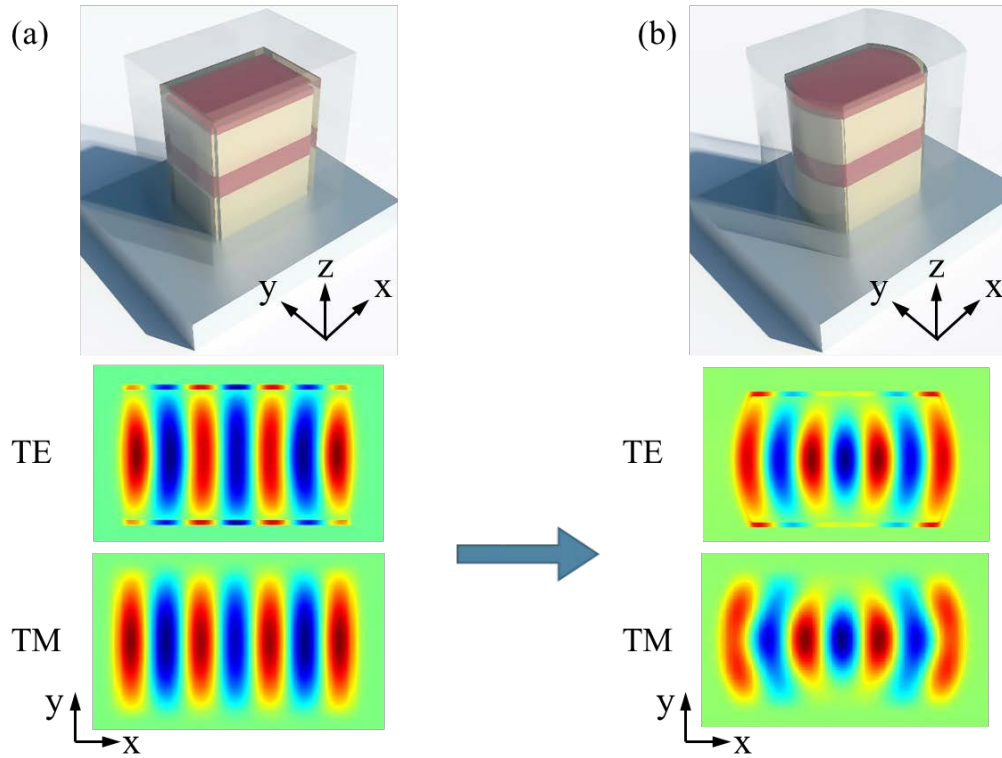
Figure 4.2 Electrical field intensity distribution in (a) rectangular cavity, (b) capsule-shaped cavity.

To confirm the effect of the capsule shape in enhancing mode selectivity, we numerically investigate the Q factor of the cavity by 3-dimension fully vectorial finite-difference time-domain simulation. Refractive indices of InP, InGaAs, and SiO2 are assumed to be 3.17, 3.53, and 1.45, respectively [16 ~ 18], while Drude-Lorentzian fit is employed to model the silver layer. The complex dielectric constant of silver is -86.6-8.7i

at 1550-nm wavelength, which is in good agreement with experimental data [19]. Using the symmetry of the structure, we simulate only quarter region of the structure and set proper conditions (perfect either electric or magnetic condition) at each boundary to selectively excite either TE or TM mode.

Figure 4.2 shows calculated electrical field intensity distribution in rectangular cavity and capsule-shaped cavity. Both have a length of 1.6 μm and a width of 1.0 μm, and L/R is 1.25 for capsule-shaped cavity. In Figure 4.2(a), the effective width of resonating mode is uniform along longitude direction. While in Figure 4.2(b), we can confirm that the field inside the capsule-shaped cavity is constricted at the center with reduced overlap with the metal cladding, which is especially significant for the TE mode. Phase surface of the resonating mode becomes curved, looks like a Gaussian beam. As a result, metal induced loss decreases and Q factor increases.
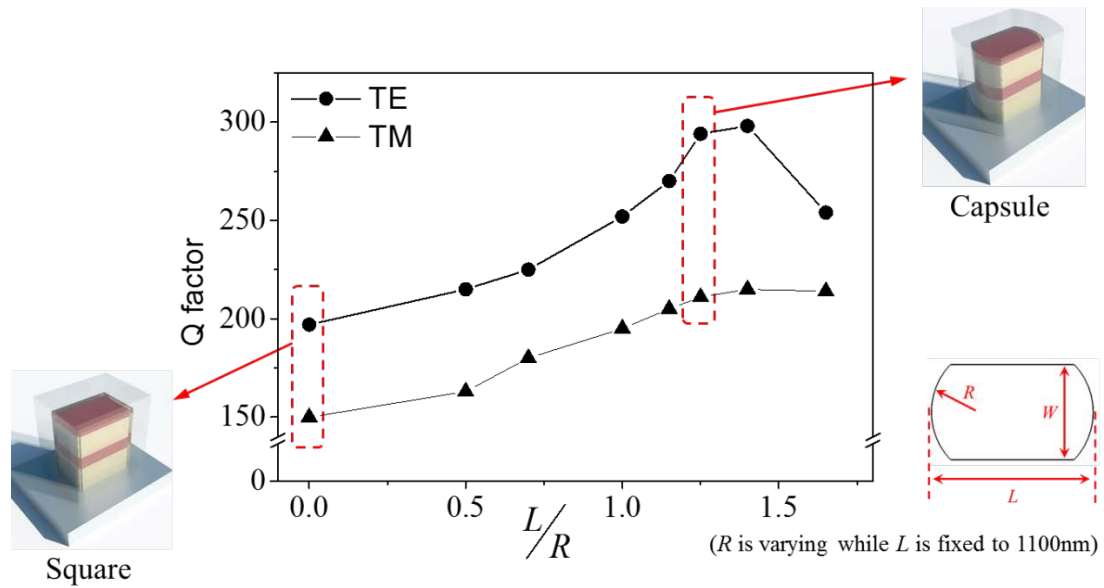
Figure 4.3 Improvement of curved mirror. Q factor changes as a function of radius of curved mirror.

Figure 4.3 shows the improvement of curved mirror from previous work [32]. During this calculation, cavity width is fixed to 840 nm, cavity length is fixed to 1100 nm. Q factors are calculated while radius of curved mirror varies from $L/R = 0$ to $L/R = 1.6$. $L/R = 0$ means R is infinite, a straight line. It is clear that Q factor gets higher with a curved mirror, and reach maximum when $L/R = 1.25$. This suggests that

the R satisfying $L/R = 1.25$ fits the phased surface most well in this case.
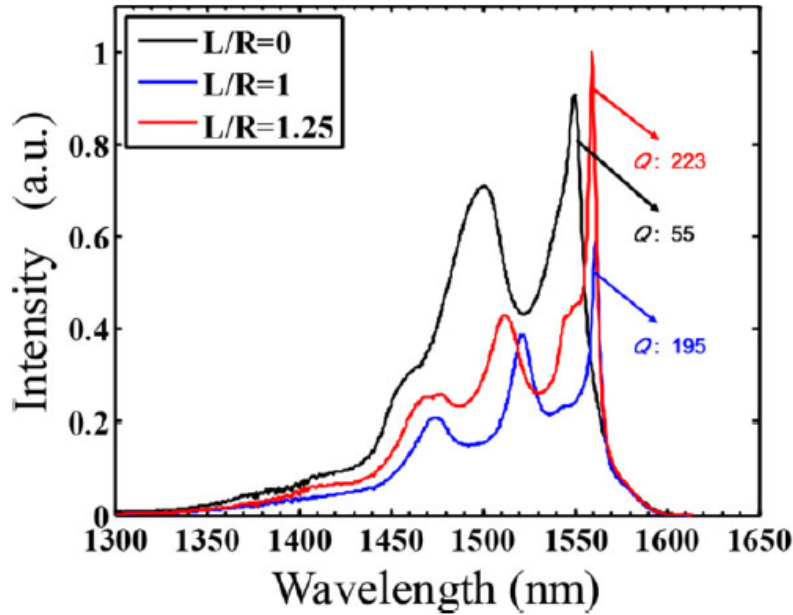
Figure 4.4 Previous work, measured spectra of fabricated metal-clad cavity with the same width and length but different cylindrical mirrors [33].

Figure 4.4 shows previous experiment results. Measured emission spectra from three different cavities are depicted in the same plot. All the cavities are 1.84 μm long and 0.8 μm wide. Radius of cylindrical mirrors are different and the ratio of length to radius is written in the plot. From the peak near 1560 nm we extract Q factors (= peak wavelength / half-width) for each cavity. We can see that as the ratio of length to radius increases from 0 to 1.25, Q factors increases significantly in consistence of prediction of simulation. The idea of new design is effective. Its' enhancement of Q factor is very important to nano-cavity of on-chip light source, whose quality factor is usually at order of a few hundreds. I further optimized of cavity design and fabrication process at first step of this research.

4.2.2   Choice of metal

Widely used plasmonic metals are silver, gold, copper and aluminum. Ag is perhaps the most widely used because of its low losses. Au is perhaps second most used metal, particularly in red and infrared wavelength [70]. Although loss of Au is not as low as Ag,

Au is more stable than Ag, which could be easily oxidized by O_2 in air, causing high resistance in electrical circuit. Cu is an abundantly used plasmonic metal due to its low cost. Al is a good candidate as well, has moderate performance at infrared wavelength and most good performance at ultraviolet wavelength. An optical pumping nanolaser coated by Al was reported achieve lasing at room temperature [71]. Unfortunately, Cu and Al are very reactive and form oxides easily, which is a problem in real application.
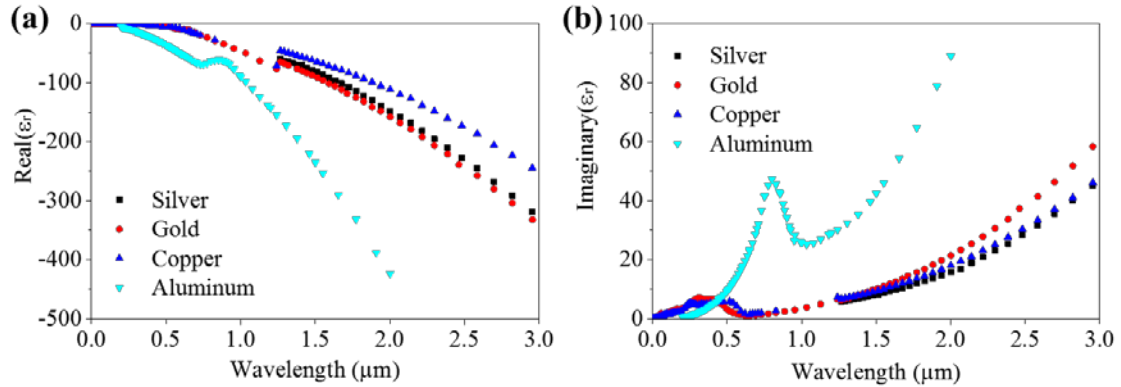
Figure 4.5 (a) Real part and (b) imaginary part of permittivity of silver, gold, copper and aluminum.

Figure 4.5 is real part and imaginary part of permittivity of the metals mentioned above measured by Palik [72]. We used his data to run simulation in this thesis. By the way, these values are derived from experiment, differ slightly from different reports. The values may also varies by deposition process. Requirement for metal used here is a large negative real part and a small imaginary part of permittivity at 1550 nm. The larger real part of permittivity is, the smaller proportion of energy distribution in metal is. In another word, penetration depth is smaller if real part of permittivity is larger. The imaginary part of permittivity leads to absorption loss. The smaller it is, the smaller loss will be.

We investigate the cavity performance with silver, gold, copper and aluminum, respectively. Results are summarized in Table 4-1. It is clear that cavity coated by silver has best Q factor. Although silver is reactive than gold, making it difficult to get high quality silver film by deposition, it is experimentally reported that loss of silver is smaller than gold if one deposit it with carefully designed recipe [45]. We chose silver to enwrap cavity in my experiment. A problem is that dewetting occurs between SiO_2 and silver. Silver tends to form small islands instead of spreading uniformly on the SiO_2 surface due

to minimization of surface energy. Therefore, silver film easily falls off after coated to SiO$_2$. A 2 nm thick germanium (Ge) wetting layer sandwiched between SiO$_2$ and silver can significantly increase the adhesion [73], making silver coating stable.

Table 4-1 Q factor of cavities with the same size but covered by different metals. Size of cavity is $L = 1.6$ µm, $W = 1$ µm, $L/R = 1.25$

	Silver	Gold	Copper	Aluminum
Q factor	421	391	276	361

4.2.3   Discussion of insulator

● Alleviating absorption loss of guided mode
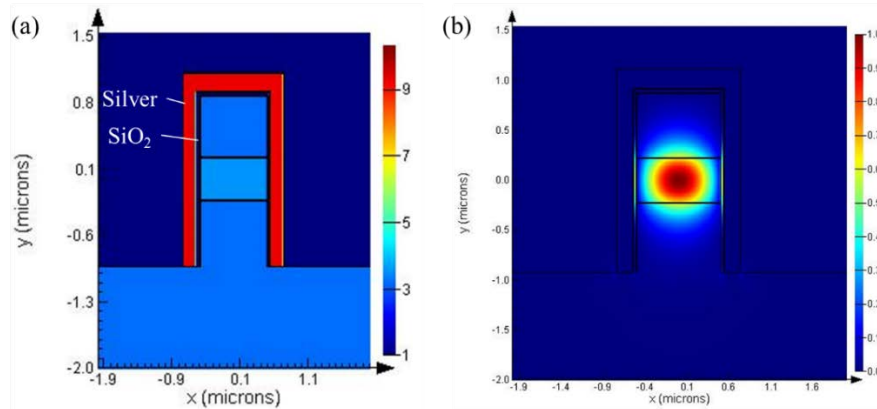
Figure 4.6 (a) Cross section of cavity with SiO$_2$ passivation in lateral plane. Width of waveguide is 1.0 µm. Thickness of SiO$_2$ is 40 nm.(b) Electrical distribution of guided mode in lateral plane. numerically calculated propagation loss is 45 dB/cm
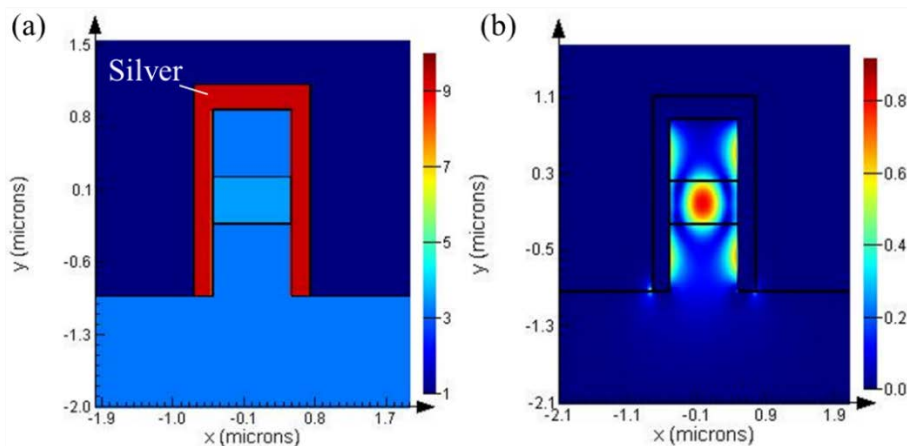
Figure 4.7 (a) Cross section of cavity without SiO$_2$ passivation in lateral plane. Width of waveguide is 1.0 µm. (b) Electrical distribution of guided mode in lateral plane. numerically calculated propagation loss is 4321 dB/cm

A SiO$_2$ buffer layer inserted between InP/InGaAs/InP waveguide and silver coating can reduce propagation loss significantly. As mentioned in section 2.2.1, evanescent field of guided mode can be expressed as $E_y = E_s exp[-\gamma_s x]$, where $\gamma_s = k_0\sqrt{n_1^2 sin^2\theta - n_2^2}$, x is distance from boundary of waveguide. When there is not SiO$_2$ passivation, evanescent field contact to silver directly and get absorbed (Figure 4.7,). If passivated by 100 nm thick SiO$_2$, $n_{eff} = n_1 sin\theta \cong 3.4$, $n_2 = 1$, $k_0 = 2\pi/(1.55\,\mu m)$, $\gamma_s = 3.35k_0$, the electrical field overlaps with silver (absorbed energy) will be reduced by a factor of $exp[-2\gamma_s x] = 0.07$ (coefficient 2 represents square of electrical field). This is approximate calculation for 1-dimension case. Usually 2-dimension waveguide has stronger confinement. The reduction of loss will be more significant.

● Effect of insulator thickness to quality factor
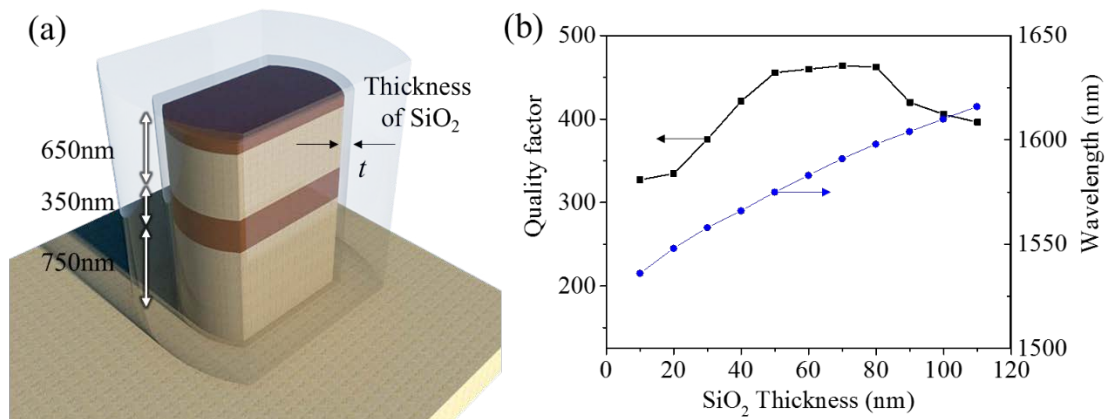
Figure 4.8 (a) Schematic image. (b) Quality factor and resonating wavelength as a function of thickness of SiO$_2$.

Next, we studied the effects of SiO$_2$ insulator thickness on cavity performance. Again, we fixed the size of cavity to $L = 1.6\,\mu m$, $W = 1\,\mu m$, $L/R = 1.25$. Coated metal was set to be silver. Only TE mode was considered in simulation.

Thickness of SiO$_2$ is another factor that affects device's performance remarkably. In Figure 4.8, we can see quality factor is sensitive to the SiO$_2$ thickness. Refractive index of SiO$_2$ is 1.45, far below 3.53 of InGaAs. Along longitude direction, the interface of SiO$_2$ and InGaAs in front of silver mirror reflects light at some degree, decreasing metal absorption. On the other hand, thick SiO$_2$ causes extra scattering, which increases the loss of the cavity. A trade-off point of the thickness between these two effects is around 70 nm,

where quality factor reaches maximum of 463.

Thicker SiO_2 results in longer effective cavity length as well. The resonating wavelength increases linearly in order to match longitude resonating phase condition. The shift of resonating wavelength may have negative relation to obtainable material gain, which is critical for small laser. The resonating wavelength varies over 10 nm if error of coated SiO_2 film thickness is over 10 nm, which likely happens in fabrication. In addition, thick SiO_2 may cause heating problem as well because of its' low thermal conductivity [74]. It is wise to choose thin SiO_2 film during design.
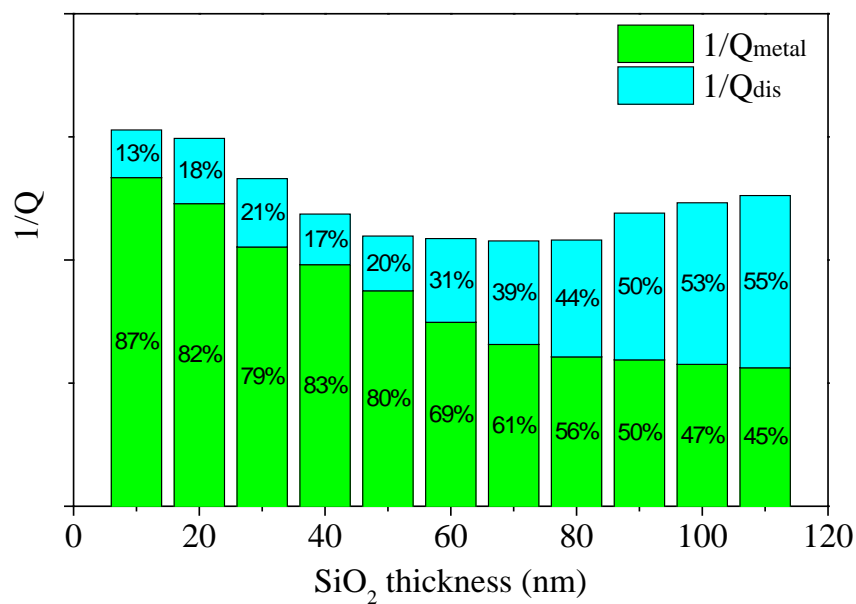
Figure 4.9 Fraction of $1/Q_{metal}$ and $1/Q_{dis}$, corresponding to metal absorption and radiation loss respectively, as a function of SiO_2 thickness.

The quality factor can be written as $1/Q = 1/Q_{metal} + 1/Q_{dis}$, where $1/Q_{metal}$ and $1/Q_{dis}$ relate to metal-induced loss and radiation loss, respectively (see coupling efficiency in section 5.2.1). In Figure 4.9, we show the fraction of $1/Q_{metal}$(corresponding to metal absorption loss) and $1/Q_{dis}$(corresponding to radiation loss) as a function of SiO_2 thickness. The height of column relates to power dissipation rate. The higher, the more lossy. We can see clearly the loss is almost induced by metal when SiO_2 is very thin. SiO_2 film works like a half mirror and its reflectivity increases at the range we studied. Therefore, both absolute value and fraction of metal (green part of column) induced loss go down. On the other hand, inside the SiO_2 film, there is no refractive index difference in

vertical direction, meaning that no confinement in vertical direction. Guided mode escape to the bottom. Therefore, we see radiation loss (cyan part of column) goes up as film thickness becomes larger.

4.2.4 Bow-tie cavity
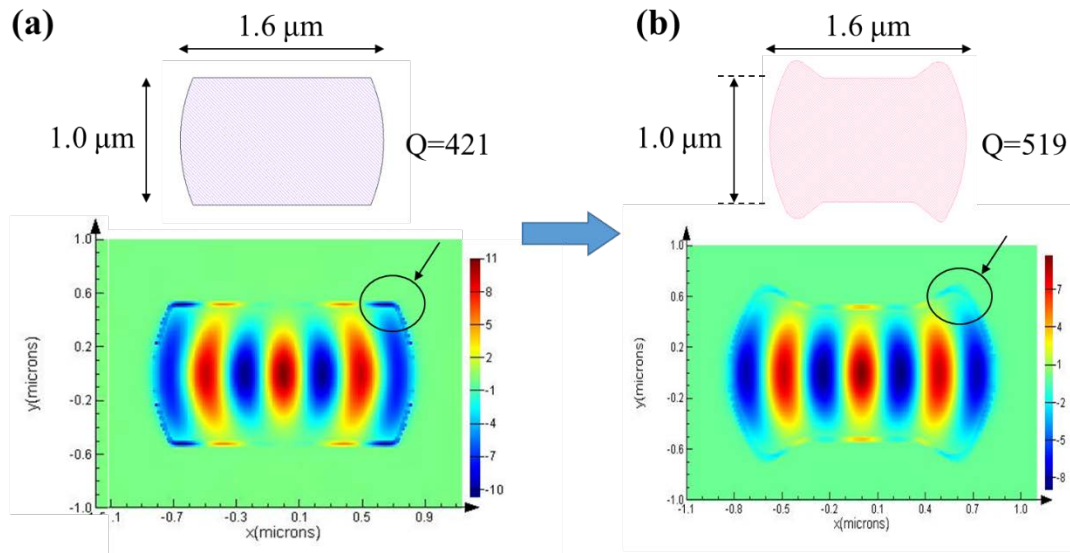
Figure 4.10 (a) Capsule-shaped cavity and its resonating mode. (b) Bow-tie cavity and its resonating mode. Only TE mode is considered here.

We tried further improving design of cavity. Figure 4.10 shows another idea. As mentioned before, capsule-shaped shrink the mode at center. However, it does not work to the electrical field at the corner of the cavity. The anti-node of the wave expands to hit the metal coatings. That causes extra loss. We expand the corner of the cavity, making it look like a bow tie shown Figure 4.10(b). The electrical field that extended to SiO_2 film now is included inside cavity. Quality factor improves from 421 to 519, which is the evidence that our considering matches the physics. However, it is difficult to optimize the structure to maximize quality factor judging eyes. An inverse design method will be a good choice [75] [76] to design irregular geometry device. An optimized structure will be generated by repeated computation for desired function including physical constraint.

By the way, in trial fabrication we found that a narrow horn of the cavity easily degraded in fabrication process. The exposed sidewalls of horn during dry etching process are etched back. It is important to set a minimum geometric feature size of edges during

cavity designing.

4.3   Measurement setup
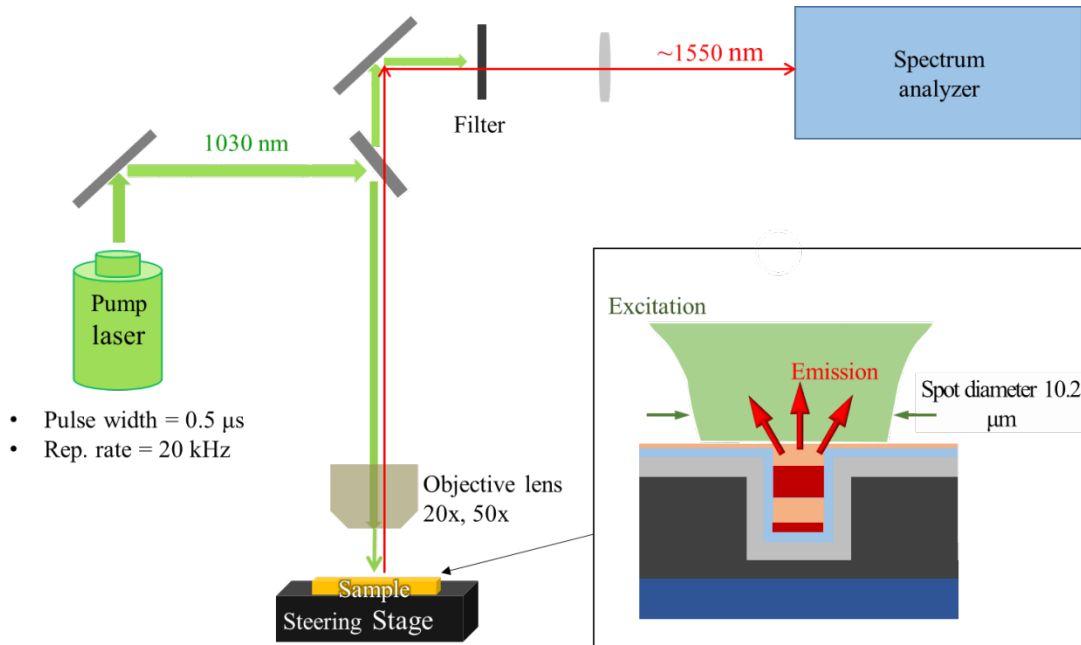
Figure 4.11 Schematic diagram of measurement setup. Inset is a microscope view of sample, showing excitation light hits cavity and emissions from cavity.

The fabricated devices were tested at room temperature under pulsed optical pumping. A 1030 nm pulsed laser was used to pump the cavity, where a pulse width of 0.5 µs and duty cycle of 1% were used. The beam focused onto a cavity through an objective lens. The diameter of focused beam spot is measured to be 10.2 µm. The emitted light from the cavity was collected through the same objective lens, and redirected to a spectrometer with a cooled (-100°C) InGaAs photodetector array. A part of collected light reflects by half mirror and travels to CCD camera, from which we can have sight of sample surface. Sample is located on a copper plate stuck to a temperature controller. This is to keep sample temperature not change while hit by injecting laser. The whole stage is controlled by stepper motor, could move at a step resolution of 0.1 µm at x, y and z direction. We fix the injecting laser spot, adjust the position of sample to make interested cavities exposed to pumping laser. After fine adjustment, we record the data when received signal reach its' maximum.

4.4 Result

4.4.1 Lasing from a capsule-shaped cavity

Figure 4.12 (a) Electrical field distribution of each simulated mode. (b) Simulated resonating spectrum of a capsule-shaped cavity, whose length is 1.6 µm and width is 1.0 µm. Blue scatter is normalized measured photoluminescence of active material. (c) Measured emission spectrum of a fabricated capsule-shaped cavity under different optical pumping power.

We fabricated many capsule-shaped cavities with different dimensions and tested them by optical pumping. A cavity with $L = 1.6$ µm and $W = 1.0$ µm started lasing, whose spectrum is shown in Figure 4.12(c). We also calculated the characteristic of the cavity, the simulated spectrum is shown in Figure 4.12(b). We put two light sources, TE polarized source and TM polarized source, inside cavity before simulation to confirm all the modes that exist. We can see there are 4 peaks in the curve. Figure 4.12(a) shows the electrical field distribution of the wavelength at each peak. E_y and E_z components are plotted respectively. Only the mode at $\lambda_3 = 1568$ nm is TE polarized. Mode 2 and Mode 3 both propagate along longitude direction. Mode 1 oscillates along lateral direction with a single path length of 1.0 µm. Mode 4 is a high order mode.

The InGaAs active layer used here has wide photon luminescence range from 1400

nm to 1600 nm (Figure 3.1), reaching peak at 1570 nm. Comparing Figure 3.1 with Figure 4.12(c), we can see that at low pumping power (black curve), mode 1 and mode 4 are dominant because there are two clear peaks around there. Calculated wavelength of mode 4 is over 1600 nm, out of the material emission range. Error of size during fabrication, error of the thickness of SiO_2, both can affect the resonating wavelength of cavity. Thus, we attribute the measured peak near 1600 nm to the calculated mode 4. When pumping power increases (red curve), mode 2 begins to stand up. Mode 3 also shows up when come to green curve. The next, blue curve suggests that there is a serious mode competition between mode 2 and mode 3, the TE and TM polarization of a same longitude mode. Finally, TE mode wins, starts lasing. Its power is 10 dB stronger than that of others. The quality factor of mode 1 and mode 4 are almost as high as that of mode 3, but the material gain peaks around 1570 nm. Therefore, the measured lasing wavelength is 1535 nm. Although there is a wavelength shift between simulation and measured data, considering the error of cavity size and SiO_2 thickness, we think measured spectrum matches simulation well. <u>A problem is that resonating wavelength did not match the peak of material emission spectral profile, ~30 nm away from the peak</u>. Obtainable gain is 2/3 of the peak. There is room for improvement.

4.4.2 Lasing from a rectangular cavity

The measured and simulated spectrum of rectangular cavity with L = 1.6 µm and W = 1.0 µm are shown in Figure 4.13. Similar to the analysis of capsuled-shaped cavity, we put TE and TM polarized light source inside cavity at the same time, so the calculated spectrum (Figure 4.13(b)) should include all existing mode. There are four similar resonating modes as well, of slightly different wavelength. As we mentioned before, quality factors here are all lower than that of capsule-shaped cavity.
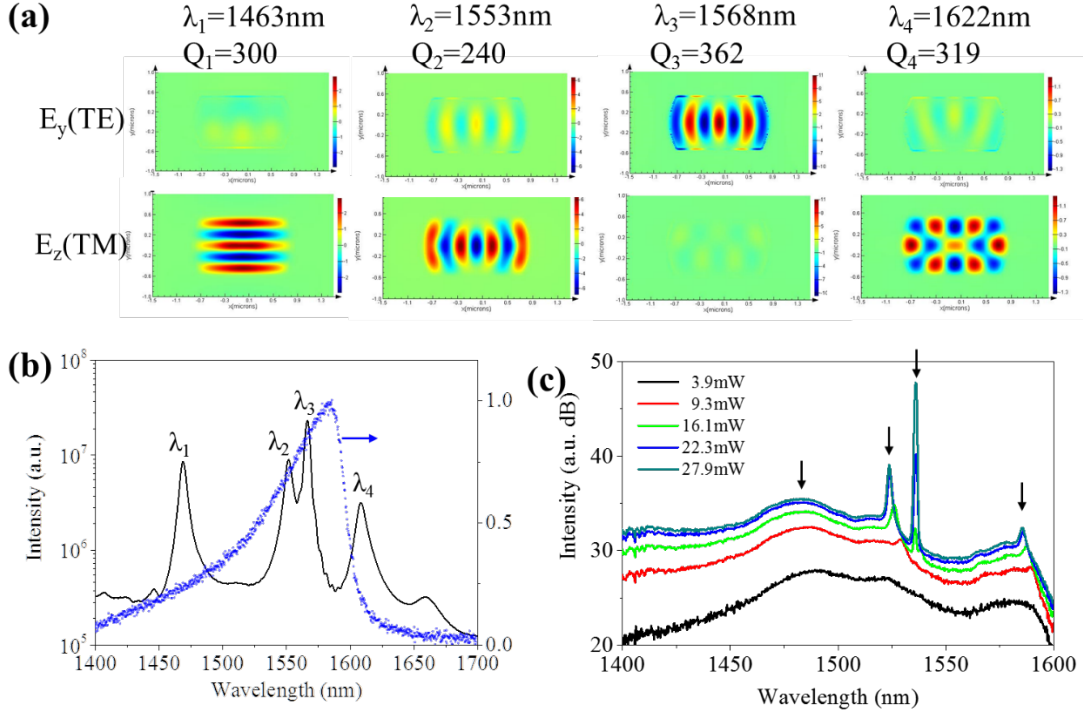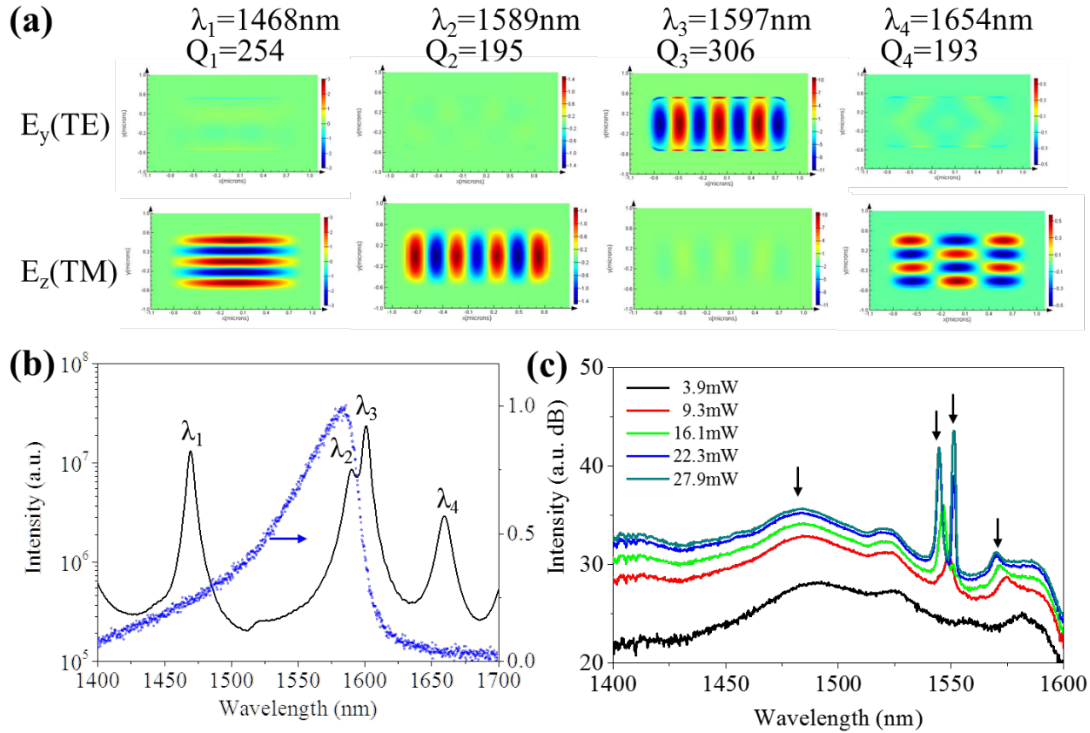
Figure 4.13 (a) Electrical field distribution of each simulated mode. (b) Simulated resonating spectrum of a rectangular cavity, whose length is 1.6 µm and width is 1.0 µm. Blue scatter is normalized measured photoluminescence of active material. (c) Measured emission spectrum of a fabricated rectangular cavity under different optical pumping power.

Measured spectrum matches simulation well. Four peaks are clearly seen in Figure 4.13(c). The mode competition is also similar. Mode 1 and mode 3 are powerful at low pumping level but soon mode 2 and mode 3 become dominant when pumping level goes up. Note that the power of mode 2 and mode 3 do not differ clearly, while the side-mode suppression ratio is 10 dB at the same pumping power for capsule-shape cavity.

4.4.3   Comparison of rectangular cavity and capsule-shaped cavity

Figure 4.14 shows the fabricated capsule-shaped and rectangular cavities mentioned above. Dimension of them are the same. They are also on the same chip, only 1.2 mm away from each other. We suppose they experienced the same condition of fabrication process, the difference of their performance is come from concept of design, not environmental factor.
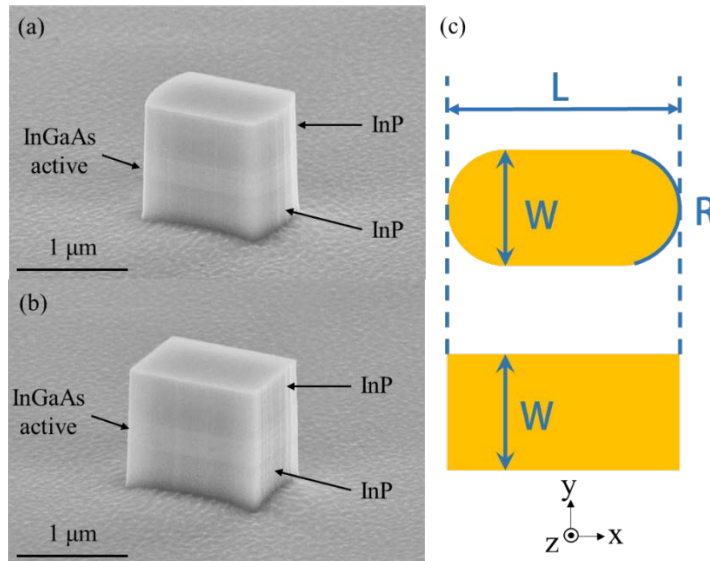
Figure 4.14 Scanning electron microscope image of fabricated devices before metal coating. (a) capsule-shaped cavity. (b) rectangular cavity. L=1.6 μm, W=1.0 μm, L/R=1.25.

Table 4-2 Calculated Q factor of two kinds of cavities

	Size		Simulated Q-factor	
	Width(μm)	Length(μm)	TM	TE
Rectangular	1	1.6	192	273
Capsule-shaped	1	1.6	192	349
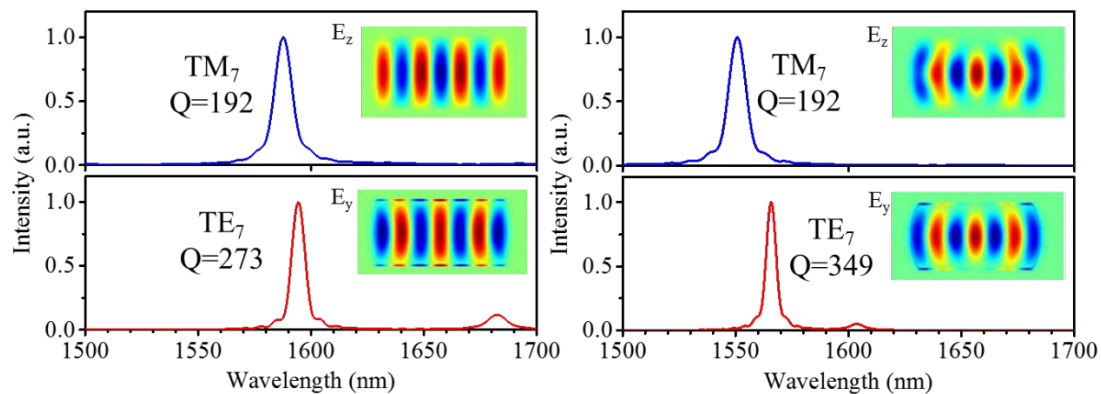
Figure 4.15 Simulated spectra of (a) capsule-shaped cavity and (b) rectangular cavity. The inset shows electric field distribution of the resonant mode.

We numerically compare them again more carefully. Using the symmetry of the structure, we simulate only quarter region of the structure and set proper boundary conditions (either perfect electric or magnetic condition) to selectively excite only TE or TM mode. Any second-order effects from undesired mode are removed. Calculated

spectrum are shown in Figure 4.15. Only one peak exists over a 200 nm wide wavelength range. The calculated Q factor are shown in Table 4-2. We can see that Q-factor of the TE mode increases from 273 to 349 (28% increase) by introducing the capsule shape, whereas that of the TM mode changes slightly from 192 to 192.

Figure 4.16(a) shows the emission spectra of a rectangular cavity with L = 1.6 µm and W = 1.0 µm, measured with increasing pumping power. The device has two clear lasing peaks at 1545 nm (Mode 2) and 1551 nm (Mode 1). By comparing with the numerical result presented in Figure 4.15, we assume that Mode 1 and Mode 2 correspond to TE and TM modes, respectively. Figure 4.16(b) shows the integrated spectral intensity of each mode as a function of pump power. We see clear evidence of mode competition between the two lasing modes, with the TE mode becoming the dominant mode at a pump power >25 mW. The linewidth of TE mode is also plotted in Figure 4.16(b) as an evidence of lasing. The measured linewidth at 27 mW is 0.3 nm, which was limited by the resolution of the spectrometer used in our measurement. From the pump beam diameter (10.2 µm), the footprint (1.6 µm^2) and active layer thickness (350 nm) of the measured device, and the absorption coefficient (17361 cm^{-1}) of InGaAs at 1030-nm wavelength [72], we estimate that the actual absorbed pump power inside the active layer is around 1% of the incident power. We thus estimate the actual pumping threshold to achieve lasing for the TE mode to be as small as 230 µW.
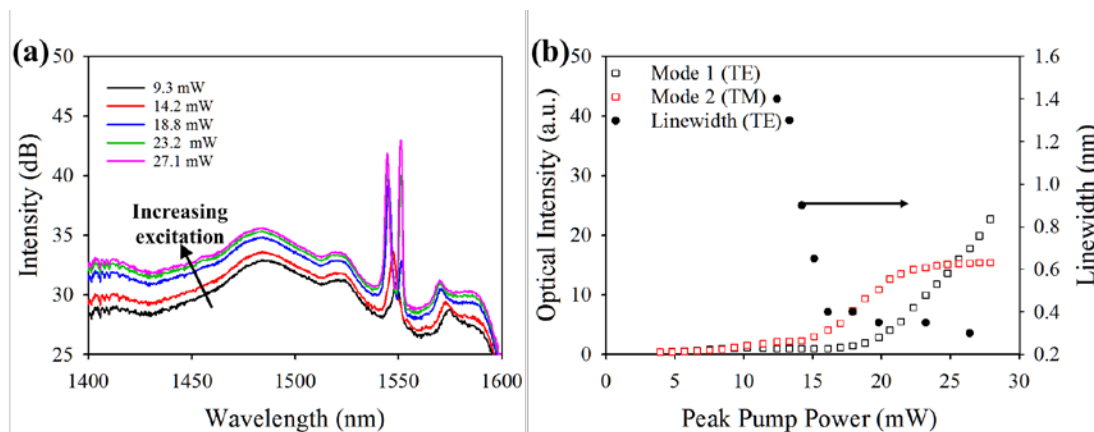
Figure 4.16 (a) Emission spectra of a rectangular laser (L = 1.6 µm, W = 1 µm) under increasing excitation pump power. (b) Emission intensity of the two lasing modes and TE mode's linewidth as a function of pump power. Effective pump power inside the active layer is estimated to be ~1% of the total pump power.

Figure 4.17(a) shows the emission spectra of a capsule-shape cavity with L = 1.6 µm, W = 1.0 µm, and L/R = 1.25. Similar to the rectangular cavity, two peaks (1535 nm and 1522 nm) are observed. However, longer-wavelength mode (Mode 1) quickly becomes the dominant lasing mode as we increase the pump power, with side-mode suppression ratio as large as ~10 dB at pump power of 27.9 mW. Figure 4.17(b) shows the integrated spectral intensity of each mode and the linewidth of TE mode as a function of excitation pump power. The TE mode start lasing beyond the threshold of 23.0 mW with the lasing linewidth of ~0.3 nm, which was limited by the resolution of the equipment as well. In comparison with the rectangular cavity (Figure 4.16), we observe that the mode competition is clearly suppressed and the slope efficiency of the TE mode is improved by factor of 1.95. Once again, we estimate the actual pumping threshold to achieve lasing in the TE mode as small as 230 µW.
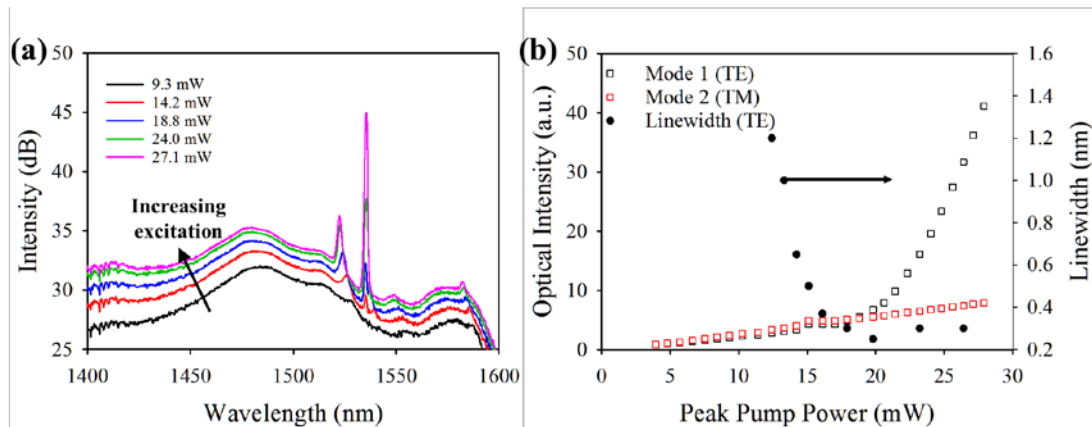
Figure 4.17 (a) Emission spectra of a capsule-shaped laser (*L* = 1.6 µm, *W* = 1 µm, *L/R* = 1.25) under increasing excitation pump power. (b) Emission intensity of the lasing modes and TE mode's linewidth as a function of pump power. Effective pump power inside the active layer is estimated to be ~1% of the total pump power.

4.4.4 Comparison of cavities with different sizes
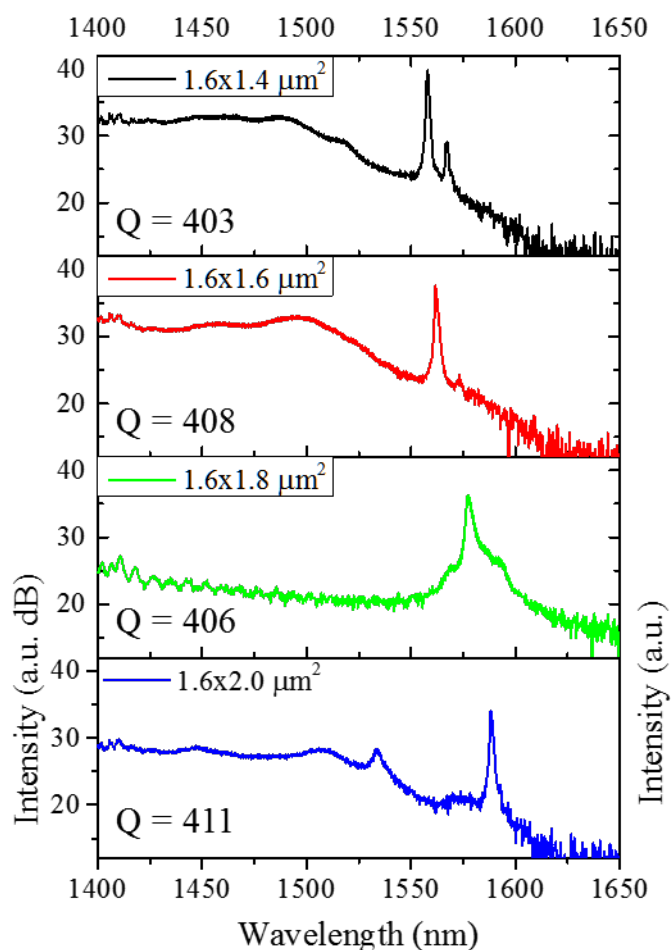
Figure 4.18 Measured spectrum from different cavities excited under the same optical power density. Peak pump power is 25.8 mW.

We also measured cavities with different dimensions, as shown in Figure 4.18, to see how cavity performance changes. The length of the cavities are all 1.6 µm. The width of them are different and denoted in the plot. The cavities discussed here are all on a chip different from that discussed in previous section. Unfortunately the 1.6 (length) × 1.0 (width) µm^2 cavity does not work on the chip discussed here, so we are unable to make a comparison to the results mentioned in previous section. However, I think the comparison of these for cavities makes sense and we get a general conclusion from it.

In the black or red curve, besides the main peak, we can see a small peak near it, which is probably a longitude mode in different polarization comparing to main peak. In

the green curve, due to the broadening of the peak, the closing two peaks seem emerged into each other.
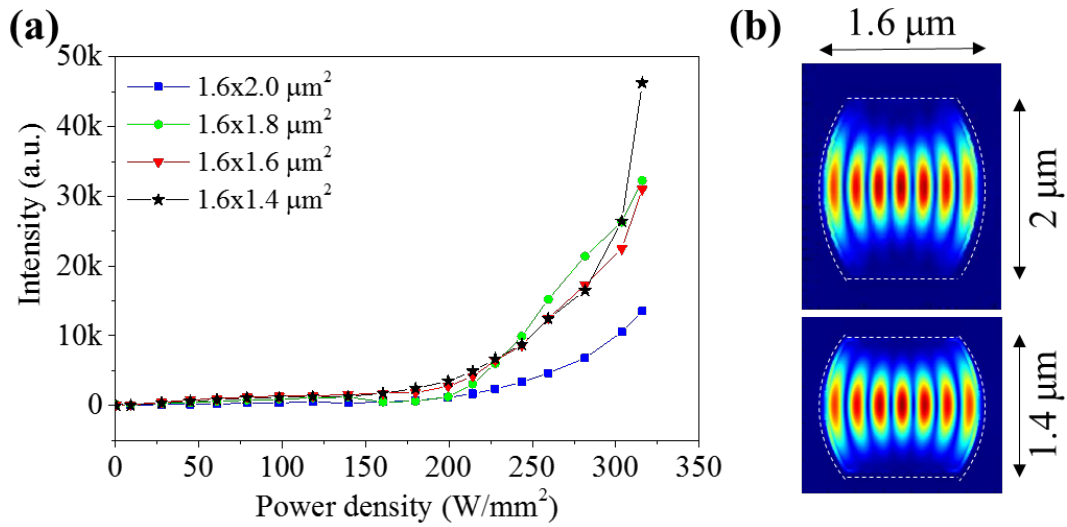
Figure 4.19 (a) Emission intensity as a function of pumping power density. Colored curves represents different cavities. (b) Electrical field distribution of resonating mode.
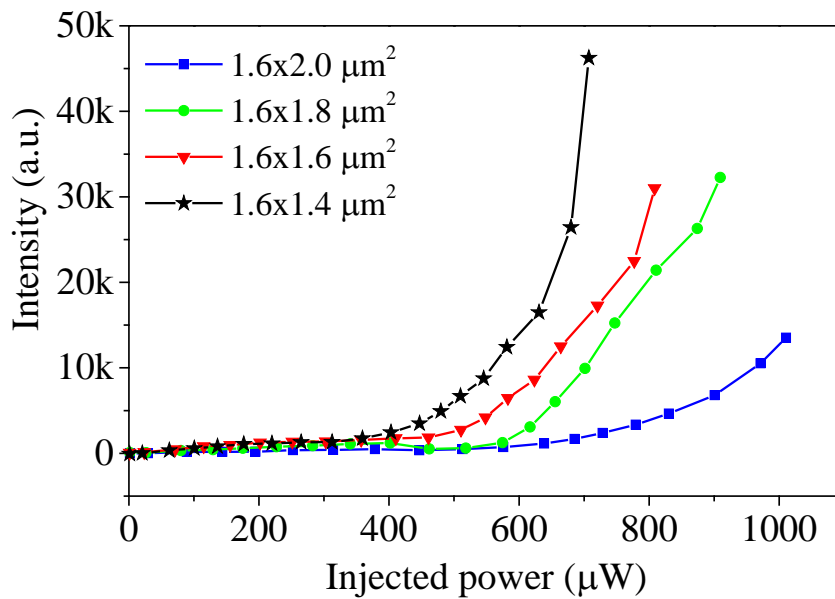
Figure 4.20 Emission intensity as a function of injected power. Colored curves represents different cavities.

Figure 4.19(a) shows the mode power (integral of spectrum) to pumping power density. I summed up the data of the wavelength range from $(\lambda_{peak} - 2)$ nm to $(\lambda_{peak} + 2)$ nm, where λ_{peak} is peak wavelength. A 4 nm wide range includes most

energy of an optical mode in cavity. The total energy of black, red, green curves are at same level, the energy of blue curve is a bit lower. Since the turning point of four curves are nearly the same, the trend and the turning point of the plot are reliable. We guess the misalignment of measurement setup caused the blue curve appeared lower.

The quality factor of these four cavities are 403, 408, 406, and 411, which are calculated by 3-D FDTD simulation, almost the same. Because longitude length and radius of curved mirror remain the same. We can see that the power density threshold of cavities are nearly the same, which are directly related to material gain. It is in consistent with simulation. The turning point of blue curve is equal to others, but its' intensity is a bit lower. It is likely due to measurement error. Figure 4.19(b) are mode distribution of $1.6 \times 2 \, \mu m^2$ and $1.6 \times 1.4 \, \mu m^2$ cavities. While dashed lines represent inner boundary of metals. The mode widths are different. For the largest cavity ($1.6 \times 2 \, \mu m^2$), spontaneous emission at lateral edge parts do not contribute to resonating mode, resulting in lower spontaneous factor.

It is clear in a power-in light-out plot (Figure 4.20). x axis is injected power, which is product of cavity area and power density. The smallest cavity has lowest threshold. It is an evidence that small cavity with high spontaneous emission factor and automatically has high efficiency. This also suggests that a cavity whose edge fits to optical mode perfectly would has optimized performance. Small light source has intrinsic advantages in photonic integrated circuit.

Chapter 5 Waveguide-coupled capsule-shaped cavity

5.1 Introduction

In previous chapter, we demonstrated wavelength-scale optical pumping laser cavity experimentally, observed laser radiated into free space from bottom of the cavity. My colleague Yu demonstrated electrical pumping metal-clad wavelength-scale laser [77]. Combining with above work, I would like to talk about waveguide-coupled wavelength-scale laser/LED in this chapter.

In practical application, we need to collect the light by fiber or waveguide to make use of it. However, radiation pattern of such small cavity is divergent. The light wave propagation is predicted by Fourier transform, which is called Fourier optics. According to that, small source leads to divergent radiation in far field. Figure 5.1 shows a far field pattern from a wavelength-scale cavity. Most of energy radiates at ±60 degree to the vertical direction. It is challenging to couple such light source into a fiber. In this chapter, we investigated the method of coupling the laser out with an integrated waveguide. It will be a powerful candidate of on-chip light source.
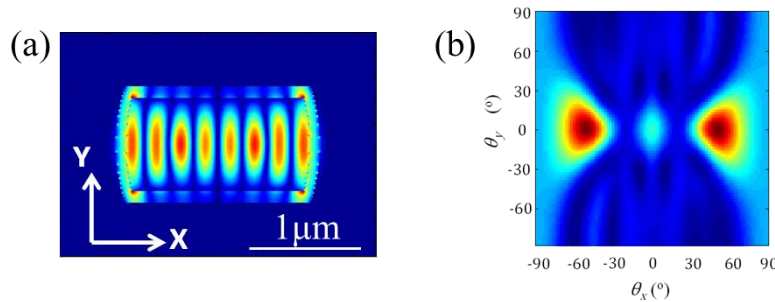
Figure 5.1 (a) Pattern of oscillating mode inside cavity. (b) Calculated far field pattern of the mode in (a) [33]

5.2 Capsule-shaped metal-coating cavity on waveguide

5.2.1 Device design

In order to realize waveguide-output of micro-laser, a single direction tapered waveguide adjacent to the capsule-shaped cavity is investigated. Figure 5.2 shows the device structure with detailed layer thickness indicated. We use the wafer stated in chapter 3.1.2. Comparing to the optical pumping device, an InGaAsP layer is inserted under InGaAs layer. The index of InGaAsP is 3.4, which is higher than 3.17 (index of InP). We expect such index difference afford a better confinement of propagating mode.
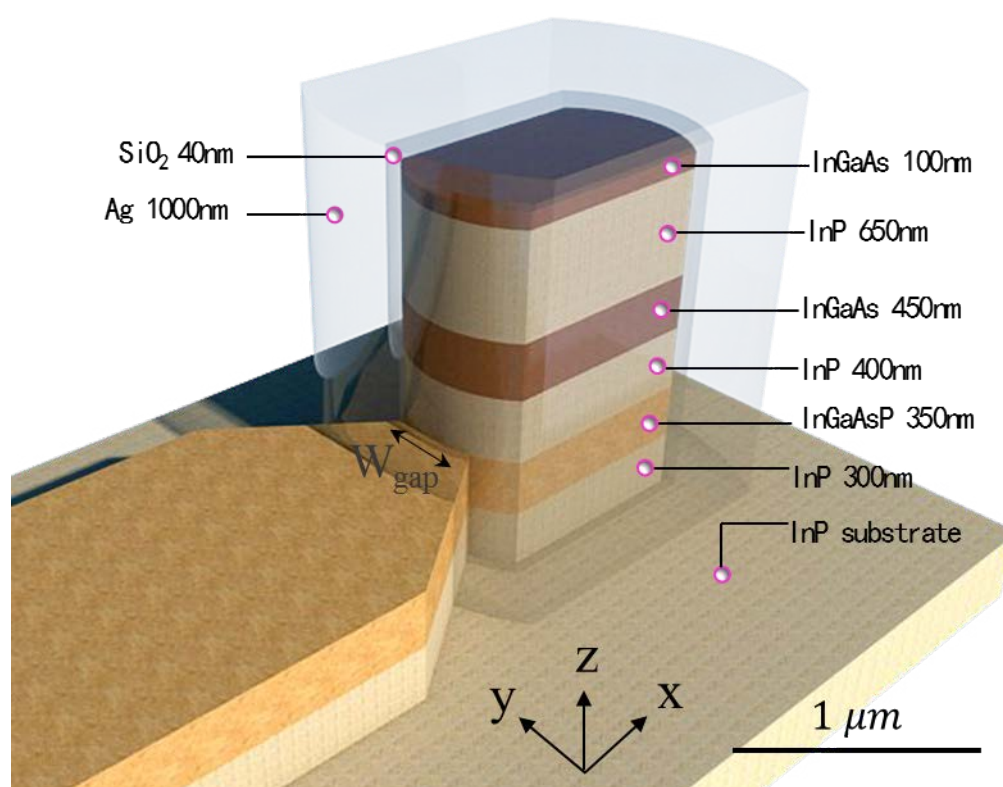
Figure 5.2 Schematic of coupling a capsule-shaped laser to the waveguide

A capsule-shaped cavity placed on waveguide. The distance between InGaAs and InGaAsP is a critical parameter that determine coupling efficiency between 2 layers. Too high coupling efficiency leads to high leaking rate of energy inside resonator, which makes lasing more difficult. On the other hand, low coupling efficiency will result in low output power. One should always take care of this trade-off carefully. A reasonable way is

to get experiment data from various sample with different parameter. However, to control the layer thickness during epitaxy is not easy, and the cycle of experiment will be quite long. We set the distance between InGaAs and InGaAsP to be 400 nm, which offers moderate coupling efficiency via numerical analysis. We have explored a practical way to engineer the output coupling efficiency by engineering the width of joint part (W_{gap} in Figure 5.2). The details are discussed in next part.

The core layer here is bulk $In_{0.53}Ga_{0.47}As$ with lattice matched to InP. The spontaneous emission is around 1550 nm. Upper clad of InP should be thick enough to isolate core layer from top metal electrode since metal could cause extra loss. It is difficult to dry etch very high mesa for practical reasons. Again, we determine the clad InP to be 650 nm thick via numerical calculation. Whole device is design as electrical-driven laser. Top p-contact layer is doped as high as $> 1 \times 10^{19}\ cm^{-3}$ to achieve low contact resist. Similarly to that in Chapter 4 , Ge/Ag is deposited to contact layer. N-contact is achieved via floor of mesa.

- **Relation of gap width and Q-factor**

We analyze the structure by 3D-FDTD simulation. The cavity size is set to be the same as the one characterized in Chapter 4 . Figure 5.3 shows electrical field distribution inside this device. In the core layer, the mode is similar to previous cavity. A proportion of power of the resonating mode couples to waveguide layer 400 nm below. This is shown in Figure 5.3(b). We regard it as a resonating mode of this 5-layered cavity. It reflects completely at left side of mesa while only partly reflects at right side since there is an outlet to waveguide, as shown in Figure 5.3(c). The cross section of the outlet is shown in the inset of Figure 5.3. It is a typical metal-insulator-metal (MIM) structure. Although guiding dielectric mode is cut-off because the width is no more than 1.0 µm, electromagnetic field inside cavity is able to radiate power toward waveguide through the gap. In another word, the gap works like an antenna. The amount of energy flow depends on the width of outlet.
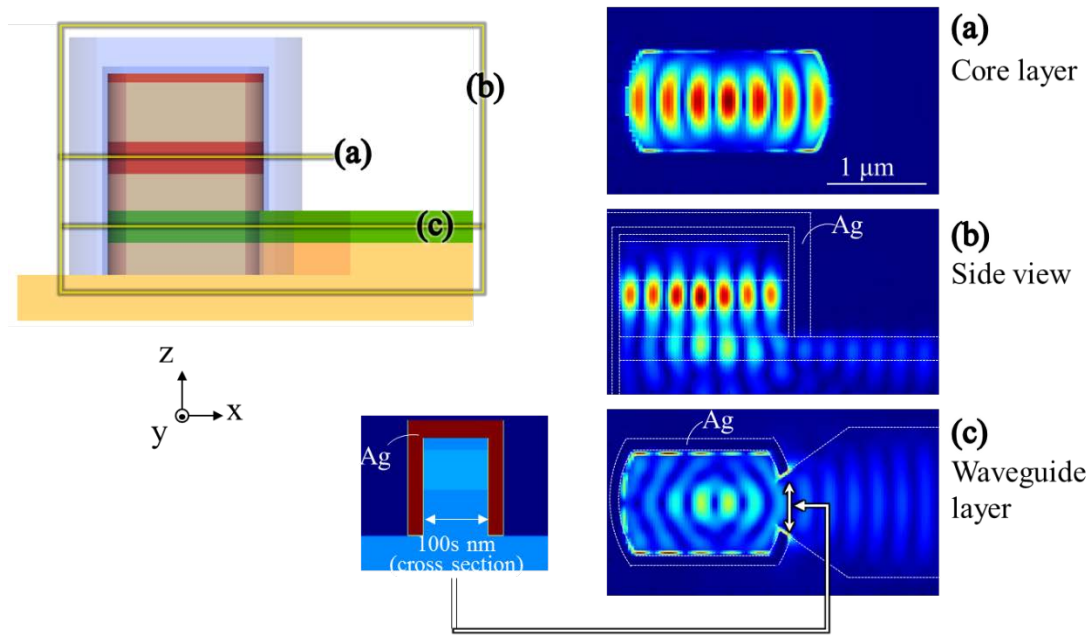
Figure 5.3 Electric field distribution in (a) InGaAs active layer, (b) side view of the whole structure, (c) InGaAsP layer

Such small cavity has very low Q-factor. It will be even less if a waveguide is coupled to cavity since energy leaks to outside. A quick way to suppress leakage is to make outlet narrower. Numerical calculation shows it is an effective way to tune overall Q-factor of such structure. Their relation is plotted in Figure 5.4. Detailed parameters of structure are illustrated in the graphic. Overall Q-factor varying from 440 (without waveguide) to 340 (the same as cavity itself) while W_{gap} changes from 0 to 1.0 µm. We plotted the corresponding threshold gain as well. Threshold gain is 564 cm^{-1} if gap width is 1.0 µm. Our previous work demonstrated an optical pumping wavelength-scale laser at room temperature, whose calculated threshold gain is around 550 cm^{-1}. From this study, the threshold gain of a waveguide-coupled wavelength-scale laser can be optimized to be around 500 cm^{-1} or less. Making it possible to start lasing. As compared to tuning Q-factor by modifying layer thickness, this method offers practical advantages. In particular, one can engineer device parameters based upon a trade-off between Q-factor and output power.

L = 1.6 μm, W = 1 μm, L/R = 1.25

SiO₂ 40nm
Ag 1000nm
W_gap

InGaAs 100nm
InP 650nm
InGaAs 450nm
InP 400nm
InGaAsP 350nm
InP 300nm

* Only TE mode is considered.
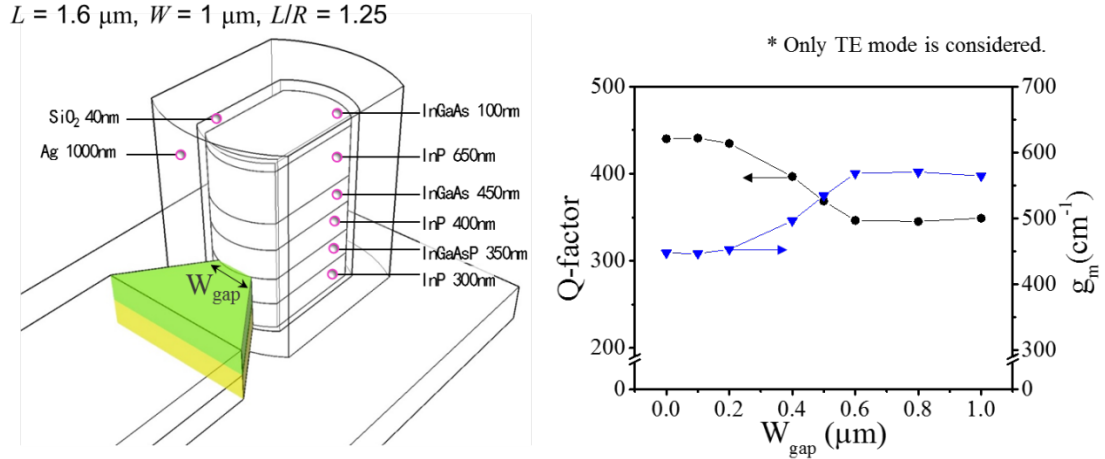
Figure 5.4 The relation between outlet width and Q-factor, gain threshold, respectively. Detailed parameters of structure are illustrated in graphic.

● **Coupling efficiency**

Generally, output power of laser depends on external coupling efficiency. A steady state of round-trip resonating light is illustrated in Figure 5.5. Light intensity (p_+ forward component, p_- backward component) gets stronger and stronger while travels along gain material, falls down at reflection mirror. Reflectivity of mirror is noted as R_1 and R_2, transmissivity is T_1 and T_2. For simplicity, we assume light intensity is constant in resonator, so we have $p_+(0) = p_+(L) = p_-(0) = p_-(L) = p_0$. Saturated coefficient can be written as

$$g = \frac{g_{ss}}{1+2p_0/p_{sat}} \tag{5-1}$$

Where g_{ss} is gain for a given pump intensity, p_{sat} is saturation intensity of the gain medium.
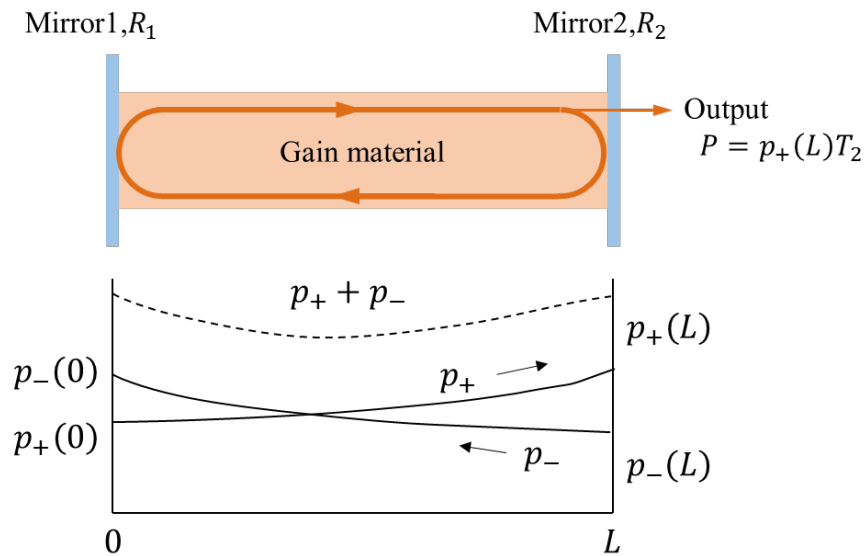
Figure 5.5 Schematic of energy flux intensity in an operating laser resonator

Solve p_0 from the equation, we get

$$p_0 = \frac{1}{2} p_{sat} \left(\frac{g_{ss}}{g} - 1 \right) \qquad (5\text{-}2)$$

As explained in Chapter 2 , in an resonating laser cavity, material gain is fixed to cavity optical loss coefficient.

$$gL = g_{th}L = \alpha_0 L + ln \frac{1}{\sqrt{R_1 R_2}} \qquad (5\text{-}3)$$

Where α_0 is intrinsic loss coefficient. L is resonator's length.

Considering single direction output at mirror 2, output power is

$$P = p_0(1 - R_2) \qquad (5\text{-}4)$$

Combining equations (5-2), (5-3) and (5-4), the relationship of output power and reflectivity can be written as a function of R_2

$$P = P_{sat} \left(\frac{2g_{ss}L}{2\alpha_0 - ln(R_1 R_2)} - 1 \right) (1 - R_2) \qquad (5\text{-}5)$$

If reflectivity R_2 is close to 1, little power is transferred to outside, output power will be near to 0. If R_2 is close to 0, it will be hard to restore power inside resonator. Consequently, no power is obtainable. Thus, an optimized value of reflectivity does exist.

However, it is hard to apply this simple theoretical model to our design shown in Figure 5.2 because the difficulty of calculating reflectivity of the arc-shaped mirror exactly.

In order to find out the proportion of power that coupled into waveguide for this specific case, we look into the detailed component of overall Q value. Considering steady lasing state of a cavity. The loss during the resonating is consist of three part, as shown in Figure 5.6.

$$E_{loss} = E_{metal} + E_{dis} + E_{wg} \qquad (5\text{-}6)$$

Where E_{metal}, E_{dis}, E_{wg} represents absorption by metal, dissipation to free space, energy coupled into waveguide, respectively. These three parts can be easily obtained by calculating poynting vector during 3D-FDTD simulation.
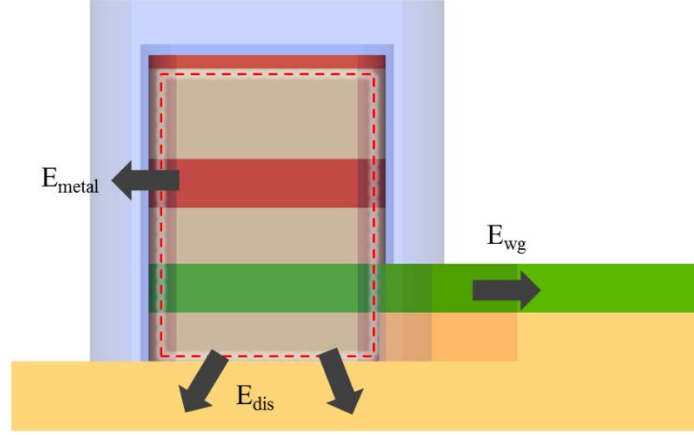
Figure 5.6 Energy loss from cavity

Since Q-factor is inversely proportional to loss, the overall Q value can be expressed as below.

$$\frac{1}{Q} = \frac{1}{Q_{metal}} + \frac{1}{Q_{dis}} + \frac{1}{Q_{wg}} \qquad (5\text{-}7)$$

The Q factor of a resonant cavity is defined as

$$Q = \frac{2\pi f_0 E}{P} \qquad (5\text{-}8)$$

Where the E is the stored energy inside the resonator, $P = -\frac{dE}{dt}$ is the power dissipation rate, f_0 is the resonant light frequency. From this equation, we can write optical energy E as a function of time t

$$E(t) = E(0)e^{-\frac{2\pi f_0}{Q}t} \qquad (5\text{-}9)$$

By using Maclaurin series of exponential function, this equation can be approximately written as

$$E(t) = E(0)e^{-\frac{2\pi f_0}{Q}t} = E(0)\left(1 - \frac{2\pi f_0}{Q}t + o\left(\frac{1}{Q^2}\right)\right) \qquad (5\text{-}10)$$

Where $o\left(\frac{1}{Q^2}\right)$ is infinitesimal of $\frac{1}{Q^2}$. The loss of energy is then

$$E_{loss} = E(0) - E(t) = \frac{2\pi f_0}{Q}t \cdot E(0) \qquad (5\text{-}11)$$

Combining equation (5-7) and (5-11), we have

$$E_{loss} = \frac{2\pi f_0}{Q}t \cdot E(0) = \left(\frac{1}{Q_{metal}} + \frac{1}{Q_{dis}} + \frac{1}{Q_{wg}}\right)2\pi f_0 t \cdot E(0)$$
$$\equiv E_{metal} + E_{dis} + E_{wg} \qquad (5\text{-}12)$$

Next, we calculate the E_{metal}, E_{dis} and E_{wg} through 3D FDTD simulation. As shown in Figure 5.7, closed surface of cube S₁ is set inside cavity, which is slightly smaller than silver coatings. Similarly, closed surface of cube S₂ a bit larger than silver coatings is set to cover whole cavity. A y-z plane S3 is set at waveguide area. The pointing vector is calculated by $\vec{P} = \vec{E} \times \vec{H}^*$. Surface integrals of vector field $\vec{P}$ represents the power leaves the cube or

passes through given plane.

$$A_1 = \oiint_{S1} \vec{P} \, d\Sigma \qquad (5\text{-}13)$$

$$A_2 = \oiint_{S2} \vec{P} \, d\Sigma \qquad (5\text{-}14)$$

$$A_3 = \iint_{S3} \vec{P} \, d\Sigma \qquad (5\text{-}15)$$

Approximately, A_1 can be regarded as all of the loss, or $A_1 = E_{loss} = E_{metal} + E_{dis} + E_{wg}$. Since electromagnetic field cannot penetrate metal, power leaves cube S2 is $A_2 = E_{dis} + E_{wg}$. Lastly, $A_3 = E_{wg}$ is simply the energy flows through waveguide. Thus, we can specify each component of overall loss E_{loss}.
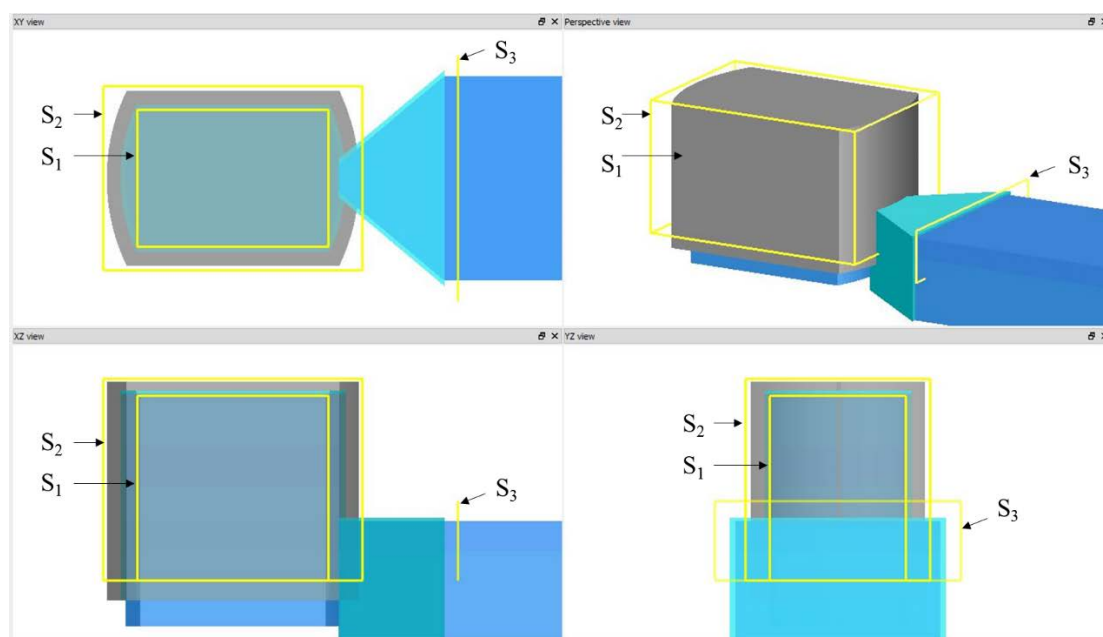
Figure 5.7 Schematic of energy flow calculation

We analyzed the E_{loss} when W_{gap} changes. Figure 5.8 shows the result. Detailed values are summarized in Table 5-1 and Table 5-2. All the structure parameters are the same as previous example. Left y-axis is overall Q factor as a function of outlet width. Right y-axis is loss rate of restored energy inside cavity. Different colored area $1/Q_{metal}$, $1/Q_{dis}$ and $1/Q_{wg}$ are proportional to optical loss E_{metal}, E_{dis} and E_{wg}, respectively, and $1/Q = 1/Q_{metal} + 1/Q_{dis} + 1/Q_{wg}$.

Overall Q factor drops from 453 to 328 while width of joint varies from 0 to 1.0 μm as a function of W_{gap}. Power that coupled into waveguide keeps increasing while W_{gap} increases. At the same time, dissipation loss increases a bit as well. When W_{gap} becomes more than 0.5 μm, Q_{wg} get close to Q_{dis}. External extraction efficiency (last row of Table

5-1) can reach 10~20%. Assuming internal efficiency is 1%, an output of 1 μW could be obtained while injection power is 1 mW. It is practicable for use in photonic integrated circuit.
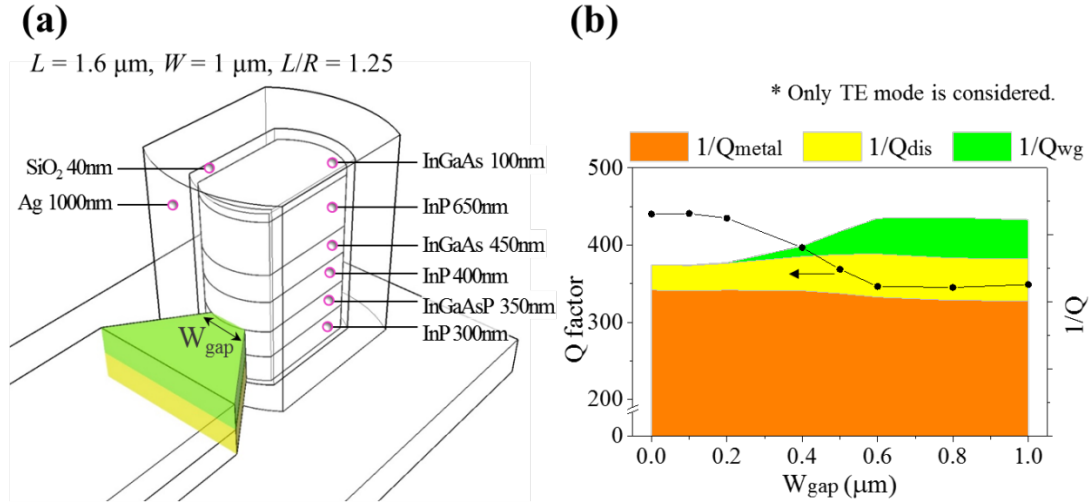
Figure 5.8 Changes of overall loss while W_{gap} varies.

Table 5-1 Percentage of power loss rate ($1/Q_{metal}$, $1/Q_{dis}$ and $1/Q_{wg}$)

W_{gap}(μm)	0	0.1	0.2	0.4	0.5	0.6	0.8	1.0
$1/Q_{metal}$, E_{metal}(%)	85.3	85.0	84.2	76.5	69.8	63.8	62.1	62.6
$1/Q_{disl}$, E_{dis}(%)	14.7	14.7	15.4	18.0	19.0	19.8	19.3	19.4
$1/Q_{wg}$, E_{wg}(%)	null	0.3	0.4	5.5	11.2	16.4	18.6	18.0
$E_{wg}/(E_{wg}+E_{dis})$(%)	0	1.8	2.2	23.3	37.0	45.1	48.9	48.0

Table 5-2 Calculated values of Q_{metal}, Q_{dis} and $1/Q_{wg}$ ($1/Q=1/Q_{metal}+1/Q_{dis}+1/Q_{wg}$)

W_{gap}(μm)	0	0.1	0.2	0.4	0.5	0.6	0.8	1.0
Q	440	441	435	397	369	346	345	349
Q_{metal}	516	519	516	518	528	543	556	557
Q_{dis}	2985	2993	2819	2205	1935	1746	1784	1797
Q_{wg}	null	1.6e5	1.2e5	7250	3296	2122	1863	1943

If we define coupling efficiency η_{wg} as $\eta_{wg}=E_{wg}/(E_{wg}+E_{dis})$ (Table 5-1), we can see that the efficiency reaches 37% when the width of joint is 0.5 μm. The efficiency does not improve too much then the width of joint gets larger than 0.5 μm.

Another point is that Q_{metal} does not change a lot, always larger than Q_{wg}. In another word, metal induced loss accounts more than 60% of overall loss. This limits the laser's performance. It is necessary to search alternative plasmonic material that has high reflectivity like metal and low absorption coefficient at the same time if one want to improve the performance of wavelength-scale metal-clad laser.

- **Device on SOI wafer**

(a)
$L = 1.6\ \mu m$, $W = 1\ \mu m$, $L/R = 1.25$

(b)
* Only TE mode is considered.
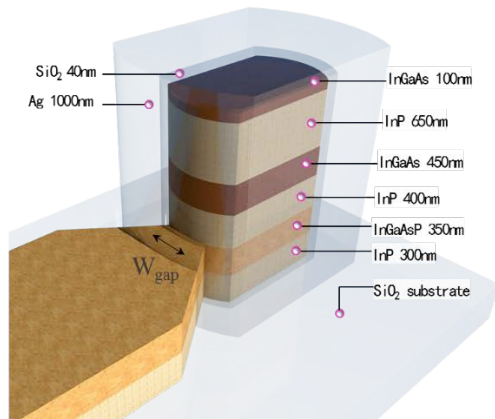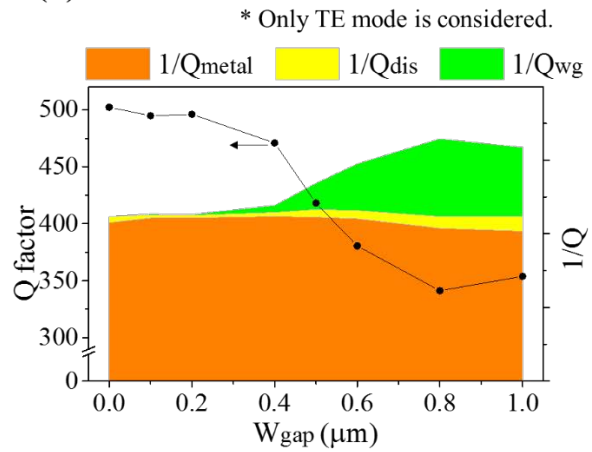
Figure 5.9 Schematic of waveguide-coupled cavity on SiO_2. Overall Q factor and loss as a function of W_{gap}.

The confinement is weak at vertical direction so that lots of power leak to substrate. If we replace the substrate InP with SiO_2, which is possible by bonding the InP wafer to a SOI wafer, the leakage from bottom will be significantly reduced. Schematic image is shown in Figure 5.9(a). Refractive index of SiO_2 is 1.45, which is far below 3.17 of InP. Figure 5.9(b) shows each component of loss changes as a function of joint width. Maximum of loss through substrate is reduced to only 6%.
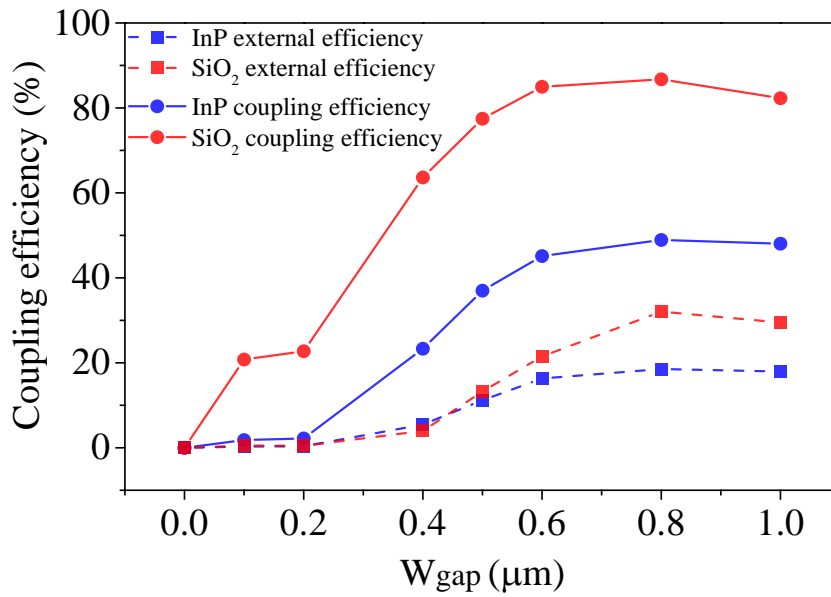
Figure 5.10 Coupling efficiency and external efficiency of InP-substrate device and SiO$_2$-substrate device. Coupling efficiency $= \frac{E_{wg}}{E_{dis}+E_{wg}}$, external efficiency $= \frac{E_{wg}}{E_{metal}+E_{dis}+E_{wg}}$, where E_{metal}, E_{dis}, E_{wg} are illustrated in Figure 5.6.

Figure 5.10 is comparison of calculated coupling efficiency and external extraction efficiency of SiO$_2$-substrate device and InP-substrate device. When the joint width increases to over 0.4 μm, coupling efficiency of SiO$_2$-substrate device rises to more than 60% and reaches maximum of 87%. It is twice of that of InP-substrate device. The overall quality factor is averagely larger as well, which means threshold could be reduced.

The SiO$_2$ is not conductor so current have to pass through waveguide layer when we pump it by electric. The current density goes high at the joint between waveguide and cavity, the narrowest part of current path. It will bring another problem of heating. SiO$_2$ is also of low thermal conductivity. Heat accumulates at cavity and bring negative effect on emission. The only way is to make metal electrode spread widely which can work as heat sink. Overall footprint gets large consequently. A well-considered thermal dissipation design is necessary.

- **Tolerance of patterning error**
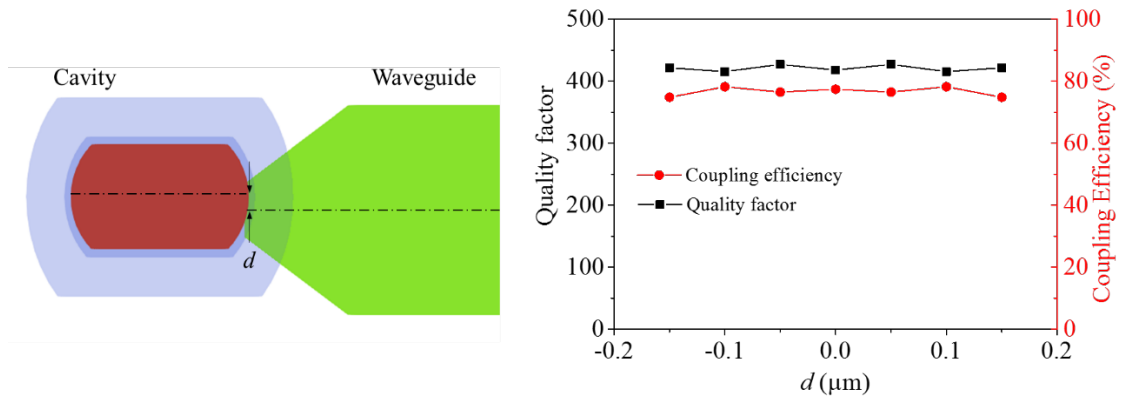
Figure 5.11 Q factor and coupling efficiency when coupled with a misaligned waveguide.

We checked the tolerance of this design to alignment errors that may occur during fabrication. The W_{gap} is fixed to 0.5 μm, substrate is set to SiO_2, cavity length is 1.6 μm, and cavity width is 1.0 μm. The alignment error of our equipment is up to 200 nm. So we investigated the tolerance in this range. As shown in Figure 5.11, d represents the misalignment in lateral direction. The quality factor and coupling efficiency do not change much when mismatched. This is because cavity and waveguide both support single-mode. For 1.55 μm infrared light, its effective wavelength in InP is about 500 nm. It is reasonable that a mismatch less than half wavelength cause little effect on cavity performance. Further simulation shows that a InP-substrate device has similar tolerance.

For the misalignment in longitude direction, the width of joint will change actually. The resulted effect is discussed above. The tolerance depends on the slope of taper. Longer taper will make device more insensitive to the error but result in larger overall footprint.

5.2.2 Measurement setup

Probes are used to contact the electrode on chip and inject current. A lensed fiber is used to collect light from 2 μm wide InP waveguide, and redirect it to a spectrometer. The photodetector of spectrometer is cooled down to minus 100 centigrade to eliminate thermal noise. A problem of such simple setup lies in alignment. We use a red laser pointer to input light from opposite side of fiber. Then through microscope, we can see

the light hit the facet of chip. Make sure the light spot hits exactly the waveguide facet by adjusting position of fiber. Then, preliminary alignment is done.
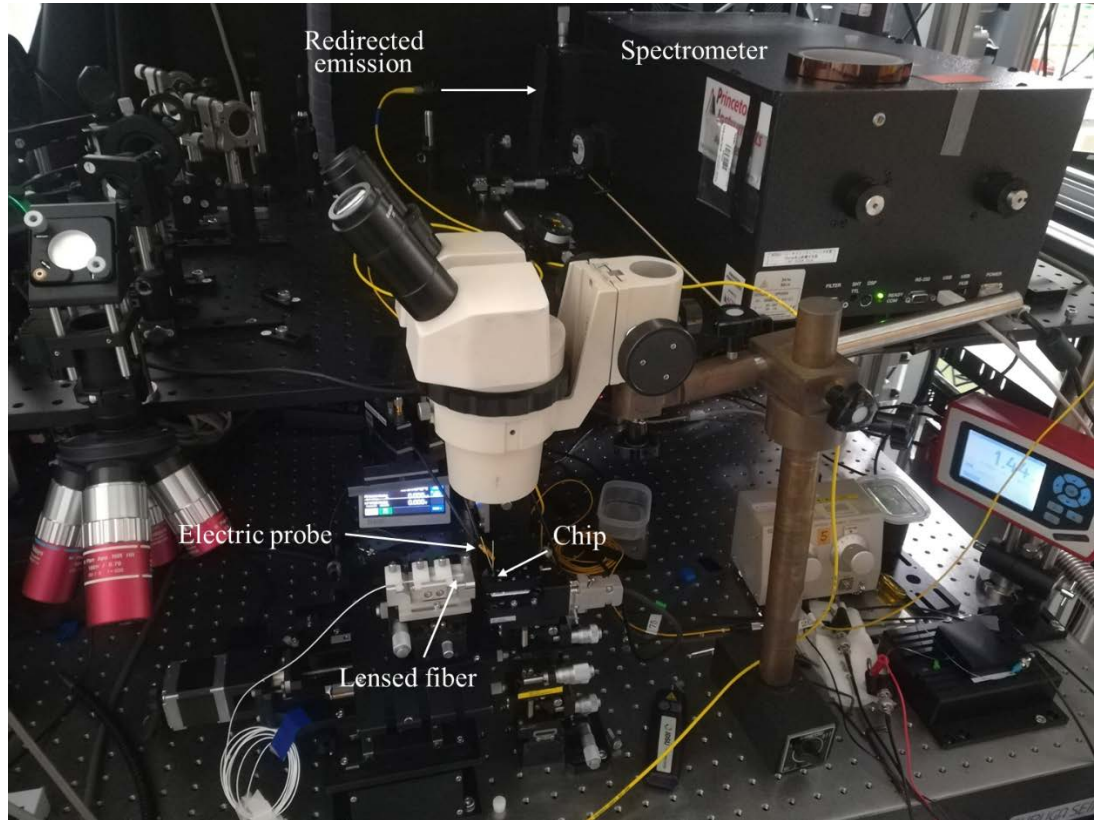
Figure 5.12 Measurement setup of electrical pumping waveguide-coupled device

Next, a commercial 1550 nm laser source is used to check fiber output optical axis is aligned to spectrometer's iris correctly. 1 mW output of laser source is weakened by 50 dB by attenuator. Expose time of spectrometer is 1 second. The alignment is no problem if a clear peak can be seen at 1550 nm. Otherwise, adjust optical axis of fiber output again.

When everything is ready to measure fabricated samples, change expose time of spectrometer to 30 seconds or more because signal from device is quite weak. It is better to use longer expose time, but no recommended to use more than 3 minutes as fiber is instable, moving gradually all the time. Actually, we used expose time of 2 minutes to take measurement 3 times continuously without any intentional changes, each result was different with others and peak intensity tended to drop as time elapses. Considering this, measurement done by less expose time yield more reliable data.

5.2.3 Experimental result
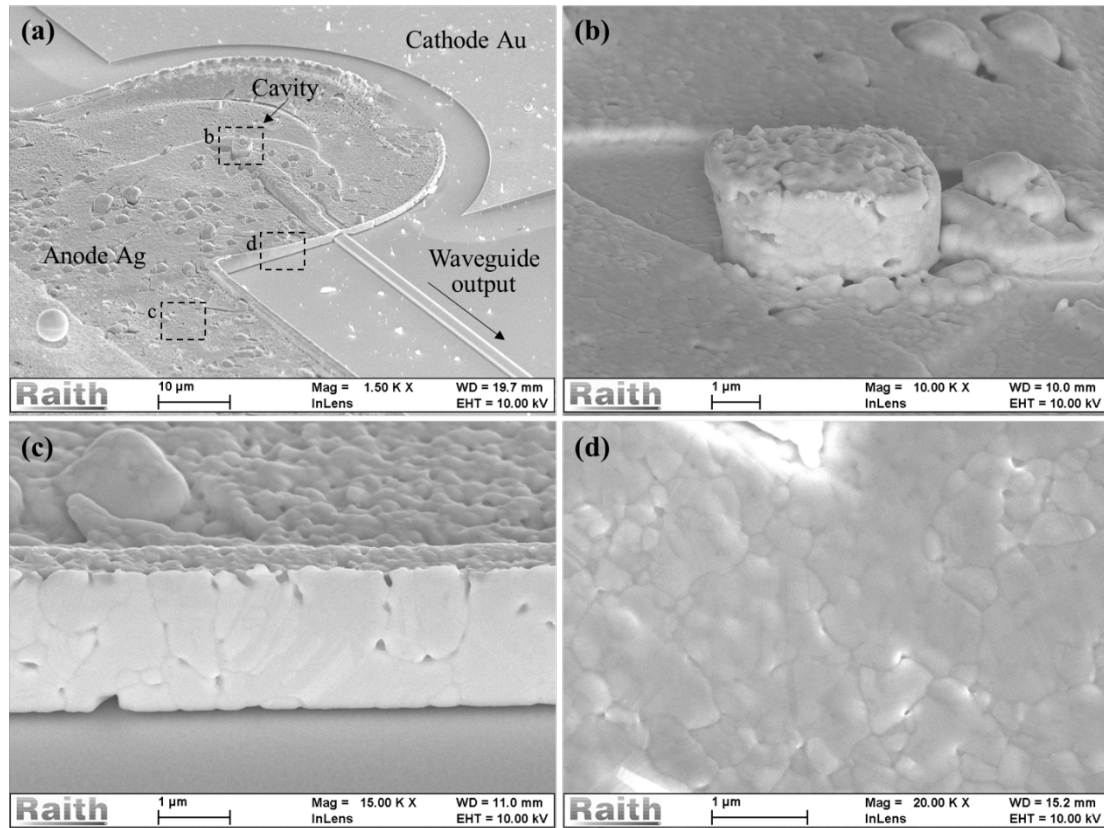
Figure 5.13 (a) Scanning electron microscope image of fabricated waveguide-coupled semiconductor laser cavity. Zooming-in of (b) the cavity, (c) edge of Ag electrode after annealing, (d) surface of Ag electrode.

We fabricated the device structure presented in Figure 5.2 with various cavity dimensions, and measured the light emission from the output waveguide at room temperature. The scanning electron microscope image of the completely fabricated device including electrode is shown in Figure 5.13(a). Figure 5.13(b) is a zooming in of cavity. The cavity is covered by metal completely. The outer surface looks quite rough but we think the inner interface of metal is smooth. An indirect evidence is shown in Figure 5.13(c). It is the edge part of electrode on the top of SiO_2 passivation. The exposed surface is very smooth after annealing. We can even see crystal stream in the image. Figure 5.13(d) is top surface of Ag electrode. The grain size is up to 1 μm suggesting that the annealing is successful.

Generally, one should try optical pumping waveguide-coupled laser before electrical pumping. However, because we used metal-clad cavity in this work, we cannot try optical

pumping from the top of the device. If we flip the chip over to do the optical pumping, it would be difficult to align fiber to waveguide since we cannot see cavity and waveguide from backside. The waveguide and cavity would be visible after removing InP substrate. The substrate is 325 μm thick. Removing it by HCl etching would followed by problems such as cracking or breaking up from side of the chip. Therefore, we tried removing substrate 300 μm away by polishing, and used diluted HCl to etch remained substrate completely. We spin coated 2 μm thick polyimide on the top of chip, annealed at 200 centigrade to harden the polyimide to protect devices on the chip surface. Then flipped the chip over and bonded it to a silicon carrier by wax, and polished the backside substrate. However, the chip had a large chance to break up after the polishing. We thought the chip was not bonded to carrier horizontally. It is tilted at several degrees. During the polishing, the non-uniform pressure broke the chip.
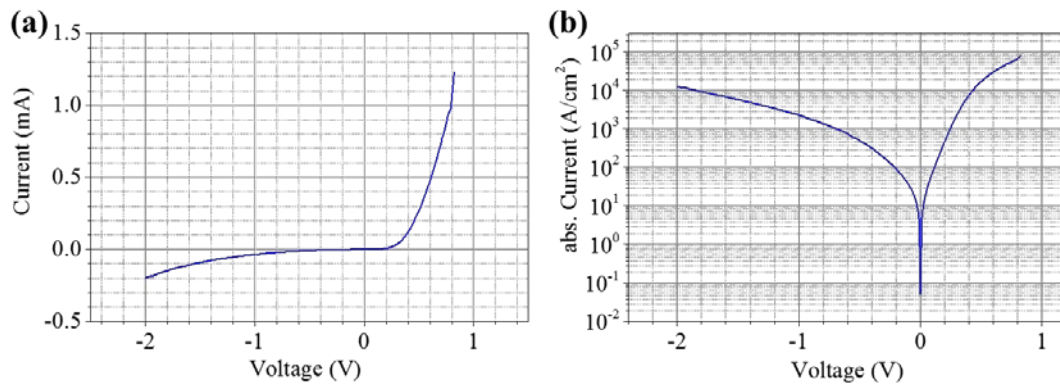
Figure 5.14 I-V response of a 1×1.6 μm^2 laser diode. (a) Linear plot. (b) Log scale plot of current density via voltage.

Thus, we tried to do the electrical test directly. The current is injected through probe touched to the electrode softly. It is easy to under the microscope view. We checked the p-n junction characteristic of fabricated devices. Figure 5.14(a) shows a linear plot of I-V response. Asymmetric conductance is observed. Turn-on voltage of the laser diode is around 0.4 V. Figure 5.14(b) is a log-scale plot of current density via voltage. Since the area of diode is as small as 1×1.6 μm^2, current density is very large even total current is only 1.0 mA. In forward bias area, two different slope line segments are observed. The data lose reliability (instable and unrepeatable) when current gets larger than 1.0 mA.

The reverse bias current is a bit large. A possible reason is that surface defects

density is high so surface leakage current is large. For such small diode with high surface-to-volume ratio, this is a fatal problem. A careful surface treatment (using acid solution) could suppress surface leakage current [78]. The heating caused by high current density could also cause the significant increase of reverse current.

We employed lensed fiber to collect emission from 2 μm-wide InP waveguide at the edge of the chip. We aligned the fiber to the waveguide by the help of top view under microscope. Figure 5.15 is a preliminary result, showing the optical spectrum for the cavity length of 3 μm, width of 1.5 μm, and Wgap = 0.8, observed under continuous electrical pumping. As we increase current from 1.5 mA to 3 mA (corresponds to a current density of 66.7 kA/cm2), increase of the spontaneous emission is clearly observed. Although the Q factor is not sufficient to achieve lasing, this is the clear evidence that the spontaneous emission inside the capsule-shaped cavity is coupled to the InP waveguide. We also tried pulse electrical pumping. Pulse width is 0.5 μs, repetition rate is 20 kHz. Observed emission spectrum is similar to continuous wave current pumping.
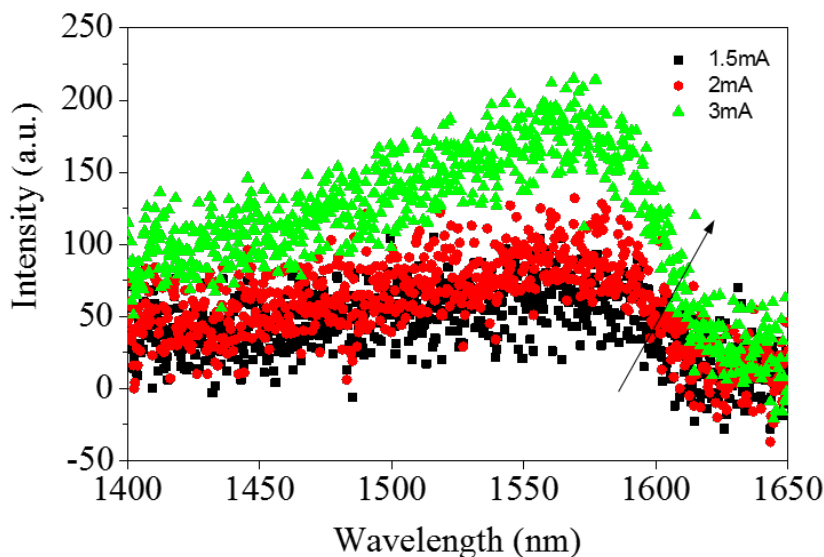
Figure 5.15 Measured spectrum from output waveguide

5.2.4   Discussion

We used the successful design discussed in Chapter 4 to try waveguide coupling. We

get LED output from waveguide successfully. For small cavity under current pumping, even 1 mA current will cause temperature increases over 20 centigrade in active layer [74]. Emission efficiency falls down. Obtainable optical gain is not enough to compensate extra loss induced by waveguide to achieve lasing. Further study such like low temperature test need to be done to analyze device performance.

Chapter 6   Conclusion

In this research, wavelength-scale metal-clad laser is studied. We used capsule-shaped cavity proposed in previous work to increase quality factor. We fabricated capsule-shaped cavities and rectangular cavities both with length of 1.6 μm and width of 1.0 μm, tested them by pulsed optical pumping at same condition. They both achieved room temperature lasing. The estimated threshold is 230 μW. Capsule-shaped cavity has better side-mode compression ratio and higher slope efficiency comparing to rectangular cavity.

We compared capsule-shaped cavities. They have a same length of 1.6 μm, but their width varies from 1.4 μm to 2.0 μm. Their simulated quality factors are all around 405. Experiment result shows that the larger dimension is the higher threshold is. In another word, smaller laser cavity has higher efficiency.

We tried to extract the light in a capsule-shaped cavity using a coupled waveguide. Simulation analysis gives acceptable coupling efficiency and quality factor. We fabricated samples and tested them by electric pumping. Spontaneous emission was observed from the output waveguide from fabricated device when pumping current is 1.5 mA. Extracting light is successful, but it needs more study to achieve waveguide-coupled lasing.

There are some trivial tips to improve this work. Optical pumping or low temperature test could help study device's performance. By comparing measurement data with simulation, we can improve simulation model. Improve of fabrication will also contribute to device's performance.

However, we should pay attention to several important issues to promote this research significantly in the future.

- Replace InP substrate with SOI substrate

In this work, all the samples are fabricated on InP substrate. Light confinement is weak at bottom. 20% of total loss dissipates into substrate. That number can decrease to 4%

if replace InP substrate (index 3.17) with SOI (index of SiO_2 is 1.45). Coupling efficiency could reach 85%. This is possible by wafer die bonding widely used in integration of InP and silicon photonics [79].

- Absorption of metal

In our calculation, metal absorption loss in waveguide-coupled laser/LED accounts for about 60% in total loss. According to free electron model in metal, free-electron scattering increases with increased temperature [80], which further increases scattering assisted absorption [81]. In a real sample, metal-induced loss could be easily over 60% in total loss, which degrades device performance a lot.

The electron density in metal is typically of order 10^{22} cm^{-3}. Semiconductors with heavy dope of 3×10^{20} cm^{-3} could exhibit negative real permittivity at near optical frequency [82], meanwhile show low absorption loss because their much lower free-electron density compared to that of metal. ITO (mixture of In_2O_3 and SnO_2), AZO (aluminum-zinc-oxide) and GZO (gallium-zinc oxide) [82] [83] are reported to show negative real permittivity at near infrared wavelength. AZO and GZO could have plasma frequency below 1.5 μm. Such materials could improve wavelength-scale plasmonic laser greatly.

- Further optimization of cavity structure by inverse design method

As mentioned in section 4.2.4, there is room to improve the design of cavity. Since the resonating is dominated by Maxwell equations, it is hard to find out analytic solution to this problem. Inverse design method [75] [76] conducted by numerical computation offers a way to figure out best answer of this problem.

- New gain material

Large net gain is needed to overcome overall loss in nano-laser at room temperature. That results in large injection power and threshold. People are searching for better gain materials. Recently, lasing based on a monolayer transition-metal dichalcogenides (TMDs)

was reported [84]. Another work demonstrated lasing by a monolayer tungsten diselenide (WSe$_2$) [85]. Such materials with high photoluminescence quantum yield could reduce threshold of nano-laser for integrated chip systems.
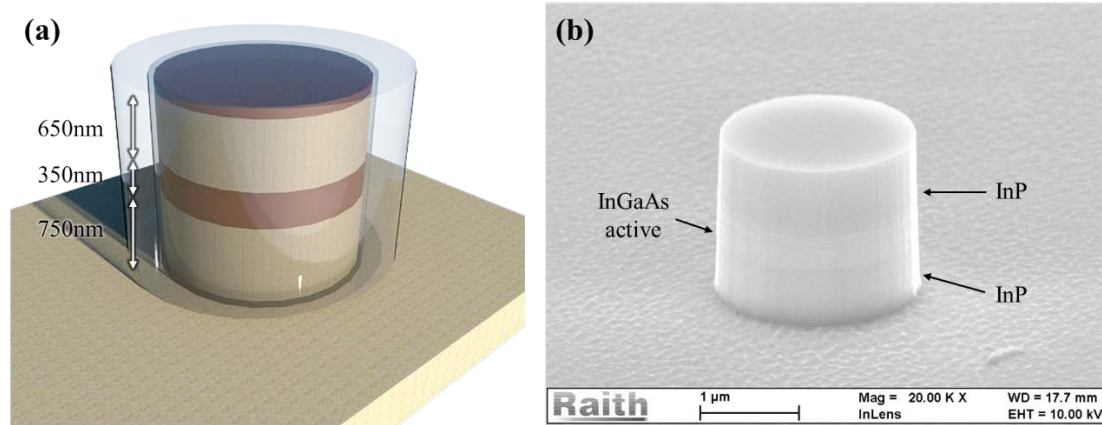
Appendix, lasing from a micro-disk cavity

Figure 0.1 (a) Schematic image of micro-disk cavity coated with SiO_2 and silver. (b) Fabricated micro-disk cavity before SiO_2 and silver coating. Radius of the cavity is 1.0 µm.

We also tried micro-disk cavity. Figure 0.1(a) is schematic image of the micro-disk cavity, Figure 0.1(b) is scanning electron microscope image of a fabricated micro-disk cavity with a radius of 1.0 µm. There are already a lot of research on it. Light propagates along the circumference by total internal reflection, forming so-called whispering gallery mode [86] [87].

A micro-disk cavity with radius of 1.0 µm achieved lasing in my experiment. We studied its optical characteristic by computation. Figure 0.2(a) is calculated resonating spectrum. We put several light source at different position with different polarization to excite all the modes. The electrical field distributions are summarized in Table 0-1, including whispering gallery modes (1425nm and 1534nm), plasmonic modes (1457nm and 1584nm), and Fabry-Perot like modes. Figure 0.2(b) is measured emission spectrum under optical pumping. The lasing peak is at 1521 nm, measured half width is 0.3 nm. We attribute it to whispering gallery mode (1534 nm) because it has a quality factor of 432, higher than that of the mode at 1519 nm.

Since micro disk cavity is a rotationally symmetric system, the lasing mode equally dissipate to all direction. In our experiment, the cavity is covered by metal, evanescent light will no longer effect nearby devices. This can increase integration density. A

waveguide-coupled 8-µm-radius micro disk laser was demonstrated [88]. For a 1-µm-radius micro disk, waveguide coupling is challenging because effective width of mode is much smaller than that of a waveguide which typically over 1 µm, coupling efficiency is quite low.
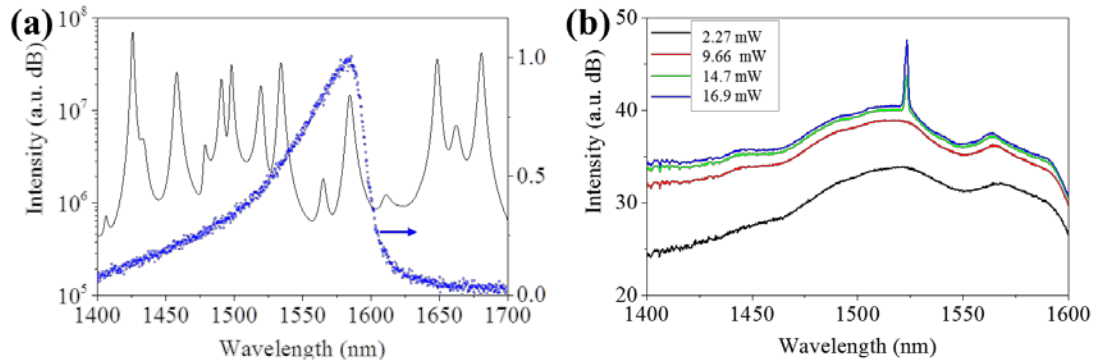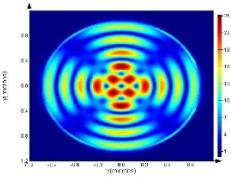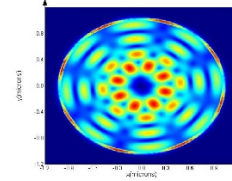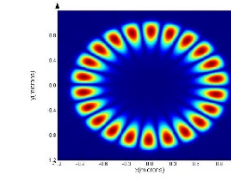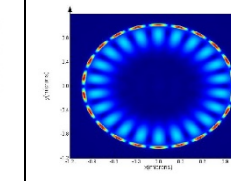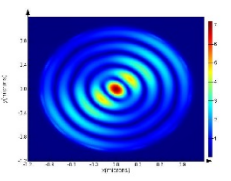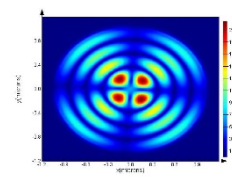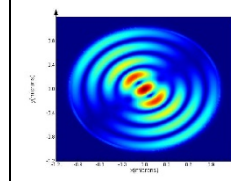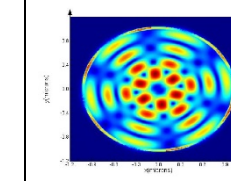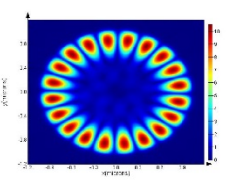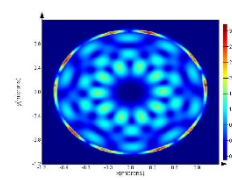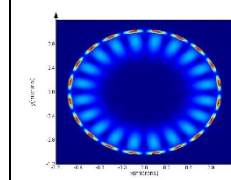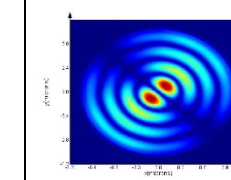
Figure 0.2 (a) Simulated resonating spectrum of a micro disk cavity, whose radius is 1.0 µm. Blue scatter is normalized measured photoluminescence of active material. (b) Measured emission spectrum of a fabricated micro disk cavity under optical pumping. The value indicates the output of pumping laser.

Table 0-1 Electrical distribution of each mode inside a micro disk cavity whose radius is 1.0 µm.

1364nm	1388nm	1425nm	1457nm
1479nm	1491nm	1499nm	1519nm
1534nm	1563nm	1584nm	1646nm

In this chapter, we first numerically studied the metal-clad cavity. Cavity's size, insulator's thickness, and the selection of metal are relative to cavity's performance. Capsule-shaped cavity enhances TE mode's quality factor. We confirmed this effect by

optical pumping two kinds of cavities and testing their emission spectrum. From the experiment data, we can see side-mode suppression ratio of capsule-shaped cavity is higher than rectangular one.

We also test several different capsule-shaped cavities. The result tell us that small cavity exhibits higher efficiency than large ones. All the measurement are done at room temperature by 1030 nm pulsed optical pumping.

We tried continuous wave pumping. In that case, cavities achieved lasing for around 10 seconds, and then spectral peak fell down and disappeared. Finally, it degraded to LED emission. This suggests heating is still a problem in our devices. It will decrease emission efficiency of active layer and increase absorption loss of metal.

A 1.0 µm-radius micro-disk cavity is also observed lasing. The resonating mode of it is quite complicated. Spontaneous emission factor is lower than capsule-shaped one and rectangular one. It is difficult for such a small micro-disk cavity to couple with waveguide. A schematic view of waveguide coupling of micro-disk is shown in Figure 0.3. Since the whisper-gallery mode is located at edge of cavity, we place waveguide at one side of the micro-disk in order to increase coupling efficiency as much as possible. The radius of micro-disk is 1 µm. The waveguide is 1 µm wide near the cavity and extends to 2 µm at far position (which is not shown in the figure).
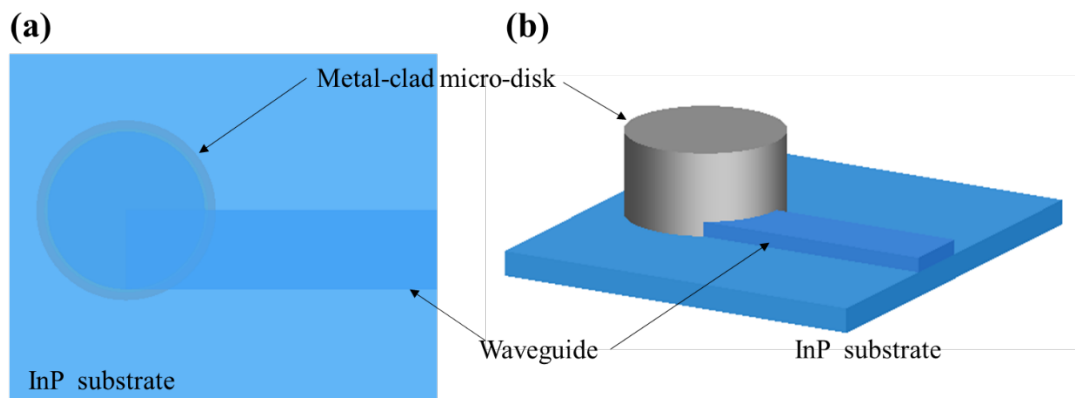
Figure 0.3 Schematic of waveguide coupling of micro-disk. (a) Top view. (b) Perspective view.

Figure 0.4 shows the coupling of the whisper-gallering mode. As we mentioned before, because the mode is not guided in a single direction, it is not easy to couple it into a directional waveguide. in the Figure 0.4(a), we can see that most of the energy is not

conveted to waveguide mode. We plot the poynting vector of the mode in Figure 0.4(b). The arrows represent the propagating direction of the light. They are circulating inside the micro-disk, and tends to dissipate to every direction. The smaller the cavity is, the more divergent the mode tends to be. This is a intuitive explanation that why waveguide coupling of whisper-gallery mode is more challenging than Fabry-Perot like mode in small micro-disk cavity. When the radius of micro-disk goes to 10 µm or larger, the component of light whose propagating direction is similar to waveguide increases. Therefore, a large (radius > 10 µm) micro-disk is easier for waveguide coupling [89]. It is not a good choice for ultra-small wavelength-scale on-chip light sources.
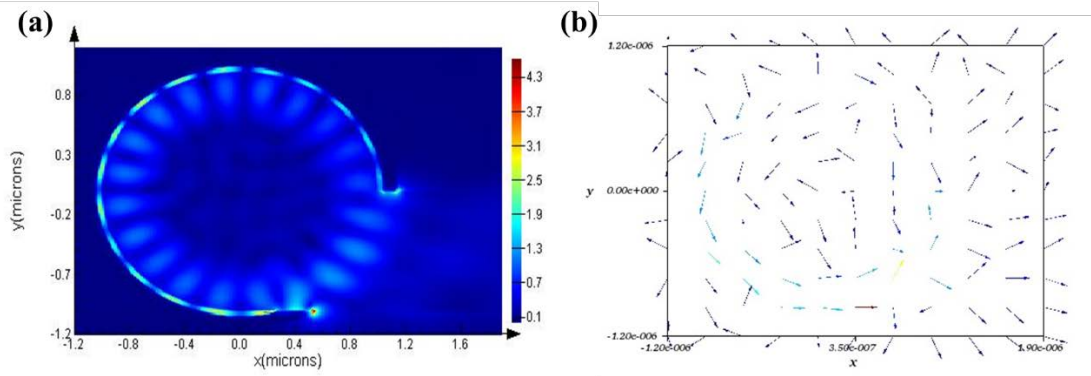
Figure 0.4 Waveguide coupling of the optical mode. (a) Electric field distribution. (b) Vector plot of pointing-vector.

We fabricated series of waveguide-coupled micro-disk cavity, in order to compare with capsule-shaped cavity in Chapter 5 . Figure 0.5 is a fabricated waveguide-coupled micro-disk cavity. Unfortunately, we do not have output LED emission from this device yet. Further investigation need to be done in future works.
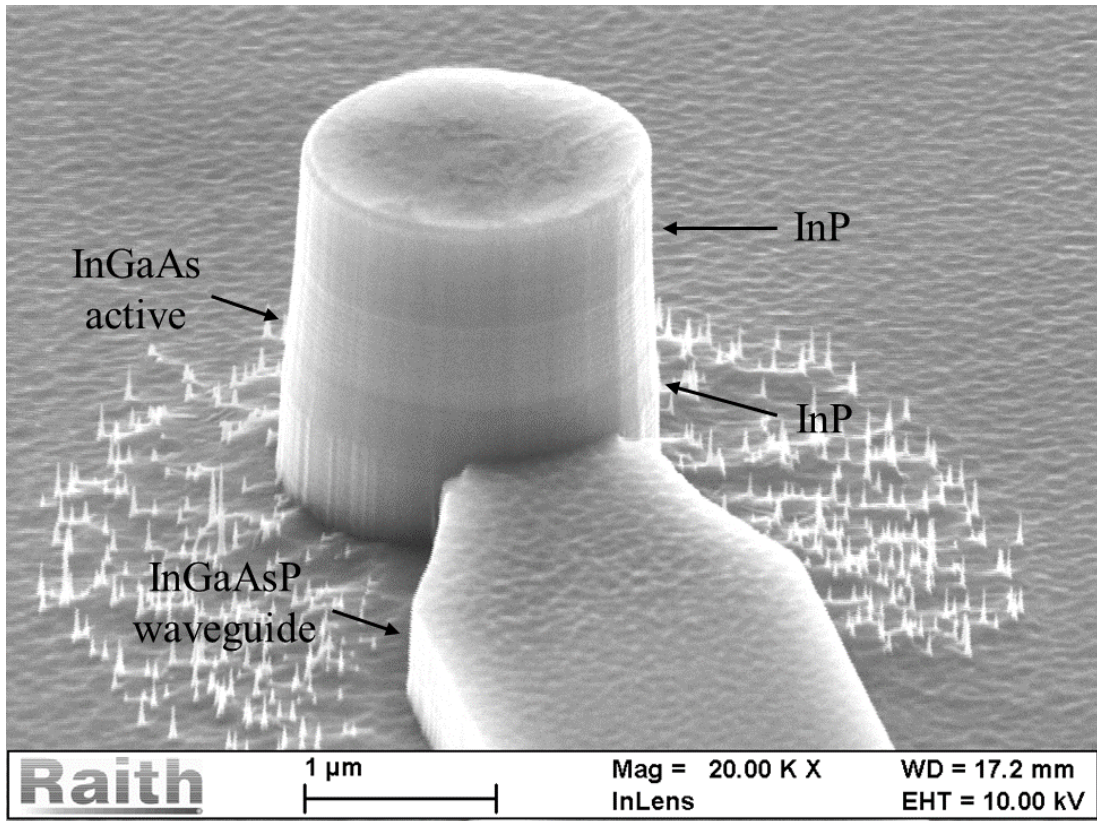
Figure 0.5 Scanning electron microscope image of fabricated waveguide-coupled micro-disk cavity.

Publications

Journal

1. Yi Xiao, Richard J.E. Taylor, Chuangqing Yu, Kaiying Feng, Takuo Tanemura, and Yoshiaki Nakano, Room-Temperature Capsule-Shaped Wavelength-Scale Metal-Clad Laser Operating at 1550 nm, Appl. Phys. Lett. 111, 081107 (2017)

2. Yi Xiao, Mitsuhiro Watanabe, Yuguang Wang, Takuo Tanemura, and Yoshiaki Nakano, Waveguide Coupling of Wavelength-Scale Metal-Clad semiconductor emitter, to be submitted to JJAP.

Conference

International

3. Yi Xiao, Richard J.E. Taylor, Chuangqing Yu, Takuo Tanemura, and Yoshiaki Nakano, Room-Temperature Capsule-Shaped Wavelength-Scale Metal-Clad Laser Operating at 1550 nm, CLEO-Pacific Rim, 31 July - 4 August 2017, Singapore. [Oral presentation]

4. Yi Xiao, Richard J.E. Taylor, Kaiyin Feng, Mitsuhiro Watanabe, Takuo Tanemura and Yoshiaki Nakano, Design of Waveguide-Coupling Structure for Wavelength-Scale Capsule-Shaped Metal-Clad Laser, iNOW, 4th-12th August, 2017 Tianjin, China.

Domestic

5. Yi Xiao, Richard J.E. Taylor, Chuangqing Yu, Takuo Tanemura, and Yoshiaki Nakano, カプセル型波長スケール金属共振器レーザの試作と室温パルス発振,the 64th JSAP spring meeting, March 14-17, 2017, Yokohama.[Highlighted oral presentation]

References

[1] Y. -H. Xie, S. S. Iyer, "Light Emission from Silicon," *Science*, vol. 260, no. 5104, pp. 40-46, 1993.

[2] Foundry Services for InP-Based Photonic Integrated Circuits. [Online]. https://www.hhi.fraunhofer.de/en/departments/pc/research-groups/foundry-services-for-inp-based-photonic-integrated-circuits.html

[3] S. E. Miller, "Integrated optics: An Introduction," *Bell Syst. Tech. J.*, vol. 48, no. 7, pp. 209-2069, 1969.

[4] A. Kolodny, U. Weiser, N. Shamir, N. Magen, "Interconnect-power dissipation in a microprocessor," *Proc. 2004 Int. Workshop System Level Interconnect Prediction (ACM 2004) Session Interconnect Anal. SoCs Microprocess.*, pp. 7-13.

[5] Mark T. Wade, Yunsup Lee, Jason S. Orcutt, Luca Alloatti, Michael S. Georgas, Andrew S. Waterman, Jeffrey M. Shainline, Rimas R. Avizienis, Sen Lin, Benjamin R. Moss, Rajesh Kumar, Fabio Pavanello, Amir H. Atabaki, Henry M. Cook, Albert J. Ou, J Chen Sun, "Single-chip microprocessor that communicates directly using light," *Nature*, vol. 528, pp. 534-538, 2015.

[6] David A. B. Miller, "Device Requirements for Optical Interconnects to Silicon Chips," *Proceedings of the IEEE*, vol. 97, no. 7, pp. 1166 - 1185, 2009.

[7] et al., S. L. Chuang, in *17th Microoptics Conference (MOC' II)*, Sendai, Japan, Oct. 30 - Nov. 2, 2011.

[8] T.H. Maiman, "Stimulated Optical Radiation in Ruby," *Nature*, vol. 187, no. 4736, pp. 493-494, 1960.

[9] Robert N. Hall, G. E. Fenner, J. D. Kingsley, T. J. Soltys, and R. O. Carlson, "Coherent Light Emission From GaAs Junctions," *Physical Review Letters*, vol. 9, no. 9, pp. 366-369, 1962.

[10] K. Iga, C. Kitahara, and Y. Suematsu, H. Soda, "GaInAsP/InP surface emitting

injection lasers," *Jpn. J. Appl. Phys.*, vol. 18, no. 12, pp. 2329-2330, 1979.

[11] R.E. Slusher, S.L. McCall, T. Tanbun-Ek, D.L. Coblentz, S.J. Pearton A.F.J. Levi, "Room temperature operation of microdisc lasers with submilliamp threshold current," *Electronics Letters*, vol. 28, no. 11, pp. 1010-1012, 1992.

[12] Se-Heon Kim, Soon-Hong Kwon, Young-Gu Ju, Jin-Kyu Yang, Jong-Hwa Baek, Sung-Bock Kim, Yong-Hee Lee, Hong-Gyu Park, "Electrically Driven Single-Cell Photonic Crystal Laser," *Science*, vol. 305, no. 5689, pp. 1444-1447, 2004.

[13] Tomonari Sato, Akihiko Shinya, Kengo Nozaki, Wataru Kobayashi, Hideaki Taniyama, Masaya Notomi, Koichi Hasebe, Takaaki Kakitsuka & Shinji Matsuo Koji Takeda, "Few-fJ/bit data transmissions using directly modulated lambda-scale embedded active region photonic-crystal lasers," *Nature Photonics*, vol. 7, pp. 569–575, 2013.

[14] G. I. Stegeman, and T. Tamir J. J. Burke, "Surface-polariton-like waves guided by thin, lossy metal films," *PHYSICAL REVIEW B*, vol. 33, no. 8, p. 5186, 1986.

[15] Yok Siang Oei, Barry Smalbrugge, Youcai Zhu, Tjibbe de Vries, Peter J. van Veldhoven, Frank W. M. van Otten, Tom J. Eijkemans, Jarosław P. Turkiewicz, Huug de Waardt, Erik Jan Geluk, Soon-Hong Kwon, Yong-Hee Lee, Richard Nötzel & Meint K. Martin T. Hill, "Lasing in metallic-coated nanocavities," *Nature*, vol. 1, pp. 589-594, 2007.

[16] M. T. Hill, Z. C. Liu, L. J. Yin, P. J. van Veldhoven, and C. Z. Ning K. Ding, "Record performance of electrical injection sub-wavelength metallic-cavity semiconductor lasers at room temperature," *Optics Express*, vol. 21, no. 4, pp. 4728-4733, 2013.

[17] Volker J. Sorger, Thomas Zentgraf, Ren-Min Ma, Christopher Gladden, Lun Dai, Guy Bartal & Xiang Zhang Rupert F. Oulton, "Plasmon lasers at deep subwavelength scale," *Nature*, vol. 461, pp. 629–632, 2009.

[18] Stuart Elston, Zhijun Liu, Gustavo Fernandes, Rashid Zia, and Jimmy Xu Jeffrey Shainline, "Subwavelength silicon microcavities," *Optics Express*, vol. 17, no. 25, pp. 23323-23331, 2009.

[19] Dorian Sanchez, Sophie Bouchoule, Paul Monnier, Gregoire Beaudoin, Isabelle Sagnes, Rama Raj & Fabrice Raineri Guillaume Crosnier, "Hybrid indium phosphide-on-silicon nanolaser diode," *Nature Photonics*, vol. 11, pp. 297–300, 2017.

[20] Tomonari Sato, Akihiko Shinya, Kengo Nozaki, Wataru Kobayashi, Hideaki Taniyama, Masaya Notomi, Koichi Hasebe, Takaaki Kakitsuka, and Shinji Matsuo Koji Takeda, "Few-fJ/bit data transmissions using directly modulated lambda-scale embedded active region photonic-crystal lasers," *Nature Photonics*, vol. 7, pp. 569–575, 2013.

[21] Dorian Sanchez, Sophie Bouchoule, Paul Monnier, Gregoire Beaudoin, Isabelle Sagnes, Rama Raj, and Fabrice Raineri Guillaume Crosnier, "Hybrid indium phosphide-on-silicon nanolaser diode," *Nature Photonics*, vol. 11, pp. 297–300, 2017.

[22] Amit M. Lakhani, and Ming C. Wu Myung-Ki Kim, "Efficient waveguide-coupling of metal-clad nanolaser cavities," *OPTICS EXPRESS*, vol. 19, no. 23, p. 23504, 2011.

[23] Masaya Nishimoto, Chuanqing Yu, Sueda Saylan, Richard J. E. Taylor, Takuo Tanemura, and Yoshiaki Nakano Kaiyin Feng, "Waveguide-coupled metal-clad cavity with integrated feedback stub," *Japanese Journal of Applied Physics*, vol. 56, p. 082201, 2017.

[24] B. Romeira, F. Pagliano, S. Birindelli, A. Higuera-Rodriguez, P. J. van Veldhoven, M. K. Smit, A. Fiore, and D. Heiss, V. Dolores-Calzadilla, "Waveguide-coupled nanopillar metal-cavity light-emitting diodes on silicon," *Nature Communications*, vol. 8, p. 14323, 2017.

[25] B. Romeira, S. Birindelli, L. E. Black, E. Smalbrugge, P. J. van Veldhoven, W. M. M. Kessels, M. K. Smit, and A. Fiore A. Higuera-Rodriguez, "Ultralow Surface Recombination Velocity in Passivated InGaAs/InP Nanopillars," *Nano Letters*, vol. 17, no. 4, pp. 2627–2633, 2017.

[26] Greg Sun Jacob B. Khurgin, "How small can "Nano" be in a "Nanolaser"," *Nanophotonics*, vol. 1, no. 1, pp. 3-8, 2012.

[27] N. Gregersen, K. Yvind, and J. Mørk, T. Suhr, "Modulation response of nanoLEDs and nanolasers exploiting Purcell enhanced spontaneous emission," *Optics Express*, vol. 18, no. 11, pp. 11230-11241, 2010.

[28] Amit Lakhani, Rodney S. Tucker, and Ming C. Wu, Erwin K. Lau, "Enhanced modulation bandwidth of nanocavity light emitting devices," *Optics Express*, vol. 17, no. 10, pp. 7790-7799, 2009.

[29] Greg Sun Jacob B. Khurgin, "Comparative analysis of spasers, vertical-cavity surface-emitting lasers and surface-plasmon-emitting diodes," *Nature Photonics*, vol. 8, pp. 468–473, 2014.

[30] Bryan Ellis, Arka Majumdar, Jan Petykiewicz, Marie A. Mayer, Tomas Sarmiento, James Harris, Eugene E. Haller & Jelena Vučković Gary Shambat, "Ultrafast direct modulation of a single-mode photonic crystal nanocavity light-emitting diode," *Nature Communications*, vol. 2, p. 539, 2011.

[31] Ke Liu, Volker J. Sorger & Devendra K. Sadana Ning Li, "Monolithic III–V on Silicon Plasmonic Nanolaser Structure for Optical Interconnects," *Scientific Reports*, vol. 5, p. 14067, 2015.

[32] T. Okimoto, T. Tanemura and Y. Nakano, B. Zhang, "Proposal and Numerical Study on Capsule-Shaped Nanometallic Semiconductor Lasers ," *Jpn. J. Appl. Phys.*, vol. 53, p. 112703, 2014.

[33] T. Okimoto, T. Tanemura and Y. Nakano, B. Zhang, ""Q Factor Improvement by Capsule-Shaped Metallic Cavity Structure for Subwavelength Lasers," *Phys. Status Solidi A*, vol. 213, no. 4, pp. 965–969, 2016.

[34] H. Raether, *Surface Plasmons on Smooth and Rough Surfaces and on Gratings*.: Springer, 1988.

[35] J. Y. Vinet, and A. Mysyrowicz B. Prade, "Guided optical waves in planar heterostructures with negative dielectric constant," *Phys. Rev. B*, vol. 44, p. 13556,

1991.

[36] D. B. Li and C. Z. Ning, "Giant modal gain, amplified surface plasmon-polariton propagation, and slowing down of energy velocity in a metal-semiconductor-metal structure," *PHYSICAL REVIEW B*, vol. 80, p. 153304, 2009.

[37] Y., Furuya, K., Suematsu, "Theoretical spontaneous emission factor of injection lasers," *Institute of Electronics and Communication Engineers of Japan, Transactions, Section E (English)*, vol. E60, pp. 467-472, 1977.

[38] K. Petermann, "Calculated spontaneous emission factor for double-heterostructure injection lasers with gain-induced waveguiding," *IEEE Journal of Quantum Electronics*, vol. 15, no. 7, pp. 566-570, 1979.

[39] G. Nienhuis, and J. P. Woerdman M. P. van Exter, "Two simple expressions for the spontaneous emission factor β," *PHYSICAL REVIEW A*, vol. 54, p. 3553, 1996.

[40] E. M. Purcell, *PHYSICAL REVIEW JOURNALS*, vol. 69, p. 674, 1946.

[41] A. Anderson, E. A. Hinds, D. Meschede, L. Moi, and S. Haroche, W. Jhe, "Suppression of spontaneous decay at optical frequencies: Test of vacuum-field anisotropy in confined space," *PHYSICAL REVIEW LETTERS*, vol. 58, no. 1497, p. 666, 1987.

[42] Benjamin T H Varcoe, Berthold-Georg Englert, and Thomas Becker, Herbert Walther, "Cavity quantum electrodynamics," *Reports on Progress in Physics*, vol. 69, no. 5, pp. 1325-1382, 2006.

[43] S. Machida, and G. Björk, Y. Yamamoto, "Microcavity semiconductor laser with enhanced spontaneous emission," *PHYSICAL REVIEW A*, vol. 44, p. 657, 1991.

[44] H. Yokoyama, E.P. Ippen, S.D. Brorson, "Spontaneous emission rate alteration in optical waveguide structures," *IEEE Journal of Quantum Electronics*, vol. 26, no. 9, pp. 1492-1499, 1990.

[45] Sriharsha V. Jayanti, Stephan J. P. Kress, Stefan Meyer, Stelio Iotti, Aurelio Rossinelli, and David J. Norris Kevin M. McPeak, "Plasmonic Films Can Easily Be Better: Rules and Recipes," *ACS Photonics*, vol. 2, no. 3, pp. 326–333, 2015.

[46] Yasuo Takahashi, Kenji Yamazaki, Toru Yamaguchi, Masao Nagase, and Kenji Kurihara, Hideo Namatsu, "Three-dimensional siloxane resist for the formation of nanopatterns with minimum linewidth fluctuations," *Journal of Vacuum Science & Technology B*, vol. 16, no. 69, pp. 69-76, 1998.

[47] Hagen CW, Grigorescu AE, "Resists for sub-20-nm electron beam lithography with focus on HSQ state of the art," *Nanotechnology*, vol. 20, no. 29, p. 292001, 2009.

[48] K. Ding and C. Z. Ning, "Fabrication challenges of electrical injection metallic cavity semiconductor nanolasers," *Semiconductor Science and Technology*, vol. 28, no. 12, p. 124002, 2013.

[49] Kostadin Djordjev, Sang Jun Choi, and P. Daniel Dapkus, Seung June Choi, "CH4 -based dry etching of high Q InP microdisks," *Journal of Vacuum Science & Technology B*, vol. 20, p. 301, 2002.

[50] S. K. Krawczyk and G. Hollinger, "Photoluminescence and x-ray photoelectron spectroscopy measurements of InP surface treated by acid and base solutions," *Applied Physics Letters*, vol. 45, p. 870, 1984.

[51] B. Romeira, S. Birindelli, L. Black, B. Smalbrugge, W. M. M. Kessels, M. K. Smit, and A. Fiore, A. Higuera-Rodriguez, "Ultra-low surface recombination for deeply etched III-V semiconductor nano-cavity lasers," in *Advanced Photonics 2016 (IPR, NOMA, Sensors, Networks, SPPCom, SOF), paper ITu2A.2*, 2016.

[52] G D T Spiller and M Hanbucken, J A Venables, "Nucleation and growth of thin films," *Reports on Progress in Physics*, vol. 47, no. 4, p. 399, 1984.

[53] Jean-Pierre Vilcot, Marc François, Didier Decoster, Denis Lauvernier, "Optimization of HSQ resist e-beam processing technique on GaAs material," *Microelectronic Engineering*, vol. 75, no. 2, pp. 177-182, 2004.

[54] Marco C. van der Krogt, Cees W. Hagen and Pieter Kruit, Anda E. Grigorescu, "Influence of the development process on ultimate resolution electron beam lithography, using ultrathin hydrogen silsesquioxane resist layers," *Journal of Vacuum Science & Technology B*, vol. 25, no. 6, p. 1998, 2007.

[55] T. H. P. Chang, "Proximity effect in electron-beam lithography," *Journal of Vacuum Science and Technology*, vol. 12, p. 1271, 1975.

[56] B.K Choi, O. Kim E. Seo, "Determination of proximity effect parameters and the shape bias parameter in electron beam lithography," *Microelectronic Engineering*, vol. 53, pp. 305-308, 2000.

[57] B. Cook, PYRAMID S. Lee, "a hierarchical, rule-based approach toward proximity effect correction – part II: correction," *IEEE Transactions on Semiconductor Manufacturing*, vol. 11, no. 1, pp. 117-128, 1998.

[58] P.D. Greber, H. Rothuizen S.J. Wind, "Accuracy and efficiency in electron beam proximity effect correction," *Journal of Vacuum Science B*, vol. 16, no. 6, pp. 3262-3268, 1998.

[59] D.L. Olynick, W. Chao, B. Harteneck and E. Veklerov E.H. Anderson, "Influence of sub-100 nm scattering on high-electron beam lithography," *Journal of Vacuum Science*, vol. 19, no. 6, pp. 2504-2507, 2001.

[60] B. Cook, PYRAMID S. Lee, "a hierarchical, rule-based approach toward proximity effect correction – part I: exposure estimation," *IEEE Transactions on Semiconductor Manufacturing*, vol. 11, no. 1, pp. 108-116, 1998.

[61] S.D. Berger, J.A. Liddle and W.K. Waskiewicz, G.P. Watson, "A background dose proximity effect correction technique for scattering with angular projection electron lithography implemented in hardware," *Journal of Vacuum Science Technology B*, vol. 13, no. 6, pp. 2504-2507, 1995.

[62] GenISys. [Online]. https://www.genisys-gmbh.com/web/

[63] Jae Su Yu and Yong Tak Lee, "Parametric reactive ion etching of InP using Cl2 and CH4 gases: effects of H2 and Ar addition," *Semiconductor Science and Technology*, vol. 17, no. 3, pp. 230-236, 2002.

[64] S J Pearton and F Ren U K Chakrabarti, "Sidewall roughness during dry etching of InP," *Semiconductor Science and Technology*, vol. 6, no. 5, pp. 408-410, 1991.

[65] M. A. Dreisbach, P. M. Thomas, W. C. Dautremont-Smith, and L. A. Heimbrook, T.

R. Hayes, "Reactive ion etching of InP using CH4/H2 mixtures: Mechanisms of etching and anisotropy," *Journal of Vacuum Science & Technology B*, vol. 7, no. 5, p. 1130, 1989.

[66] R. A., Outlaw, *Chapter 3.3: Practical Aspects of Vacuum System Mass Spectrometers. In Handbook of Vacuum Science and Technology.*: Academic Press: San Diego, 1998.

[67] H. C. Kim and T. L. Alford, "Thickness dependence on the thermal stability of silver thin films," *Applied Physics Letters*, vol. 81, p. 4287, 2002.

[68] Stephen J. Fonash, "An Overview of Dry Etching Damage and Contamination Effects," *Journal of The Electrochemical Society*, vol. 137, no. 12, pp. 3885-3892, 1990.

[69] U. K. Chakrabarti, and W. S. Hobson, S. J. Pearton, "Reactive ion etching induced damage in GaAs and AlGaAs using C2H6/H2/Ar or CCl2F2/O2 gas mixtures," *Journal of Applied Physics*, vol. 66, p. 2061, 1989.

[70] W. Heni, Y. Fedoryshyn, J. Niegemann, A. Melikyan, D. L. Elder, B. Baeuerle, Y. Salamin, A. Josten, U. Koch, C. Hoessbacher, F. Ducry, L. Juchli, A. Emboras, D. Hillerkuss, M. Kohl, L. R. Dalton, C. Hafner and J. Leuthold C. Haffner, "All-plasmonic Mach–Zehnder modulator enabling optical high-speed communication at the microscale," *Nature Photonics*, vol. 9, pp. 525–528, 2015.

[71] Aleksandar Simic, Olesya Bondarenko, Boris Slutsky, Amit Mizrahi, Liang Feng, Vitaliy Lomakin and Yeshaiahu Fainman Maziar P. Nezhad, "Room-temperature subwavelength metallo-dielectric lasers," *Nature Photonics*, vol. 4, pp. 395–399, 2010.

[72] E. D. Palik, *Handbook of optical constants of solids.*: Academic Press, 1997.

[73] Mark D. Thoreson, Satoshi Ishii, Alexander V. Kildishev, and Vladimir M. Shalaev Weiqiang Chen, "Ultra-thin ultra-smooth and low-loss silver films on a germanium wetting layer," *Optics Express*, vol. 18, no. 5, pp. 5124-5134, 2010.

[74] Baifu Zhang, Yi Xiao, Richard JE Taylor, Takuo Tanemura, and Yoshiaki Nakano,

Chuanqing Yu, "Electrically Pumped Metallic Cavity Lasers with Thermal Management," in *The 24th Congress of the International Commission for Optics*, Tokyo, August, 2017.

[75] Jesse Lu and Jelena Vučković, "Nanophotonic computational design," *Optics Express*, vol. 21, no. 11, pp. 13351-13367, 2013.

[76] Jesse Lu and Jelena Vučković, "Objective-first design of high-efficiency, small-footprint couplers between arbitrary nanophotonic waveguide modes," *Optics Express*, vol. 20, no. 7, pp. 7221-7236, 2012.

[77] Chuanqing Yu, "Electrically driven metallic micro cavity semiconductor lasers with thermal management," *Master's dissertation, The University of Tokyo*, 2017.

[78] Kai Zhang, MengYi Cao, ShengLei Zhao, JinCheng Zhang, XiaoHua Ma, and Yue Hao YongHe Chen, "Study of surface leakage current of AlGaN/GaN high electron mobility transistors," *Applied Physics Letters*, vol. 104, p. 153509, 2014.

[79] Joost Brouckaert, Dirk Taillaert, Pieter Dumon, Wim Bogaerts, Dries Van Thourhout, Roel Baets, Richard Nötzel, and Meint Smit, Gunther Roelkens, "Integration of InP/InGaAsP photodetectors onto silicon-on-insulator waveguide circuits," *Optics Express*, vol. 13, no. 25, pp. 10102-10108, 2005.

[80] Marie-Luce Thèye, "Investigation of the Optical Properties of Au by Means of Thin Semitransparent Films," *PHYSICAL REVIEW B*, vol. 2, p. 3060, 1970.

[81] Jacob B. Khurgin, "How to deal with the loss in plasmonics and metamaterials," *Nature Nanotechnology*, vol. 10, pp. 2-6, 2015.

[82] P.R. West S. Ishii G.V. Naik N.K. Emani V.M. Shalaev A. Boltasseva, "Searching for better plasmonic materials," *Laser & Photonics Reviews*, vol. 4, no. 6, pp. 795-808, 2010.

[83] Jacob B. Khurgin and Alexandra Boltasseva, "Reflecting upon the losses in plasmonics and metamaterials," *MRS BULLETIN*, vol. 37, no. 8, pp. 768-779, 2012.

[84] Jianxing Zhang, Dandan Huang, Hao Sun, Fan Fan, Jiabin Feng, Zhen Wang & C. Z. Ning, Yongzhuo Li, "Room-temperature continuous-wave lasing from monolayer

molybdenum ditelluride integrated with a silicon nanobeam cavity," *Nature Nanotechnology*, vol. 12, pp. 987–992, 2017.

[85] Sonia Buckley, John R. Schaibley, Liefeng Feng, Jiaqiang Yan, David G. Mandrus, Fariba Hatami, Wang Yao, Jelena Vučković, Arka Majumdar & Xiaodong Xu, Sanfeng Wu, "Monolayer semiconductor nanocavity lasers with ultralow thresholds," *Nature*, vol. 520, pp. 69–72, 2015.

[86] Jitao Li, Chunxiang Xu, Shuangpeng Wang, Chongxin Shan, Bin Xuan, Yongqiang Ning, and Dezhen Shen, Mingming Jiang, "Graphene induced high-Q hybridized plasmonic whispering gallery mode microcavities," *Optics Express*, vol. 22, no. 20, pp. 23836-23850, 2014.

[87] A. F. J. Levi, R. E. Slusher, S. J. Pearton, and R. A. Logan, S. L. McCall, "Whispering-gallery mode microdisk lasers," *Applied Physics Letters*, vol. 60, p. 289, 1992.

[88] Kostadin Djordjev, Sang Jun Choi, and P. Daniel Dapkus, Seung June Choi, "Microdisk lasers vertically coupled to output waveguides," *IEEE Photonics Technology Letters*, vol. 15, no. 10, pp. 1330-1332, 2003.

Acknowledgements

I would like to express my gratitude to everyone around me. They are all warm-hearted, gave me many help kindly during my Ph. D course.

I would like to thank my advisor Prof. Yoshiaki Nakano for offering me a great opportunity to be a member of photonics group, who guided me with his broad and rich knowledge, who inspired and encouraged me with thought of realizing friendship beyond national boundaries. I would like to thank Prof. Takuo Tanemura, who constantly gave me help and advice both in research and career path, who always encourages me saying "don't worry, you are doing fine". I thank you for leading me into researcher's world.

I would like to thank Prof. Masakazu Sugiyama for his insightful comments meetings and pre-defense. His view from different aspect helped me to improve my research.

I would like to thank Baifu Zhang, who patiently answered my questions in my first year studies even though he was working in Nanjing. I would like to thank Koh Chieda, who taught me how to do the fabrication after his final defense. I would like to thank Chuanqing Yu, Kaiyin Feng, for sharing ideas and know-how of fabrication. They are energetic and always have new ideas, which always enlightens me. I would like to thank Richard Taylor, who trained me to do laser measurement and data analysis, taught me how to write English papers, as well as enjoy in a Britain styled bar. I would like to thank Masaya Nishimoto for his comments in group meetings. His views inspired me a lot in thinking about basic physics.

I would like to thank Kento Komatsu, Takahiro Suganuma, Daiji Yamashita, who ran and do the maintenance of network of our lab and software. They helped me kindly whenever I have problems in using simulation software. I would like to thank Eisaku Kato, who does the maintenance of equipment in our cleanroom, helps me a lot whenever I have problems in doing fabrication. I would like to thank Jiaqi Zhang, Rui Tang, Hsiang-Hung Huang, Ryota Tanomura, Takahiro Suganuma, Mohiyuddin Atharuddin

Kazi, Yusuke Kohno, Peng Zhou, Masaharu Fukuda, Yuguang Wang, and Mitsuhiro Watanabe. We shared opinions about science, life, news and so on. Those trivial chatting are treasure memories for me. I would like to thank Makoto Fujiwara in Mita lab, who taught me how to use electron-beam lithography system in Takeda cleanroom, helped me a lot when I have troubles with that equipment.

I would like to thank my parents, who are always supporting me, give me courage to overcome difficulties. I would like to thank Emi Tokiyoshi, who always encourages me when I feel frustrated. I cannot finish my Ph. D without help from all of you.